NAVAL POSTGRADUATE SCHOOL

MONTEREY, CALIFORNIA

THESIS

EVALUATION OF STRAIGHT AND SWEPT RAMP OBSTACLES ON ENHANCING DEFLAGRATION-TO-DETONATION TRANSITION IN PULSE DETONATION ENGINES

by

Carlos A. Medina

December 2006

Thesis Advisor:	Christopher M. Brophy
Second Reader:	Jose O. Sinibaldi

Approved for public release; distribution is unlimited

THIS PAGE INTENTIONALLY LEFT BLANK

REPORT DOCUMENTATION PAGE			Form Approved OMB No. 0704-0188
Public reporting burden for this collection of information is estimated to average 1 hour per response, including the time for reviewing instruction, searching existing data sources, gathering and maintaining the data needed, and completing and reviewing the collection of information. Send comments regarding this burden estimate or any other aspect of this collection of information, including suggestions for reducing this burden, to Washington headquarters Services, Directorate for Information Operations and Reports, 1215 Jefferson Davis Highway, Suite 1204, Arlington, VA 22202-4302, and to the Office of Management and Budget, Paperwork Reduction Project (0704-0188) Washington DC 20503.			
1. AGENCY USE ONLY *(Leave blank)*	**2. REPORT DATE** December 2006	**3. REPORT TYPE AND DATES COVERED** Master's Thesis	
4. TITLE AND SUBTITLE: Evaluation of Straight and Swept Ramp Obstacles on Enhancing Deflagration-to-Detonation Transition in Pulse Detonation Engines		**5. FUNDING NUMBERS**	
6. AUTHOR(S): Carlos A. Medina			
7. PERFORMING ORGANIZATION NAME(S) AND ADDRESS(ES) Naval Postgraduate School Monterey, CA 93943-5000		**8. PERFORMING ORGANIZATION REPORT NUMBER**	
9. SPONSORING /MONITORING AGENCY NAME(S) AND ADDRESS(ES) N/A		**10. SPONSORING/MONITORING AGENCY REPORT NUMBER**	
11. SUPPLEMENTARY NOTES The views expressed in this thesis are those of the author and do not reflect the official policy or position of the Department of Defense or the U.S. Government.			
12a. DISTRIBUTION / AVAILABILITY STATEMENT Approved for public release; distribution is unlimited		**12b. DISTRIBUTION CODE** A	

13. ABSTRACT (maximum 200 words):

The use of detonations to achieve thrust in pulse detonation engines (PDEs) offers significant advantages in efficiency, simplicity, and versatility. An enabling mechanism for practical PDE implementation will likely utilize an efficient deflagration-to-detonation transition (DDT) process. This method simplifies detonation generation, but the required length is prohibitive in many applications and limits the frequency of repeatability. Obstacles have historically been employed to minimize the DDT distance, but often result in significant total pressure losses that degrade the delivered efficiency advantages of PDEs. This thesis explored the use of straight and swept ramp obstacles to accelerate DDT while minimizing the overall pressure losses. Computer modeling examined three-dimensional disturbances caused by such obstacles. Experimental tests measured combustion shockwave speed, flame velocity, and flame front interactions with obstacles. Evaluations were completed for several straight ramp obstacle configurations in a modeled two-dimensional flow. The placement of consecutive ramps resulted in flame acceleration accompanied by significant pressure spikes approaching 500 psi. Although detonation was not verified across the instrumented section, experimental data prove that straight ramp obstacles successfully accelerate the DDT process. Computer modeling predicts that swept ramps may be even more effective by introducing streamwise vorticity with a relatively low pressure drop.

14. SUBJECT TERMS Pulse Detonation Engines, PDE, PDE Ignition, PDE Initiation, Ramp, Ramp Injectors, Straight Ramp, Swept Ramp, Swept Ramp Injectors			**15. NUMBER OF PAGES** 129
			16. PRICE CODE
17. SECURITY CLASSIFICATION OF REPORT Unclassified	**18. SECURITY CLASSIFICATION OF THIS PAGE** Unclassified	**19. SECURITY CLASSIFICATION OF ABSTRACT** Unclassified	**20. LIMITATION OF ABSTRACT** UL

NSN 7540-01-280-5500 Standard Form 298 (Rev. 2-89)
Prescribed by ANSI Std. 239-18

THIS PAGE INTENTIONALLY LEFT BLANK

Approved for public release; distribution is unlimited

EVALUATION OF STRAIGHT AND SWEPT RAMP OBSTACLES ON ENHANCING DEFLAGRATION-TO-DETONATION TRANSITION IN PULSE DETONATION ENGINES

Carlos A. Medina
Lieutenant Commander, United States Navy
B.S., United States Naval Academy, 1996

Submitted in partial fulfillment of the
requirements for the degree of

MASTER OF SCIENCE IN ASTRONAUTICAL ENGINEERING

from the

NAVAL POSTGRADUATE SCHOOL
December 2006

Author: Carlos A. Medina

Approved by: Christopher M. Brophy
Thesis Advisor

Jose O. Sinibaldi
Second Reader

Anthony J. Healey
Chairman, Department of Mechanical and Astronautical Engineering

THIS PAGE INTENTIONALLY LEFT BLANK

ABSTRACT

The use of detonations to achieve thrust in pulse detonation engines (PDEs) offers significant advantages in efficiency, simplicity, and versatility. An enabling mechanism for practical PDE implementation will likely utilize an efficient deflagration-to-detonation transition (DDT) process. This method simplifies detonation generation, but the required length is prohibitive in many applications and limits the frequency of repeatability. Obstacles have historically been employed to minimize the DDT distance, but often result in significant total pressure losses that degrade the delivered efficiency advantages of PDEs. This thesis explored the use of straight and swept ramp obstacles to accelerate DDT while minimizing the overall pressure losses. Computer modeling examined three-dimensional disturbances caused by such obstacles. Experimental tests measured combustion shockwave speed, flame velocity, and flame front interactions with obstacles. Evaluations were completed for several straight ramp obstacle configurations in a modeled two-dimensional flow. The placement of consecutive ramps resulted in flame acceleration accompanied by significant pressure spikes approaching 500 psi. Although detonation was not verified across the instrumented section, experimental data prove that straight ramp obstacles successfully accelerate the DDT process. Computer modeling predicts that swept ramps may be even more effective by introducing streamwise vorticity with a relatively low pressure drop.

THIS PAGE INTENTIONALLY LEFT BLANK

TABLE OF CONTENTS

THIS PAGE INTENTIONALLY LEFT BLANK

LIST OF FIGURES

LIST OF TABLES

THIS PAGE INTENTIONALLY LEFT BLANK

LIST OF ABBREVIATIONS, ACRONYMS, AND SYMBOLS

C-J	-	Chapman-Jouguet
CAD	-	Computer-Aided Design
CCD	-	Charge-Coupled Device
CFD	-	Computational Fluid Dynamics
CMOS	-	Complementary Metal–Oxide–Semiconductor
CPU	-	Central Processing Unit
Cequel	-	Chemical Equilibrium in Excel
DDT	-	Deflagration-To-Detonation Transition
NI	-	National Instruments
NPS	-	Naval Postgraduate School
PDE	-	Pulse Detonation Engine
RAM	-	Random Access Memory
RDT	-	Research, Design and Test
RPL	-	Rocket Propulsion Laboratory
STP		Standard Temperature and Pressure
USB	-	Universal Serial Bus
VI	-	Virtual Instrument
VIS	-	Variable Ignition System
ZND	-	Zeldovich–Neumann–Döring

A	-	Area
C	-	carbon
C_2H_4	-	ethylene
c	-	speed of sound
c_P	-	constant pressure coefficient of specific heat
cm	-	centimeter
f	-	fuel-to-air ratio
GB	-	gigabyte
GHz	-	gigahertz
g	-	gravitational constant
H	-	hydrogen
Hz	-	hertz
I.D.	-	Inner Diameter
I_{sp}	-	specific impulse
K	-	Kelvin
kg	-	kilogram
MHz	-	megahertz
m	-	meter
mm	-	millimeter
M	-	Mach number
MB	-	Megabyte

Mb	-	Megabit
$\dot{m}$	-	mass flow rate
$\dot{m}_f$	-	mass flow rate of fuel
$\dot{m}_a$	-	mass flow rate of air
$\dot{m}_{tot}$	-	total mass flow rate
N	-	nitrogen
O	-	oxygen
p	-	pressure
psi	-	pounds per square inch
P-v	-	pressure-specific volume
q	-	specific heat
R	-	specific gas constant
s	-	second
s	-	entropy
t	-	time
T	-	temperature
TI	-	Turbulence Intensity
u	-	velocity
v	-	velocity
ϕ	-	equivalence ratio
γ	-	specific heat ratio
ρ	-	density

ACKNOWLEDGMENTS

I would like to express my profound gratitude to Professor Chris Brophy for his guidance in developing an area of thesis research worthy of inspiration, and his endless mentorship and instruction throughout. I would also like to thank Professor Jose Sinibaldi for his invaluable contributions to my own understanding and growth. Without their tremendous enthusiasm, depth of knowledge, encouragement, and endless patience, this work would not have been possible. Their efforts and dedication to their professions truly inspired me.

I would also like to thank Mr. George Hageman and my graduate student peers, especially Lieutenant Commander Chris DeSena, Lieutenant Dave Dausen, and Captain Pat Hutcheson: their enthusiasm, technical assistance, and camaraderie were invaluable.

I am grateful Mr. Frank Franzen and Mr. Jim Lambert, whose exceptional machining abilities and willingness to go above and beyond the required efforts were greatly appreciated.

I am deeply indebted to Mr. Todd Rumbaugh of DRS Data & Imaging Systems, Inc., whose personal efforts during several technical setbacks directly contributed to completion of this thesis.

Finally, I would like to thank my beautiful wife Laura, for her endless support and understanding during this demanding time. I owe everything I am to her, in this and all endeavors.

THIS PAGE INTENTIONALLY LEFT BLANK

I. INTRODUCTION

Conventional propulsion systems, such as rockets and turbojet/turbofans, are quickly approaching maturity in both technology and performance. More advanced concepts, such as pulse detonation engines (PDEs), promise greatly increased thermodynamic efficiency and performance across a wider range of flight regimes. While several technological challenges still prevent the near-term implementation of this type of propulsion system, ongoing research at the Naval Postgraduate School (NPS) and several other institutions strives to make PDE propulsion a reality.

The primary advantage offered by PDEs is their high efficiency near constant-volume combustion process. Theoretical specific impulses greater than 2,000 seconds have been predicted, higher than all but the most efficient air-breathing turbojet and turbofan engines (Figure 1).

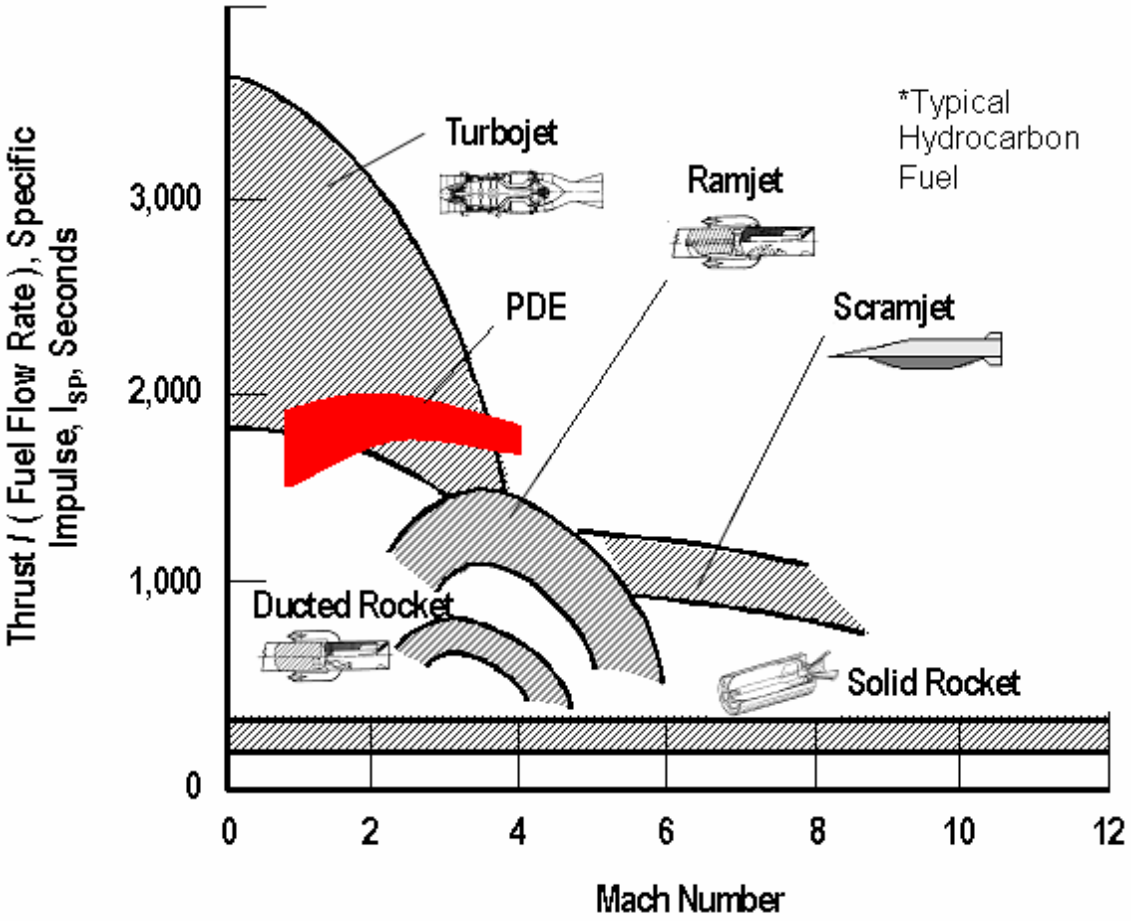

Figure 1. Propulsion Comparison Chart (After [1]).

Conventional turbojet systems are structurally and thermodynamically limited to a maximum speed approaching Mach 4. PDEs have a much greater performance zone ranging from zero velocity up to nearly Mach 5, although there are still controversies related to PDE's performance through the transonic region. Other advanced propulsion types such as ramjets and scramjets are capable of much higher speeds, but have a limited throttling capability and require booster systems to accelerate to their operational flight regime. Only PDEs offer the combination of high efficiency, a broad range of speed regimes, and relative engineering simplicity. Potential employments highlight low-weight, single-use systems capable of acceleration from subsonic to supersonic and have been largely focused on tactical missile applications [1].

II. BACKGROUND

Most current propulsion technologies rely on a constant-pressure combustion process. This process is used in many engine designs including gas turbine engines and solid rocket motors, where the burning of fuel takes place in the combustor under constant pressure conditions. While well studied and practicable, this process limits the overall engine efficiency. Alternative approaches have been studied to increase efficiency though use of different combustion processes. One such approach is the use of the constant-volume detonation combustion process, which allows for much more efficient burning of fuel. An effective way to utilize this process on an air-breathing propulsion system is through use of a pulse detonation combustor. If practically implemented, increases in thermal efficiency in a detonation engine can be translated to increases in propulsive efficiency. The following section describes the history of research into detonation and the principles that govern detonation theory.

A. DETONATION HISTORY

1. Early Research in Detonation

Detonation was first discovered in 1863 by A. Nobel, who described it simply as a "violent explosion." The process was not well understood, and not until the 1870s and 1880s did subsequent research begin to show to full meaning of detonation. F.A. Abel and M. Berthelot conducted research exploring the relationship between the strength of an explosion and its velocity of propagation. They theorized the existence of a shock wave required to create and sustain the detonation event. Following this research, M. Berthelot and P. Vielle sought to further characterize the velocities of these detonations. They concluded that the detonation velocity was uniform and dependent on the mixture ratio of the detonation medium [2].

This led to the work of H. Le Chatelier and E. Mallard, who in 1883 conducted experiments to examine the detonation process more closely. Their work demonstrated that a detonation could be produced through transition from deflagration, the well known combustion process seen in everything from gas turbine engines to candle flames. Their

experimentation showed that detonation was formed by a rapid adiabatic process feeding a detonation wave. They demonstrated that the speed of this detonation wave approached the sound velocity of the products combusted, and was therefore dependent on the detonation mixture and the type of ignition [2].

2. Chapman-Jouguet Theory

These early explorations into detonation were followed by increased interest in the process. In 1890, V.A. Michelson showed that the detonation pressure depended on the detonation velocity and the heats of reaction of the reactants. He found that the same reactants under different conditions gravitate toward two distinct reaction localities. He theorized that the detonation process was found near a convergence of pressures at the upper point [2].

Michelson's work was proven by D.L. Chapman and E. Jouguet in the early 1900s. Working independently, each proved the existence of these two regions in which combustion could occur, named the Upper and Lower Chapman-Jouguet (C-J) points. Chapman found that for any given detonable mixture, there was a minimum velocity at which the detonation could occur. Jouguet further clarified this idea with his proof that the velocity of the detonation wave is equal to the velocity of sound in the combusted mixture. Their combined results form the core of C-J theory, and include a series of equations that are modeled as a one-dimensional shock traveling through a detonable mixture. It assumes an instantaneous transition through the shock, and results in the theoretical steady state detonation wave velocity, termed the C-J velocity [3].

3. ZND Model

Further work was conducted near the middle of the twentieth century by Zeldovich, von Neumann, and Döring (ZND). Working independently, their research considered the chemical reaction rates of the detonated mixture. The ZND model described detonation with a finite shock wave transition preceded by undisturbed mixture and followed by two zones, an induction zone and a chemical reaction zone. These two zones arise due to chemical kinetics, which follow an Arrhenius law and for hydrocarbon oxidation include high activation energies. Therefore, only a very small amount of reaction occur initially (the induction zone) then the reactions approach completion at very high rates (chemical reaction zone) providing an overall highly energetic

combustion. The ZND model was much more comprehensive than the C-J model, but still did not fully describe the complexity of the detonation process [3].

4. Cellular Models

During the last few decades various combustion/detonation models have come to light, all which work only at very specific conditions. Although cellular behavior of detonations has been well documented in the technical literature, no single model has been able to properly describe all of the variations and intricacies found while performing experiments. More recently (in the last 10 years) researches have turned to numerical models ranging from modeling the Euler equations with a one or two step chemistry reaction scheme to the modeling of the full Navier-Stokes equations with extensive chemical kinetic reaction models. With the exponential increase of computing power since the advent of transistor, we are now capable of solving the former on a desktop personal computer; meanwhile the latter models still require supercomputing capabilities. Similar increases in laser diagnostics have allowed the validation of these highly complex numerical codes.

B. COMBUSTION PROCESSES

Detonation is a unique process, distinct from other types of reactions based on the speed of propagation, the shock wave created, and the effects of this shock on the continuing process. It can be obtained near-instantaneously through use of an explosive charge, high energy ignition, or shock focusing. Detonation can also be reached by transition from a more conventional burning process that becomes a detonation. The following sections describe these processes, and assume a premixed flame in which the reactants are mixed into a homogenous mixture before chemical reaction.

1. Deflagration

Deflagration is the most commonly known form of combustion, and approximates a constant-pressure thermodynamic reaction. Deflagration occurs when a combustion wave propagates at subsonic speeds through a reactive mixture. It is the process present in the flame of a candle, turbofan engines, conventional rocket motors, and approximates what occurs in a diesel engine.

Deflagration is often characterized by a laminar or turbulent flame. In an idealized deflagration event, combustion occurs only at the flame front, releasing energy and leaving behind only reacted products as it passes. As the deflagration wave travels, the energy released at the flame front heats and ignites the reactants that it encounters, further propagating the combustion. Because the combustion occurs through the thermal diffusion and interaction of particles, it is theoretically limited by definition to sonic speeds. In reality, it is further limited by the finite reaction rates of the reactive mixture, reducing the actual deflagration wave velocities to subsonic values. The total energy released by a deflagration is limited by the speed at which the flame front spreads, as combustion only occurs when the flame front reaches the reactants. Deflagration flame speed is further affected by the chemistry of the reactants and the temperature and pressure of the mixture as the flame front passes. Turbulence in the mixture can "wrinkle" the flame surface, which yields an increase of total area of the flame front. This allows the flame to increase the rate of consumption of reactants and thereby locally increasing the overall reaction rates.

Deflagration reactions result in a dramatic increase in entropy which can take away from the available work that may be obtained by the process. The effect is that deflagration reactions contain intrinsic thermodynamic efficiency limitations [3].

2. Detonation

The primary characteristic of detonation is the presence of a self-sustaining supersonic shock wave propagating through a reactive mixture. The shock wave compresses the mixture, causing a rapid rise in pressure, temperature, and density. These conditions result in a region behind the shock containing a highly energetic mixture with a temperature near ignition. Following the shock wave, this highly volatile mixture rapidly combusts in an extremely violent and energetic exothermic reaction. This reaction further supports the preceding shock wave and the two processes become coupled and self sustaining.

These two properties combine to give detonation a substantial increase in useful work energy which is released at a faster rate than achievable through deflagration [3].

3. Explosion

The third type of combustion reaction is an explosion, an extremely energetic and rapid reaction. Unlike the other forms considered, explosion does not require combustion wave passage though the exploding medium, has little applicability to propulsion, and will not be discussed further [3].

4. Deflagration vs. Detonation

Comparison of the characteristics of deflagration and detonation reactions further highlight the differences between the two. The model used for the following comparison is shown in Figure 2, with a combustion wave held stationary while reactants pass from left to right. The combustion wave model is of a simple one-dimensional planar wave. Unburned reactants on the left are annotated with the subscript 1; similarly, burned reactants on the left are annotated with the subscript 2.

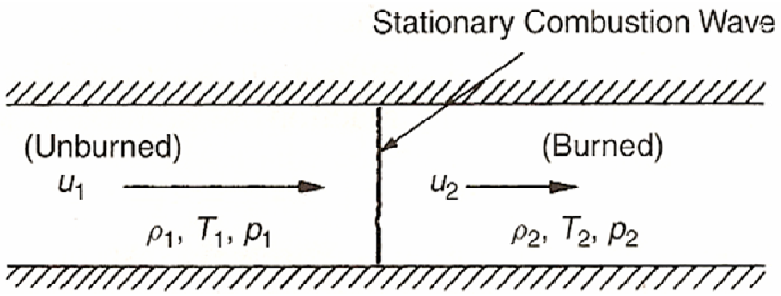

Figure 2. Stationary One-Dimensional Combustion Wave Model (From [3]).

Figure 2 and Table 1 show the velocity of the reactants (u), density (ρ), temperature (T), and pressure (p) before and after combustion wave passage. The unburned reactant velocity is further compared with the local speed of sound (c). These comparisons clearly show the dramatic increase in pressure and temperature present following the detonation wave.

	Detonation	Deflagration
u_1/c_1	5–10	0.0001–0.03
u_2/u_1	0.4–0.7 (deceleration)	4–6 (acceleration)
p_2/p_1	13–55 (compression)	$\approx$ 0.98 (slight expansion)
T_2/T_1	8–21 (heat addition)	4–16 (heat addition)
ρ_2/ρ_1	1.7–2.6	0.06–0.25

Table 1. Comparison of Detonation and Deflagration Characteristics (From [3]).

C. DETONATION THEORY

1. Detonation Thermodynamics

One of the conventional methods of characterizing the thermodynamic states possible for the simple one-dimensional model with heat release is the Hugoniot curve. This curve relates the pressure, density, and energy of a given mixture before and after passage through a standing shock wave. It is a one-dimensional steady state model similar to that depicted previously in Figure 2, assuming no heat transfer to the walls of this constant-area section. Fundamental assumptions of this model include the perfect gas law and the conservation of mass, momentum, and energy equations.

Perfect Gas Law: $$p = \rho RT \tag{1}$$

where R is the specific gas constant

Conservation of Mass: $$\rho_1 u_1 = \rho_2 u_2 \tag{2}$$

(Continuity Equation)

Conservation of Momentum: $$p_1 + \rho_1 u_1^2 = p_2 + \rho_2 u_2^2 \tag{3}$$

Conservation of Energy: $$c_p T_1 + \frac{1}{2}u_1^2 + q = c_p T_2 + \frac{1}{2}u_2^2 \tag{4}$$

where q is the specific heat added to the system,

and c_p is the specific heat at constant pressure, equivalent to:

$$c_p = \frac{\gamma}{\gamma - 1} R \tag{5}$$

Equation (2) shows that for a constant area problem, the mass flow rate ($\dot{m}$) must be constant, and after manipulation with (3) leads to the Raleigh-line relation

Raleigh-Line Relation: $$\rho_1 u_1^2 = \frac{p_2 - p_1}{\frac{1}{\rho_1} - \frac{1}{\rho_2}} = \dot{m} \tag{6}$$

Using (2), (3), and (5), Equation (6) can subsequently be manipulated into a form that eliminates the velocity conditions u_1 and u_2 and relates to the total heat release per unit of mass. It is known as the Hugoniot relation.

Hugoniot Relation:
$$\frac{\gamma}{\gamma-1}\left(\frac{p_2}{\rho_2}-\frac{p_1}{\rho_1}\right)-\frac{1}{2}(p_2-p_1)\left(\frac{1}{\rho_1}+\frac{1}{\rho_2}\right)=q \quad (7)$$

This equation describes the Hugoniot curve (Figure 3). This curve can be drawn for any combustion mixture with initial conditions p_1 and ρ_1 and for a given q, and shows all mathematically possible combinations of p_2 and $1/\rho_2$ (this inverse of density is also known as specific volume).

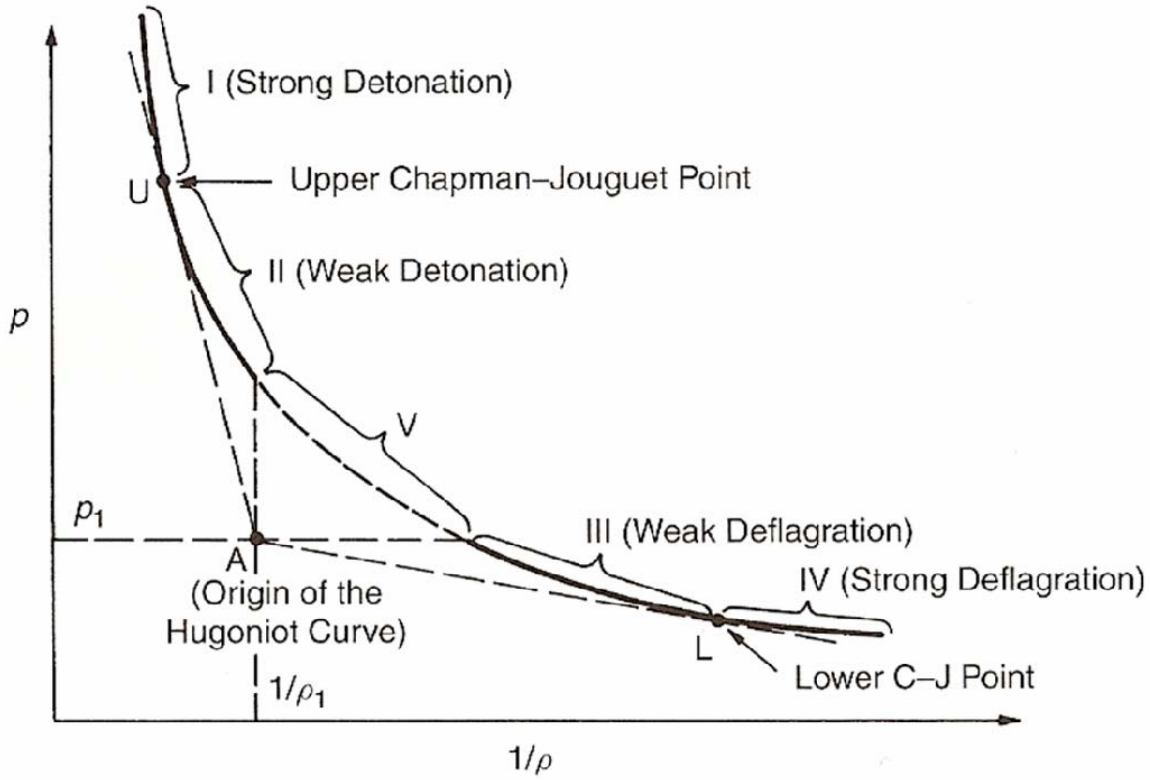

Figure 3. Hugoniot Curve Divided by Theoretical Regions (From [3]).

The origin of the Hugoniot Curve is defined by the initial conditions p_1 and ρ_1. From this origin, the curve is divided into five regions describing the five theoretical combustion conditions, and is delineated by four distinct points. Two points are shown by extending the constant pressure and constant specific volume lines through the origin until they intersect the curve. The remaining two points are defined by the tangential intersection of the curve with the origin, and correspond to the two Upper and Lower C-J points mentioned in the previous section.

Differentiating the Hugoniot relation (7) with respect to $1/\rho_2$, assuming q is fixed, after rearranging results in an equation describing the slope of the Hugoniot Curve:

$$\text{Slope of the Hugoniot Curve: } \frac{dp_2}{d(1/\rho_2)} = \frac{(p_2 - p_1) - \left(\frac{2\gamma}{\gamma - 1}\right) p_2}{\left(\frac{2\gamma}{\gamma - 1}\right)\frac{1}{\rho_2} - \left(\frac{1}{\rho_1} + \frac{1}{\rho_2}\right)} \tag{8}$$

The slope of the Hugoniot Curve at the tangent C-J points can also be represented as:

$$\text{Slope at C-J Points: } \frac{dp_2}{d(1/\rho_2)} = \frac{p_2 - p_1}{1/\rho_2 - 1/\rho_1} \tag{9}$$

Equating the right sides of (8) and (9), and combining with the Raleigh-line relation (6) produces a solution for the velocity of the burned reactants at the C-J points on the Hugoniot Curve:

$$\text{Velocity at C-J Points: } u_2^2 = \frac{\gamma p_2}{\rho_2} = c_2^2 \tag{10}$$

This relation leads to the important conclusion that the speed of the burned reactants at the C-J points, both for detonation and deflagration, is equal to the local speed of sound, or Mach = 1.

Of the five regions on the Hugoniot Curve (Figure 4), Region V is physically impossible as it would require a simultaneous increase in pressure with decrease in density. This would result in an imaginary value of u_1 in order to satisfy the Raleigh-line relation (6). Regions I and II are possible but transient and unstable, quickly gravitating toward another region. Region IV becomes unrealizable in a constant area problem as density decreases with little change in pressure. The only possibilities are in Region III, weak deflagration, and at the Upper C-J point which provides the unique solution critical for detonation [3].

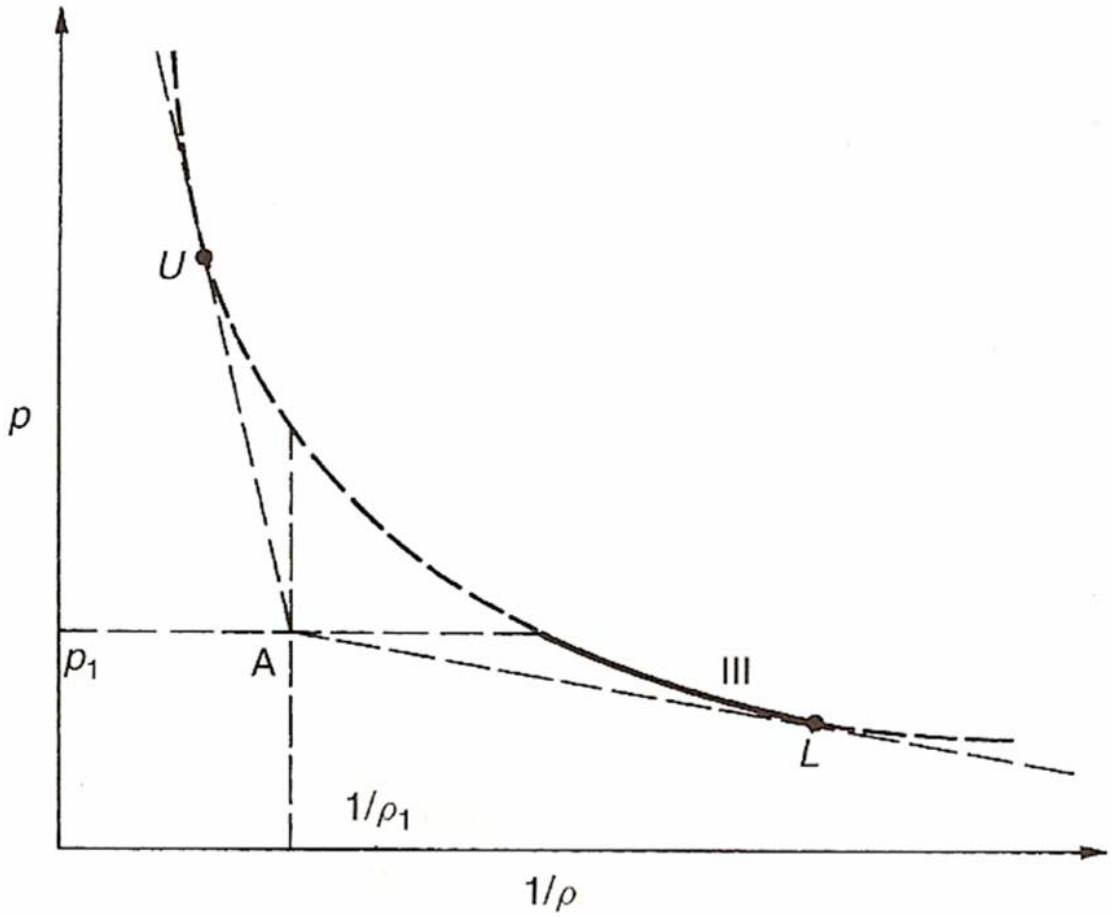

Figure 4. Hugoniot Curve Showing Possible Solution Regions (From [3]).

2. Detonation Structure

Once established, a detonation wave is sustained through a strong coupling with the combustion event that is intrinsically attached to it. The one-dimensional steady ZND model provides a good description of the general interactions associated with a detonation wave (Figure 5).

The reactive medium is relatively undisturbed prior to shock arrival. As the supersonic detonation shock wave passes, it delivers a considerable amount of energy to the mixture in a very short span. This energy rapidly increases temperature, pressure, and density in the mixture and increases it to the point of ignition. Immediately following the shock wave is the induction zone, where the reaction has just begun and the thermodynamic properties of the mixture remain relatively constant. As the flame front passes, an extremely energetic chemical reaction takes place in the reaction zone. This

very efficient adiabatic process releases tremendous energy which serves to further sustain the shock wave. The entire detonation event takes place across a distance of approximately 1 cm in hydrocarbon-air gaseous mixtures at STP.

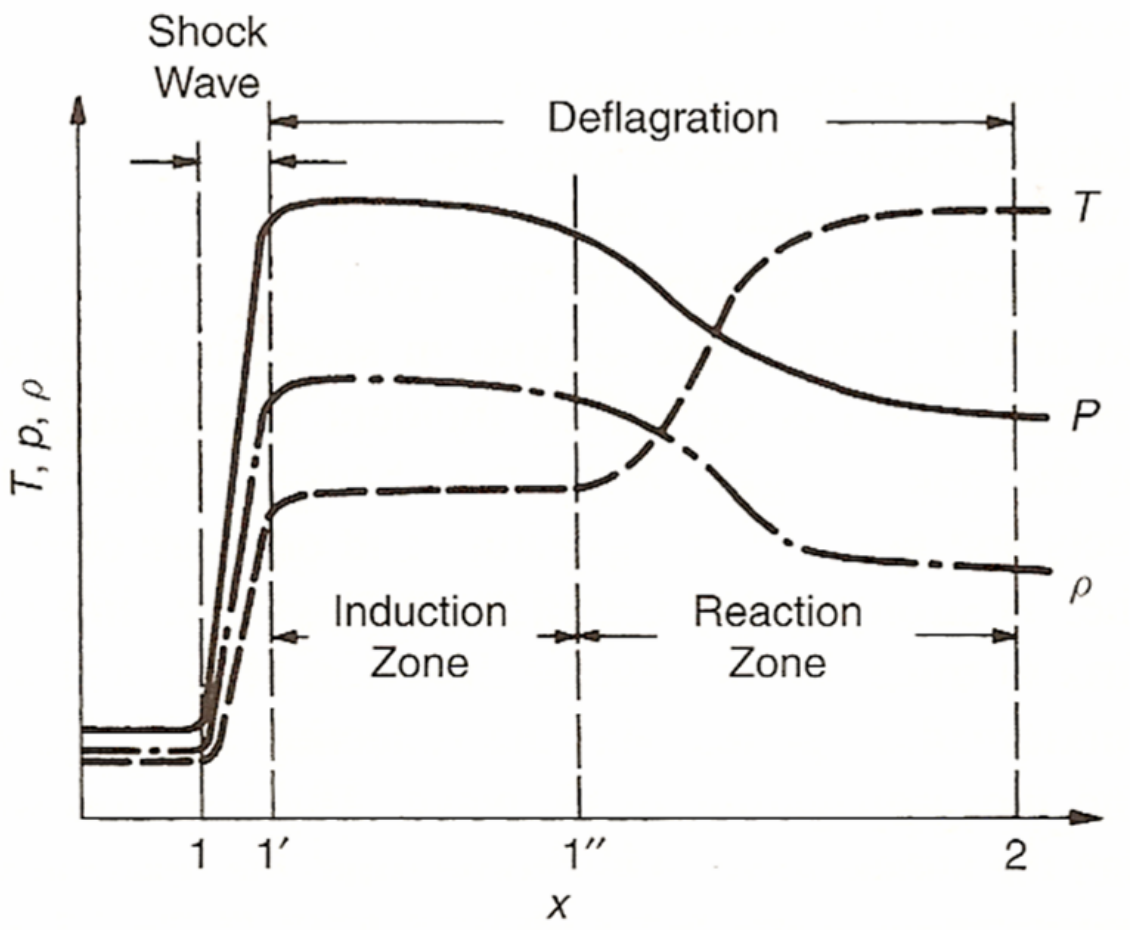

Figure 5. ZND Detonation Wave Profile (From [3]).

This one-dimensional analysis illustrates many of the important characteristics of a detonation event, but an actual detonation wave has a very complex three-dimensional structure (Figure 6). The leading shock wave of a detonation in generally normal to the direction of travel, but is not actually planar. Instead, it is composed of many small curved shock sections followed by perpendicular shockwaves interacting with each other and the front shock wave forming triple points which can be recorded using soot-foil techniques as shown in Figure 6. [3].

Figure 6. Image of Three-Dimensional Nature of Detonation Wave (From [3]).

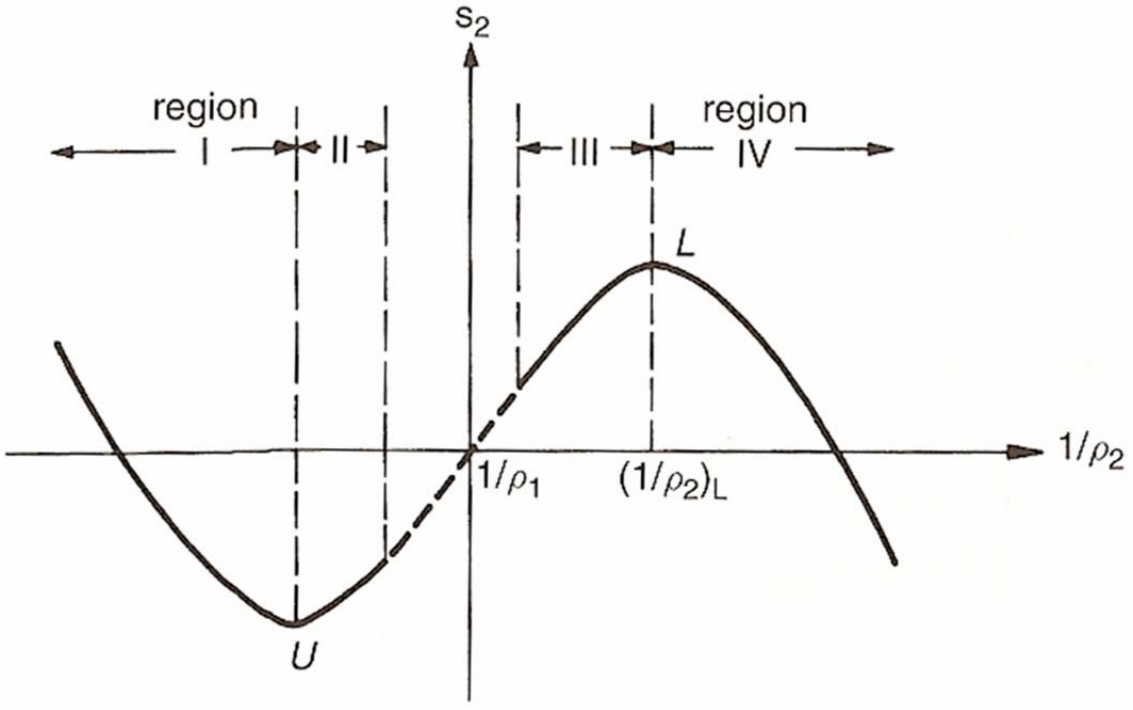

Figure 7. Entropy Distribution on to the Hugoniot Curve (From [3]).

3. Thermodynamic Advantages of Detonations

One of the most interesting features of the detonation phenomena is the high thermodynamic efficiency exhibited. Entropy (*s*) is used as a measure of the useful energy lost in a thermodynamic event. Thus, the lower the entropy the more thermodynamically efficient the combustion process is.

Referencing the Hugoniot Curve previously shown in Figures 3 and 4, Figure 7 shows the relative values of entropy in the different regions. Entropy is maximum at the Lower C-J point, the upper velocity regime of a deflagration. Entropy reaches a minimum at the Upper C-J point where detonation occurs. Thus, for combustion of any given reactive mixture, detonation is inherently more efficient in extracting useful energy from the reaction [3].

4. Deflagration-to-Detonation Transition

Detonation can be obtained though several methods, including the use of extremely high-energy ignition, confinement, shock focusing, explosive charges, or deflagration-to-detonation transition. However, to be useful in propulsion it must be repeatable and at a high enough frequency to achieve effective thrust. Deflagration-to-detonation transition has these favorable properties and for a propulsion system and is a principle means of detonation initiation in pulse detonation engines.

DDT refers to a detonation wave that is created from an initial deflagration wave. It begins with ignition of a reactive mixture forming a small kernel of combustion. The flame spreads and produces compression waves ahead of the accelerating wrinkled laminar flame front. These compression waves coalesce into a shock front, which leaves turbulence in its wake and causes the flame front to break into a turbulent flame brush. The flame surface area, reaction rates and energy at the flame front increase dramatically, until “an explosion in an explosion” occurs in the reaction zone (Figure 8). This causes two strong shock waves; the superdetonation wave traveling forward into the unburned gases, and the retonation wave moving backwards into the already combusted products. Oscillations between the two large shocks also form transverse waves (Figure 9).

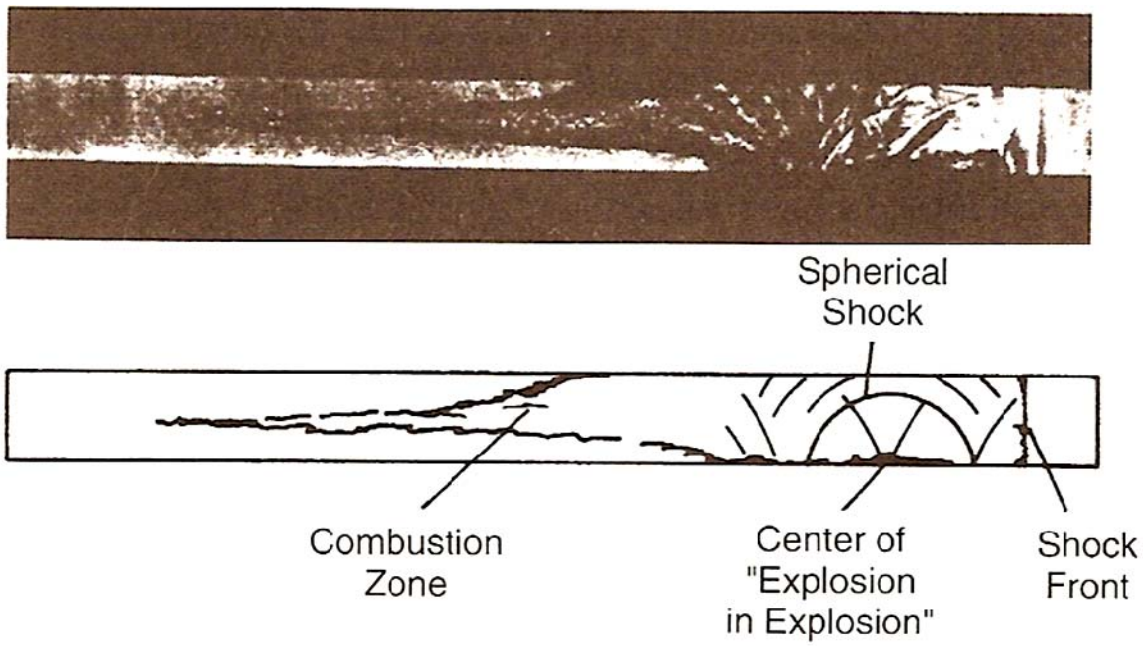

Figure 8. DDT "Explosion in an Explosion" (After [3]).

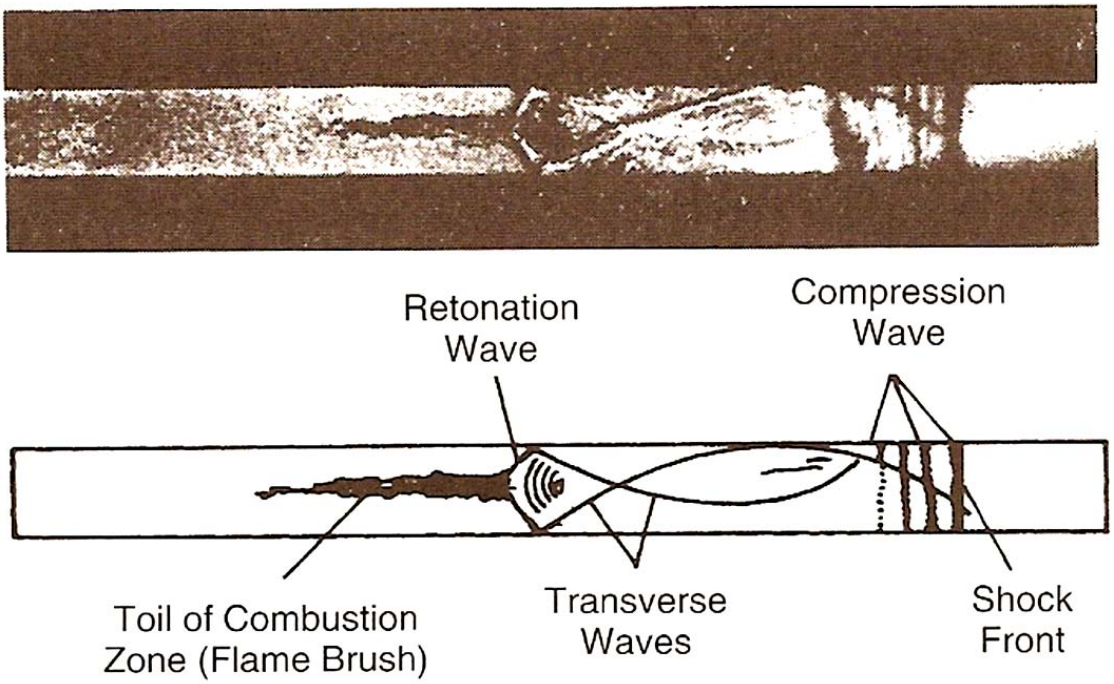

Figure 9. DDT Transverse Waves (After [3]).

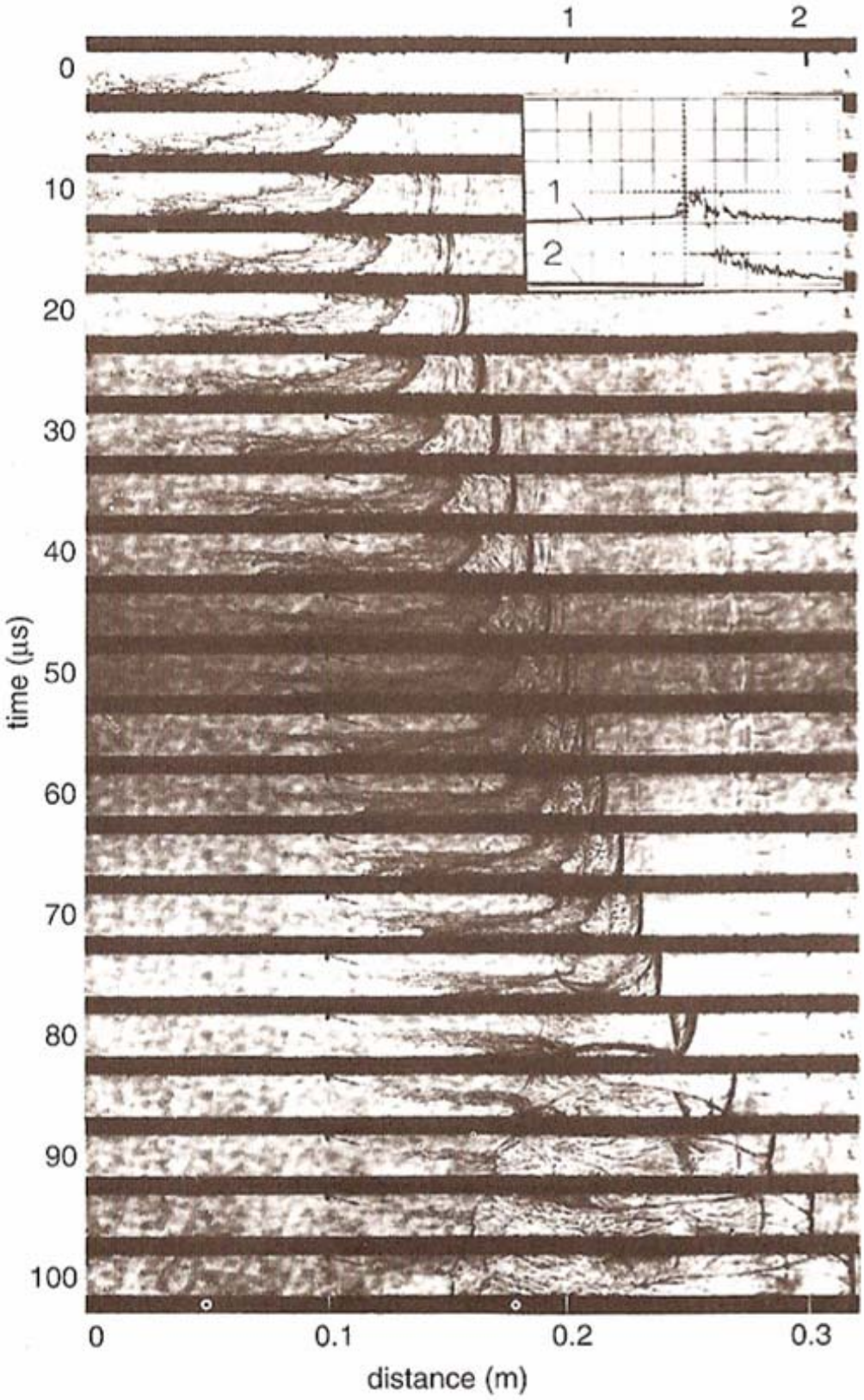

Figure 10. DDT Progression Sequence (From [3]).

A spherical shock wave also begins at the onset of this "explosion in an explosion," located near the boundary layer. As the multiple shocks propagate, the transverse waves interact with the original shock, the retonation wave, and the reaction zone. Eventually, a final steady detonation wave is formed from these interactions traveling at the C-J detonation velocity [3]. Figure 10 shows stroboscopic Schlieren images of the entire deflagration-to-detonation transition.

5. DDT Acceleration

Given sufficient distance in a smooth tube, deflagration-to-detonation in a reactive mixture can occur under certain conditions. This is due to wall effects and autoturbulization that cause high-intensity turbulence in the combustion zone. This turbulence causes increased wrinkling of the flame. The resultant increase in reactive surface area of the flame front leads to increases in release of energy, thus accelerating the flame.

Turbulence can also be intentionally created by the insertion of obstacles into the flow field as in Figure 11. Obstacles lead to greater turbulence and allow the DDT process to complete in a shorter distance. This is currently accomplished by use of screens, tabs, Shchelkin spirals, or some other form of turbulence-forming obstacle [4].

Placement of obstacles in the flow path may also help to form shock-focused "hot spots" that lead to self-ignition of the fuel ahead of the existing flame front and serve to accelerate the reaction zone. These two combined phenomena dramatically increase the reaction rates and strength of compression waves [5].

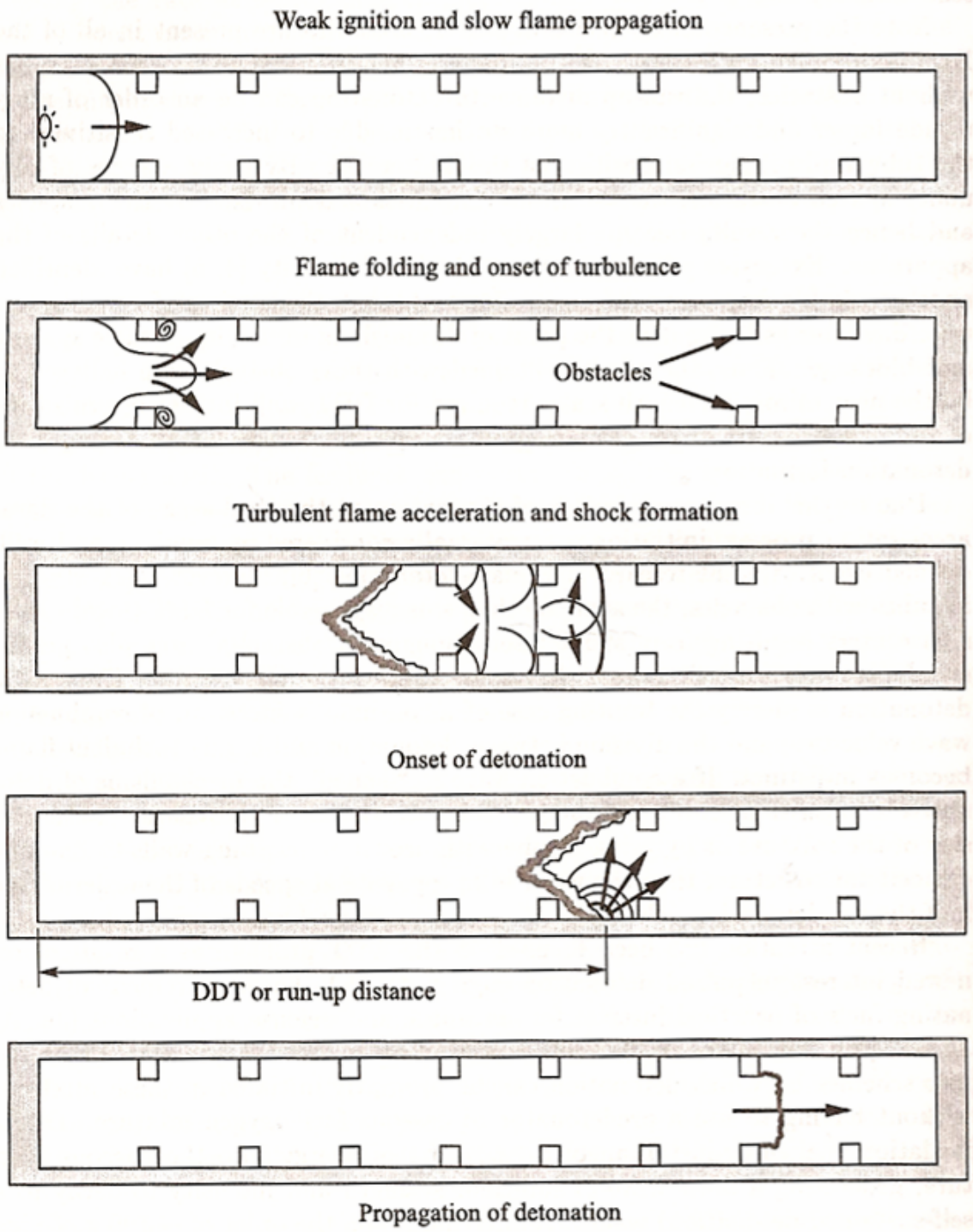

Figure 11. Sequence of DDT Acceleration in Tube with Obstacles (From [5]).

D. PULSE DETONATION ENGINES

Multiple successive detonation events must take place to achieve practical propulsion performance using detonations. If detonations are produced at high enough frequency, the result is near-constant thrust and typically this requires cyclic rates above 60 Hz. This type of system forms the pulse detonation engine concept [6].

1. Pulse Detonation Implementation

Figure 12 illustrates a single cycle of a generic pulse detonation engine, proceeding in a clockwise direction. It assumes a valved gas delivery in which the reactants flow to the chamber only during certain stages of the cycle.

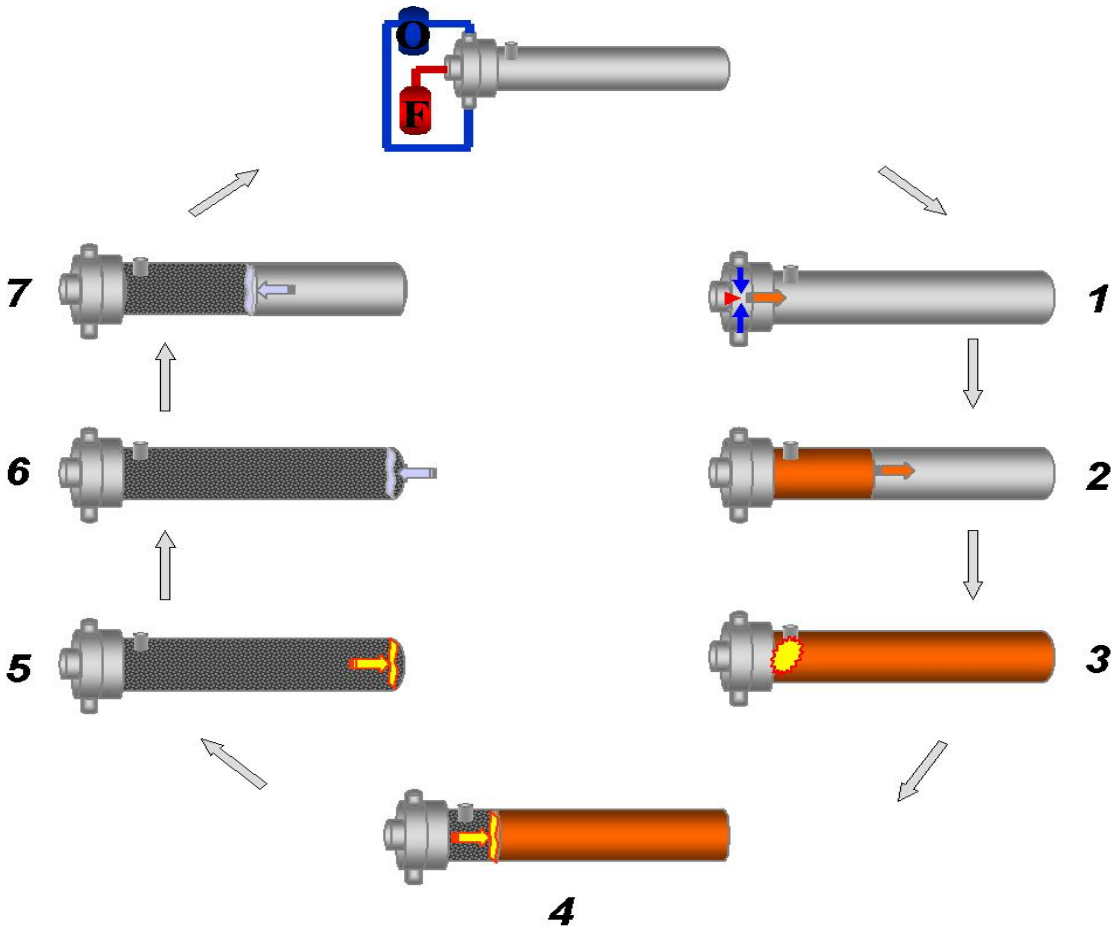

1. Reactants injected	5. Detonation wave exits
2. Tube fills	6. Rarefaction waves
3. Mixture ignited	7. Products exhausted
4. Detonation wave forms	8. Cycle repeats

Figure 12. Ideal PDE Operation Cycle (From [7]).

A description of each stage of the cycle follows. 1) The reaction chamber is initially empty when fuel and oxidizer begin injection into the head end. 2) The chamber then filled with the combustible mixture. Timing here is critical, as too long a fill will waste fuel and too short a fill will not utilize the total combustor volume, either situation reducing the overall efficiency of the engine. This portion of the cycle is referred to as t_{fill}. 3) Once the fill is complete, the mixture is ignited at the head end. This step may contribute $t_{ignition\_delay}$ if fill time is greater than the required value of t_{fill}, valve timing and actuation is required, or the ignition device itself is not recovered from the last cycle. 4) At some distance later, the detonation wave is formed. The time required for this event is $t_{detonation}$, and while it contributes relatively little to the overall cycle time, it determines the overall length of the chamber. The detonation may be achieved though extremely high-energy ignition or other direct means, but is most commonly the product of a deflagration-to-detonation transition. 5) The detonation wave travels quickly to the end of the chamber and exits the combustor. 6) After the detonation wave passes the end of the chamber, the combustion products inside suddenly "sense" atmospheric pressure and a rarefaction wave if formed traveling forward in the chamber. These last two steps combine to form $t_{blowdown}$. 7) Finally, the burned products in the engine must be exhausted before the cycle can begin again, requiring t_{purge} to complete [7].

2. Pulse Detonation Optimization

Thrust is only present during a portion of the pulse detonation cycle, and to produce near-constant thrust the cycle time must be held to a minimum. Referring to the time intervals defined previously, the total cycle time of a pulse detonation sequence is:

Cycle Time: $$t_{cycle} = t_{fill} + t_{ignition\_delay} + t_{detonation} + t_{blowdown} + t_{purge} \qquad (11)$$

The fill, blow down, and purge times are all highly dependent on the length of the chamber. Obstacles used to enhance DDT by creating turbulence may also have the undesired side effect of increasing the pressure loss through the combustor. Some PDEs use valveless configurations, in which the flow of gases is continued throughout the cycle, and may effectively reduce fill and purge time contributions, as well as ignition

delay times. Only the fuel is pulsed (using fuel injectors) thus removing the constraints of heavy and complex high speed gaseous valving technology that would otherwise be required.

If detonation is initiated indirectly, minimizing the time before the detonation wave is formed is critical, both for efficiency and due to the contribution to total cycle time.

Of the cycle steps, 4) and 5) are typically insignificant in their total contribution to cycle time, each on the order of hundreds of microseconds. The greatest contributions to cycle time, and therefore the greatest limitations on PDE operational frequency are ignition delay due to filling requirements.

3. Pulse Detonation Performance

The thermodynamic properties of the PDE give it the potential for significantly higher performance than other propulsion types, such as turbojets, ramjets, and rockets that operate utilizing the constant pressure Brayton cycle. The constant-volume process in PDEs provides the potential for propulsive efficiency gains of as high as 30%. This thermal efficiency can only be realized if implementation losses in the PDE cycle can be controlled and reduced [8].

E. MOTIVATION

Several significant challenges still face PDE designs. The first is increasing the frequency of detonations by minimizing the total time required to complete an entire detonation cycle. The second is reducing the chamber length required to achieve detonation since the minimum length is directly coupled to the length the turbulence devices required. The third is reliable achievement of detonation and a corrective technique to “restart” the sequence if a bad cycle occurs.

Current methods of detonation initiation focus on high energy ignition methods and/or placement of obstacles in the flow path. These obstacles often induce gas/dynamic flame interactions, increased turbulence, or shock focusing to provide “hot spots” that accelerate the deflagration-to-detonation transition. These obstacles also have the undesired side effect of pressure losses during fill and blow down, which lengthen the overall pulse detonation cycle time and sacrifice the efficiency gains inherent in PDEs.

This thesis explored the use of straight and swept ramp obstacles to enhance DDT while attempting to minimize and control pressure losses. The goal was to prove that these obstacles are as or more effective accelerators of DDT than other types already studied. Based on motivation, future research of the ramp geometry will study the inclusion of base flow injectors to further reduce total pressure losses. Multi-port fuel injectors may also allow much shorter fill times, thereby reducing PDE cycle time even further. Research has already examined the effects of swept ramp injectors in supersonic flowfields, but their application in the subsonic DDT regime is unexplored [9].

By finding a more efficient way to hasten the DDT process while maintaining the simplicity inherent in current PDE designs, the efficiency gains of pulse detonation propulsion may someday be realizable in applications outside the laboratory.

III. COMPUTER SIMULATION

Initial exploration of the proposed approach began with extensive computer modeling and simulation. The goal was to better understand and characterize the flow disturbances caused by shock interaction with both straight and swept ramp obstacles, including the use of base flow.

It must be emphasized that the peculiar qualities of detonation are not fully understood. Even the most advanced computer modeling software cannot directly predict the phenomena, due to the widely varying pressure and temperature conditions as well as the complicated chemistry involved. The simulations in this experimental thesis served primarily to provide qualitative data on which obstacle configurations were most likely to produce the desired effects.

Nearly 30 simulations were conducted for various geometries, initial conditions, and degrees of resolution and only 16 produced unique and useful results. The procedures are illustrated below, following a swept ramp three-dimensional simulation as an example.

The extensive computational demands of some of the more detailed models required significant processor time and memory. To illustrate, the model used in the example was one of the more aggressive simulations, composed of 2,661,250 distinct nodes. The transient solution took slightly less than 14 and-a-half days of continuous processing to progress through the majority of the test section and converge. Solutions were output at 200 iteration intervals, and required over 7.85 GB of memory to store the results.

A. MODELING SOFTWARE

Three software programs were used in succession to develop the computer model simulations. These modules were designed by Computational Fluid Dynamics Research Corporation and marketed by ESI Group, and were capable of both two- and three-dimensional modeling.

1. CFD-GEOM

CFD-GEOM was the first program used in the simulation process. It provided for geometric construction of the model, as well as volume and grid generation. It had extensive capabilities for import and export to other CAD software.

CFD-GEOM software was used to create two- and three-dimensional models for subsequent export to the solver package. The model was divided into zones or volumes, and these were further subdivided by placing grids across them (Figures 13-15). The total number of grid cells integrated into this model would determine both the resolution of the solution and the computational demands and time required to solve it.

A volume was created to house an obstacle near the center. In addition the test obstacle, a driver volume was added upstream to generate the shock wave required to simulate the expected experimental conditions. The grids were shaped in such a way to reduce total number of grid nodes while maximizing resolution around the areas of interest, primarily immediately downstream of the obstacle.

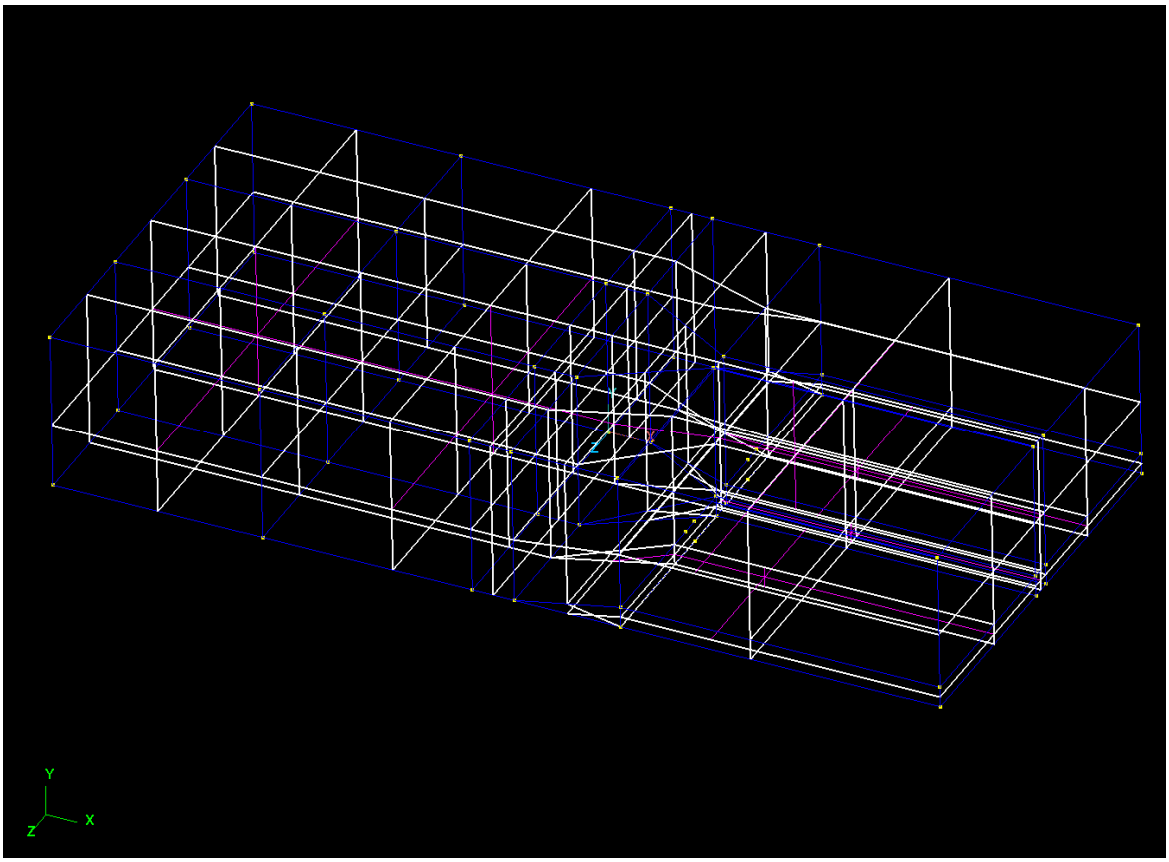

Figure 13. Example CFD-GEOM Construction 3-D View.

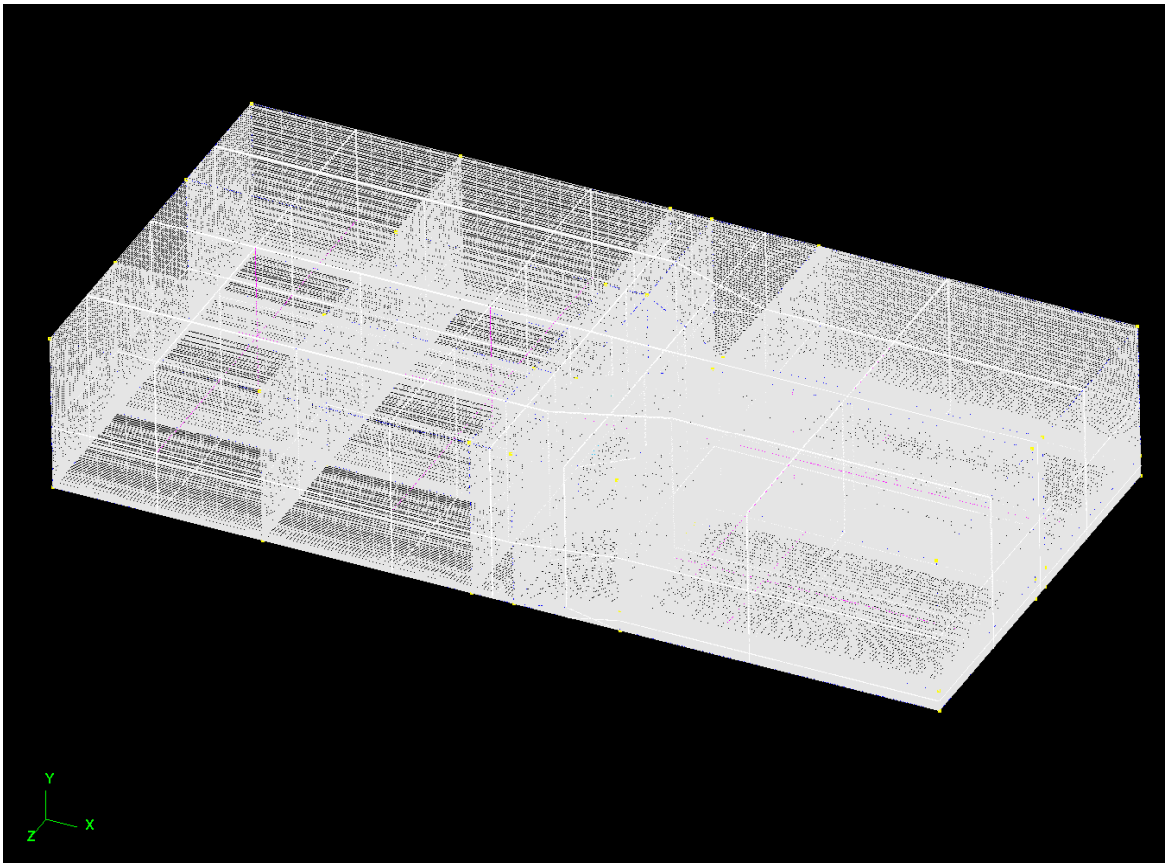

Figure 14. Example CFD-GEOM Grid Design 3-D View.

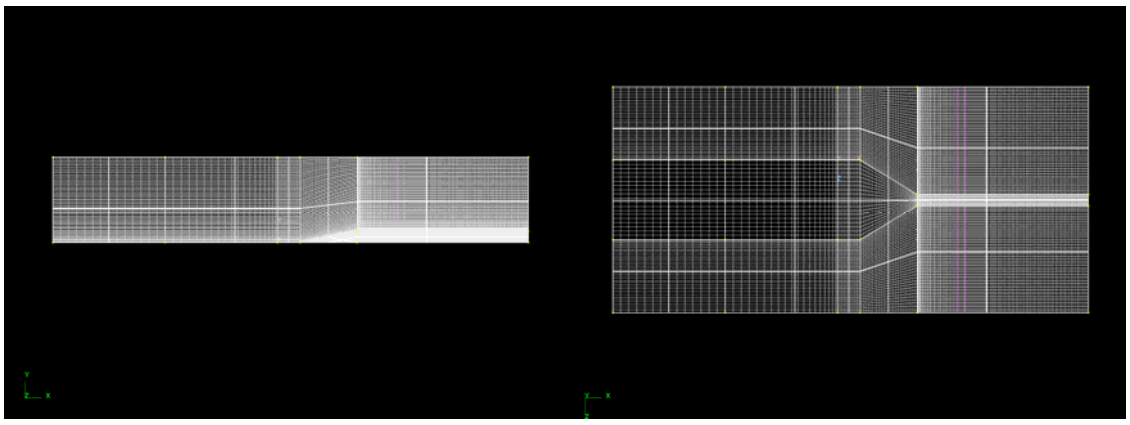

Figure 15. Example CFD-GEOM Grid Design Side and Top View.

2. CFD-FASTRAN

Once exported from CFD-GEOM, the grid file was imported into the CFD-FASTRAN solver program, a high resolution density-based finite-volume solver for compressible flows.

This program allowed the user to define the conditions of all of the volumes and surfaces imported from GEOM, as well as the initial and boundary conditions to be considered. The forward end was consistently defined as an inlet, the aft end an outlet, and the remaining faces as solid surfaces. Air was used as the fluid, and the model did not deal with any mixtures or combustion. The majority of the test volume was considered at sea-level atmospheric pressure, static, and with varying initial pressure. Some simulations also included base flow originating at the back of the ramp.

The driver volume was defined with conditions of high pressure and high temperature, separated from the test volume by a numerical interface. This interface allowed separate condition definition on either side, but had no physical meaning once the solver began. The purpose of this arrangement was to simulate the bursting of a diaphragm in a pressure driven shock tube, creating a shock that would propagate down to the test obstacle. In Figures 16 and 17, the diaphragm-like interface is represented in purple

The simulation was conducted in a time-accurate transient mode, providing complete instantaneous solutions of the entire volume at any interval defined by the user. These solutions were saved as discrete files, which could be viewed later in sequence [10].

The pressure and temperature for the driver volume were calculated using the Shockwave Calculator Applet available online. This program was used to determine the driver initial conditions to produce the desired shock wave [11].

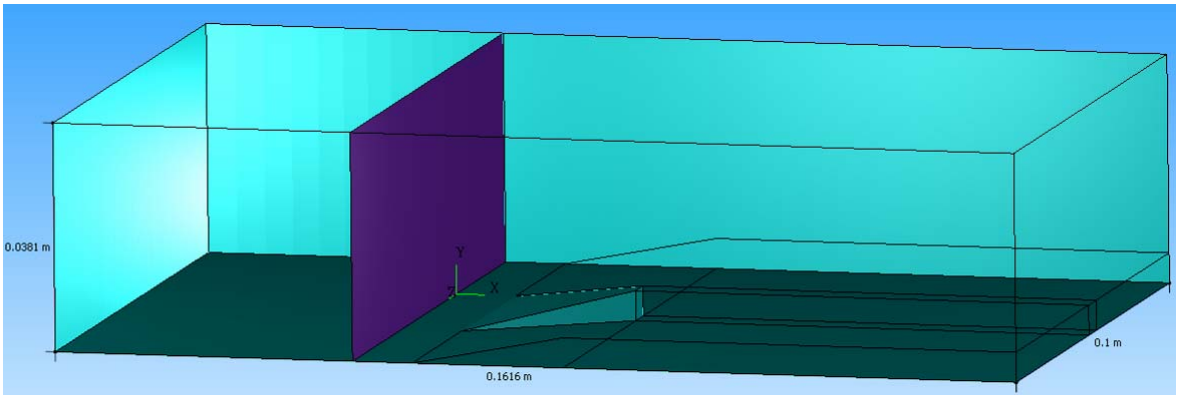

Figure 16. Example CFD-FASTRAN 3-D Side View.

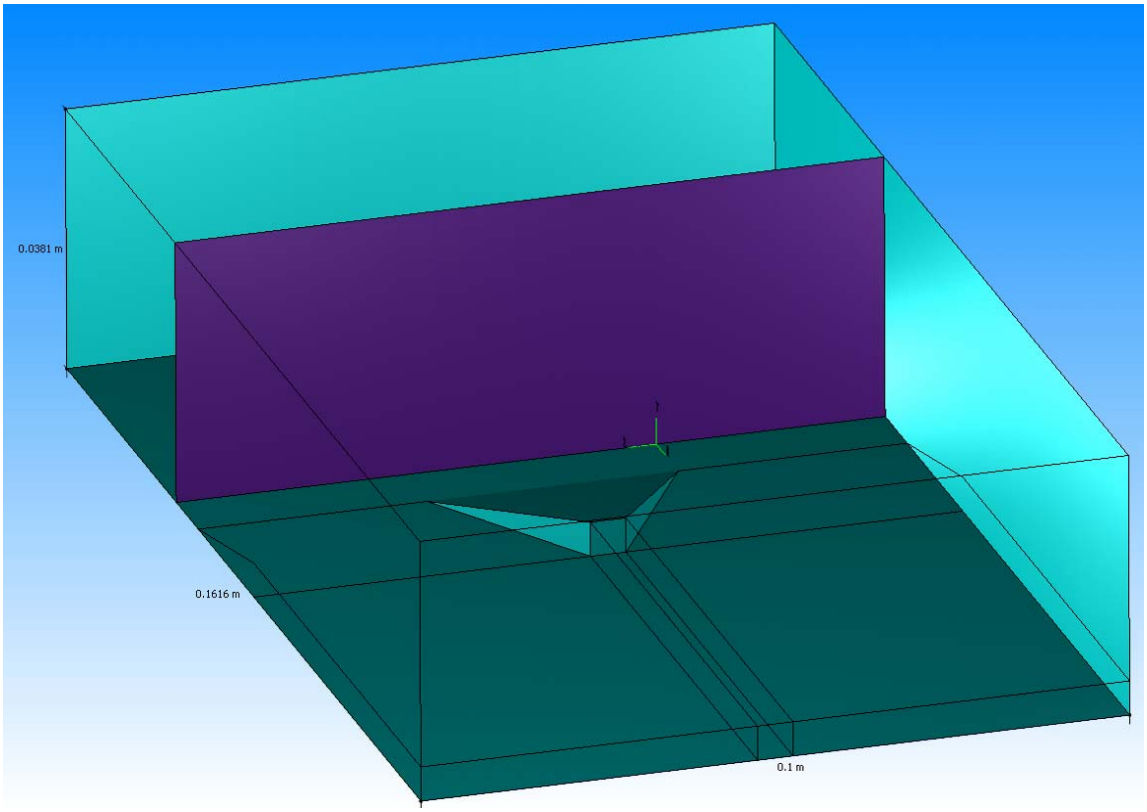

Figure 17. Example CFD-FASTRAN 3-D Aft View.

3. CFD-VIEW

The results were examined using CFD-VIEW for post-processing and visualization. This program allowed loading of individual files to examine the progress of an ongoing solution and was also capable of loading of multiple files to generate frame-by-frame animations.

Slices of the simulations revealed the instantaneous values of many variables, including density, velocity, pressure, temperature, Mach number, and turbulence intensity. The resolution of these values depended on the size of the grid processed by CFD-FASTRAN. While the three-dimensional visualization provided by CFD-VIEW is difficult to characterize with static images, the Figures 18 through 21 illustrate some of the capabilities of the program

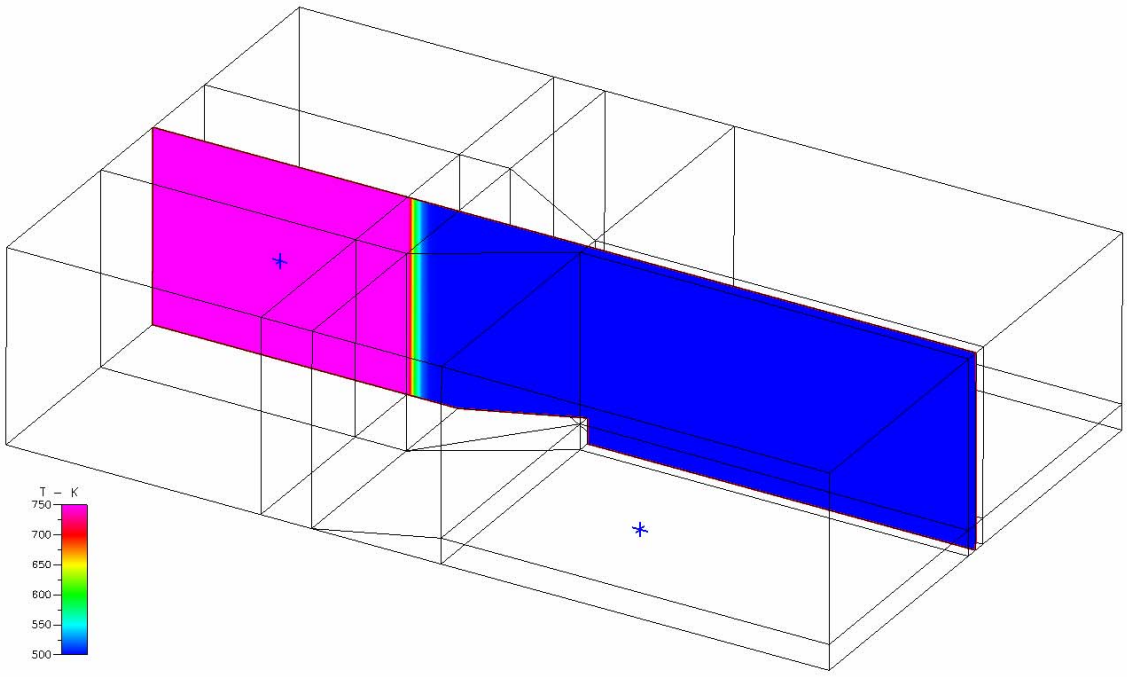

Figure 18. Example CFD-VIEW Showing Z-Axis Slice of Initial Temperature.

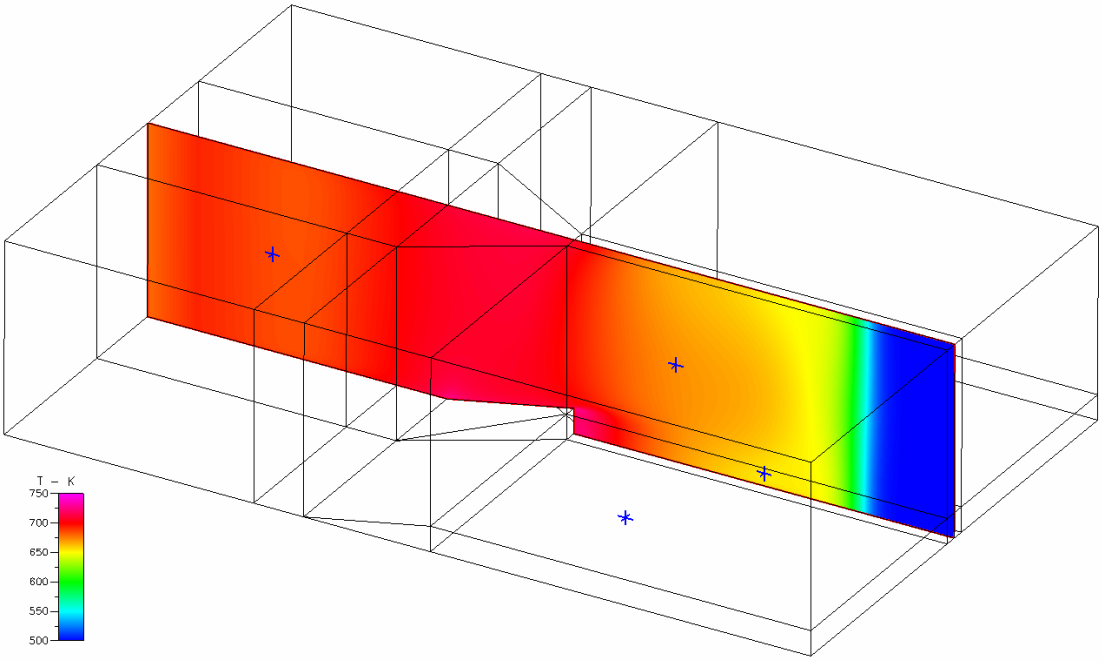

Figure 19. Example CFD-VIEW Showing Z-Axis Slice of Final Temperature.

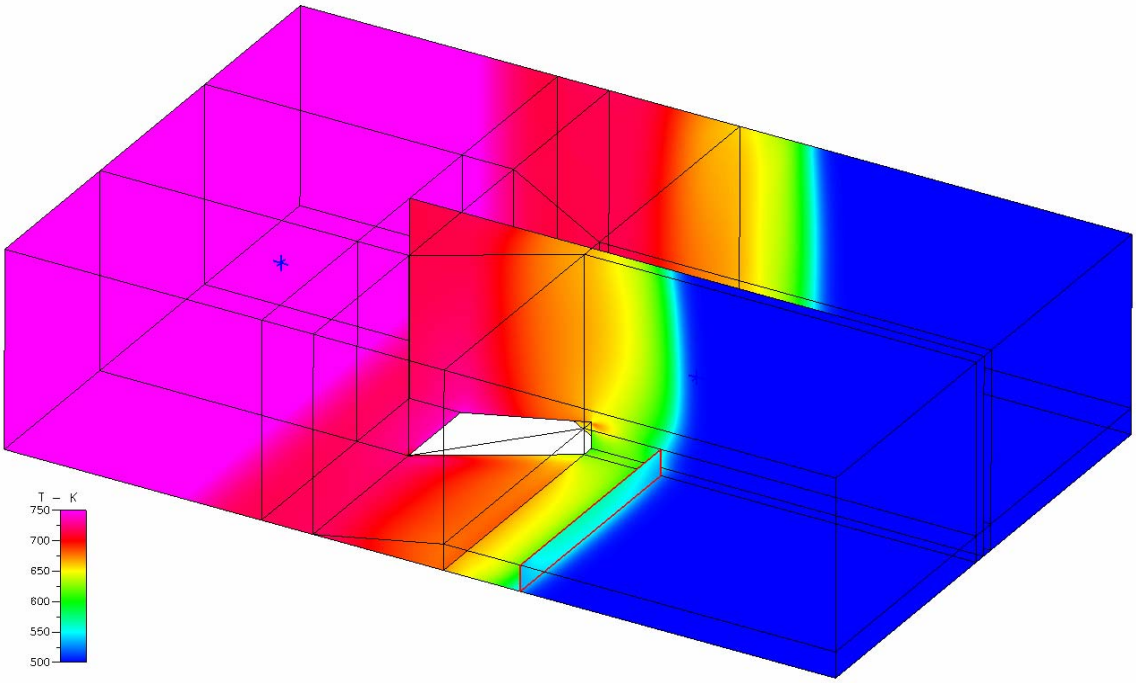

Figure 20. Example CFD-VIEW Showing Multiple-Axes Slices of Temperature.

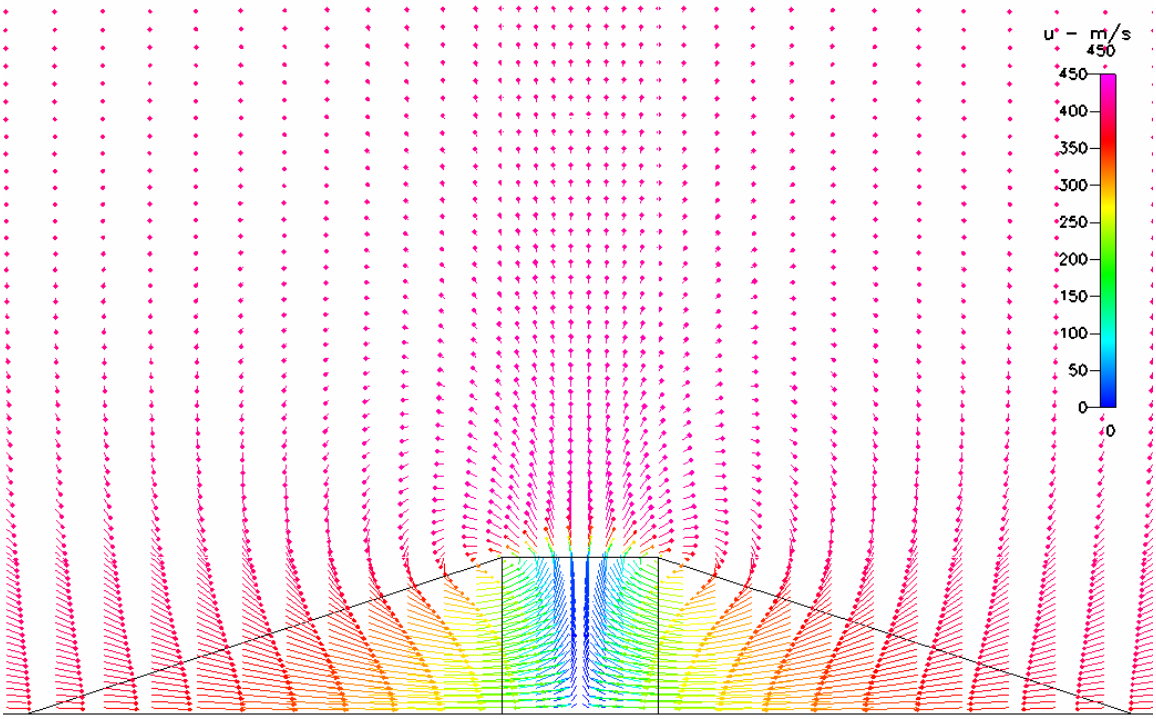

Figure 21. Example CFD-VIEW Showing Close-Up X-Axis Slice of Velocity Vectors.

B. SIMULATION SUMMARY

Two distinct types of simulation were conducted. The first type examined the steady state interactions of ramp geometries with and without base flow. The second examined time accurate characterization of shock interaction with various ramp geometries without base flow, with base flow, and with existing flow in the section. The straight ramp used was 35.4 mm wide, 25.4 mm in length, with 5 mm ramp height, for an approximate 11.14 degree incline. The swept ramp had the same baseline dimensions but included an 11.14 degree sweep (Figure 22). These dimensions were chosen based those already evaluated in supersonic ramp injector studies [12]. A summary of all 3-D CFD-FASTRAN simulations conducted is included in Tables 2 and 3, and described in the following sections. Specific parameters entered in CFD are included in Appendices A and B.

1. Steady State Base Flow Interactions

Initial modeling examined the steady state interactions of straight and swept ramps with base flow. These simulations examined mixing and total pressure gradients

for straight ramps and swept ramps with varying external flow velocities and base flow velocities. As seen in the Figures 23 and 24, these simulations demonstrate the effectiveness of base flow in reducing total pressure losses.

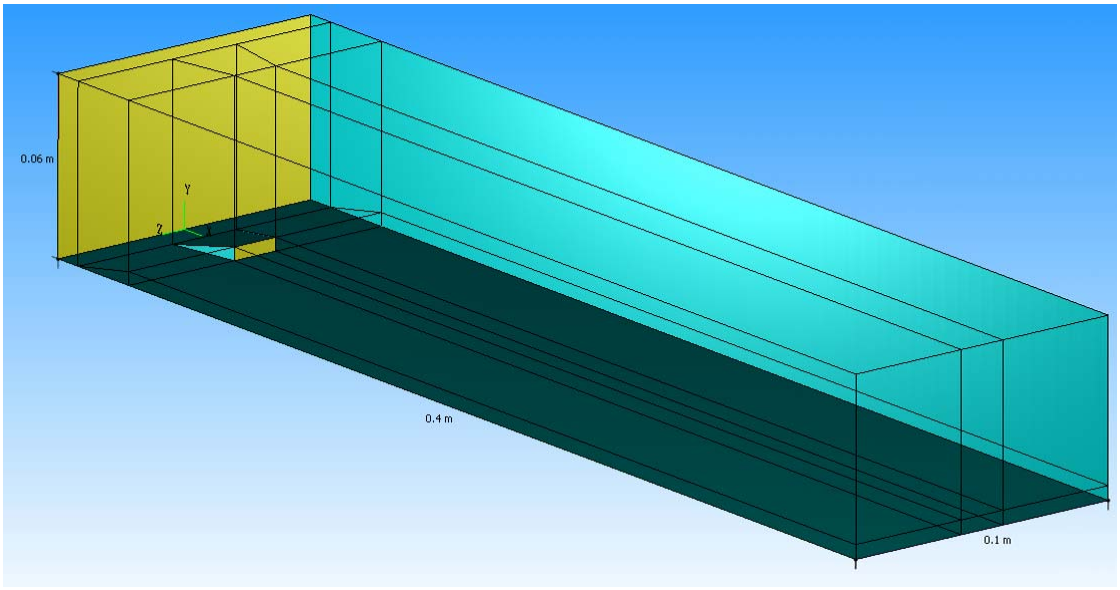

Figure 22. Steady State Swept Ramp CFD Geometry.

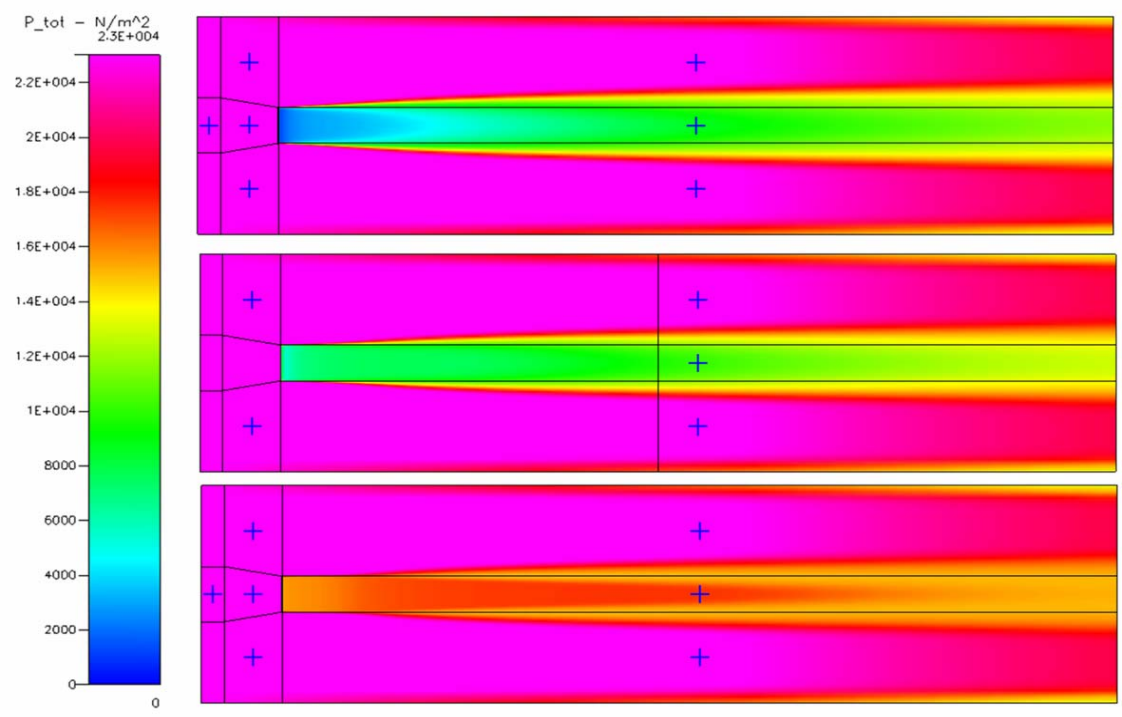

Figure 23. Steady State Swept Ramp Top View Comparison, U=200 m/s: Base Flow of 0, 50, and 150 m/s.

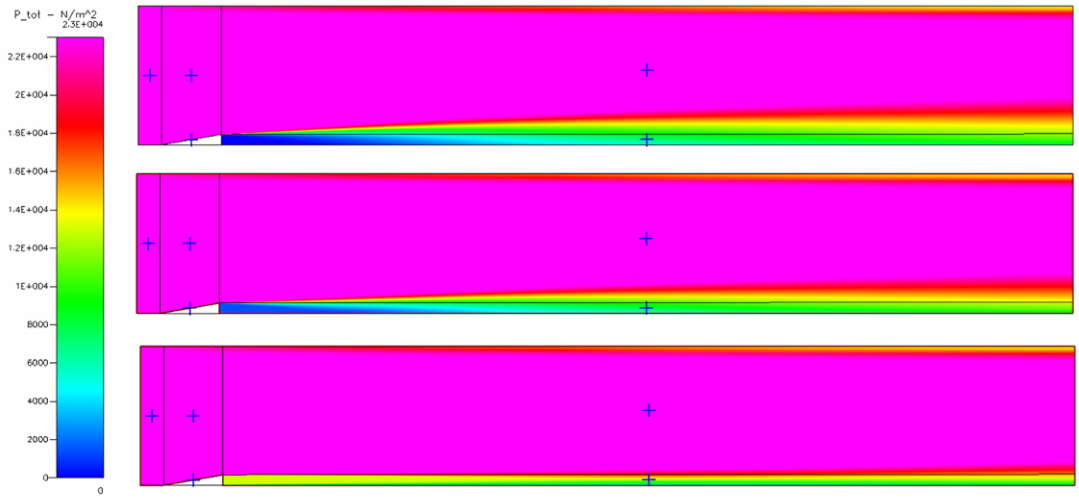

Figure 24. Steady State Swept Ramp Side View Comparison, U=200 m/s: Base Flow of 0, 50, and 150 m/s.

	Volume Initial Flow (m/s)	**Base Flow (m/s)**
Straight Ramp	100	--
Straight Ramp	200	--
Swept Ramp	100	--
Swept Ramp	200	--
Swept Ramp	200	50
Swept Ramp	200	100
Swept Ramp	200	150

Table 2. CFD Steady State Simulation Summary.

	Shock Mach Number	Volume Initial Temperature (K)	Volume Initial Flow (m/s)	Base Flow (m/s)
Straight Ramp	2	300	--	
Straight Ramp	2	500	--	
Straight Ramp	3	300		
Straight Ramp	3	500		
Straight Ramp	2	500		225
Straight Ramp w/troughs	2	500		
Swept Ramp	2	500		
High-Sweep Swept Ramp	2	500		
High-Sweep Swept Ramp	2	500	90	

Table 3. CFD Time Accurate Simulation Summary

2. Time Accurate Straight Ramp Simulations

Initial modeling of the time accurate models attempted to bracket the extremes of the conditions of interest. These conditions were Mach 2 and Mach 3 shocks, with initial medium temperature of 300 and 500 K, using a single straight ramp as seen in Figure 25. Based on the qualitative results of these simulations, a Mach 2 shock with 500 K initial temperature showed the most promising interactions and was chosen for use with all subsequent geometries. Straight ramps simulations were also conducted with a base flow at 225 m/s.

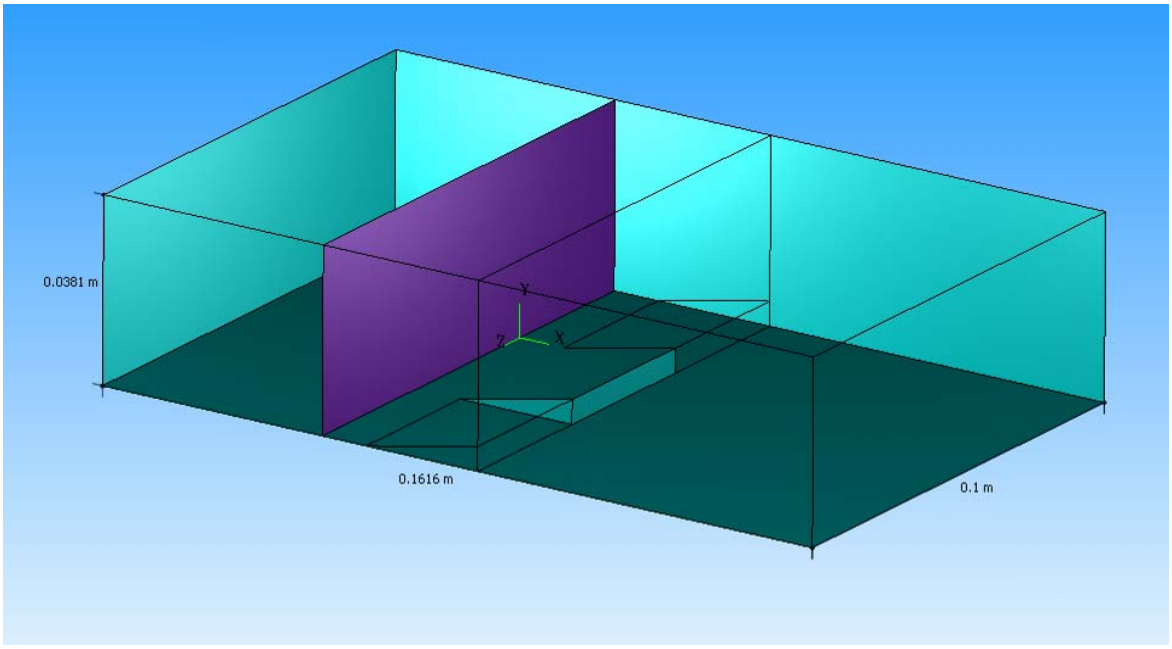

Figure 25. Time Accurate Straight Ramp CFD Geometry.

3. Time Accurate Straight Ramp with Trough Simulation

With these conditions, a straight ramp with identical geometry but with troughs behind the ramp was simulated (Figure 26). The purpose of this geometry was to examine the possible effects of shock focusing to develop hotspots downstream of the ramp. It was inconclusive and not explored further in simulation or experimentation.

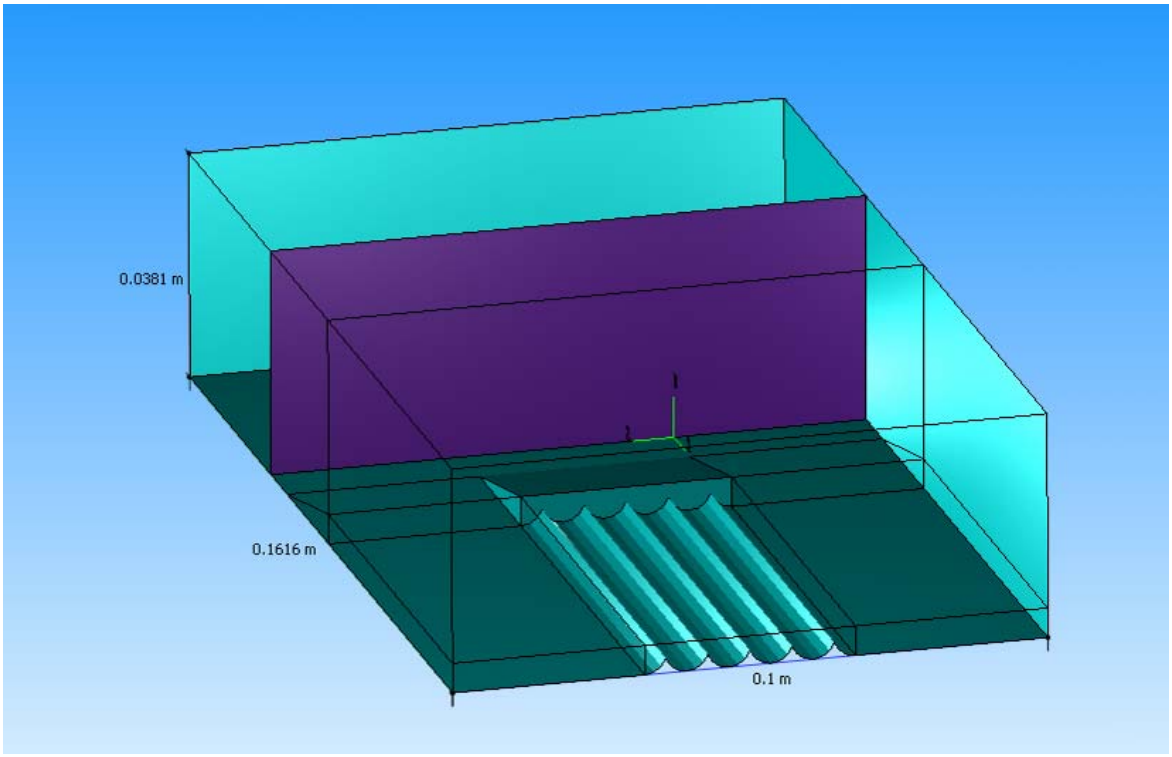

Figure 26. Time Accurate Straight Ramp with Troughs CFD Geometry.

4. Time Accurate Swept Ramp Simulation

Using a similar geometry, a swept ramp was constructed with an 11.14 degree sweep equal to the slope of the straight ramp (Figure 27). The results showed increased turbulence and the beginning of vorticity at the ramp edges, but were not dramatically different than the straight ramp and a more aggressive geometry was considered.

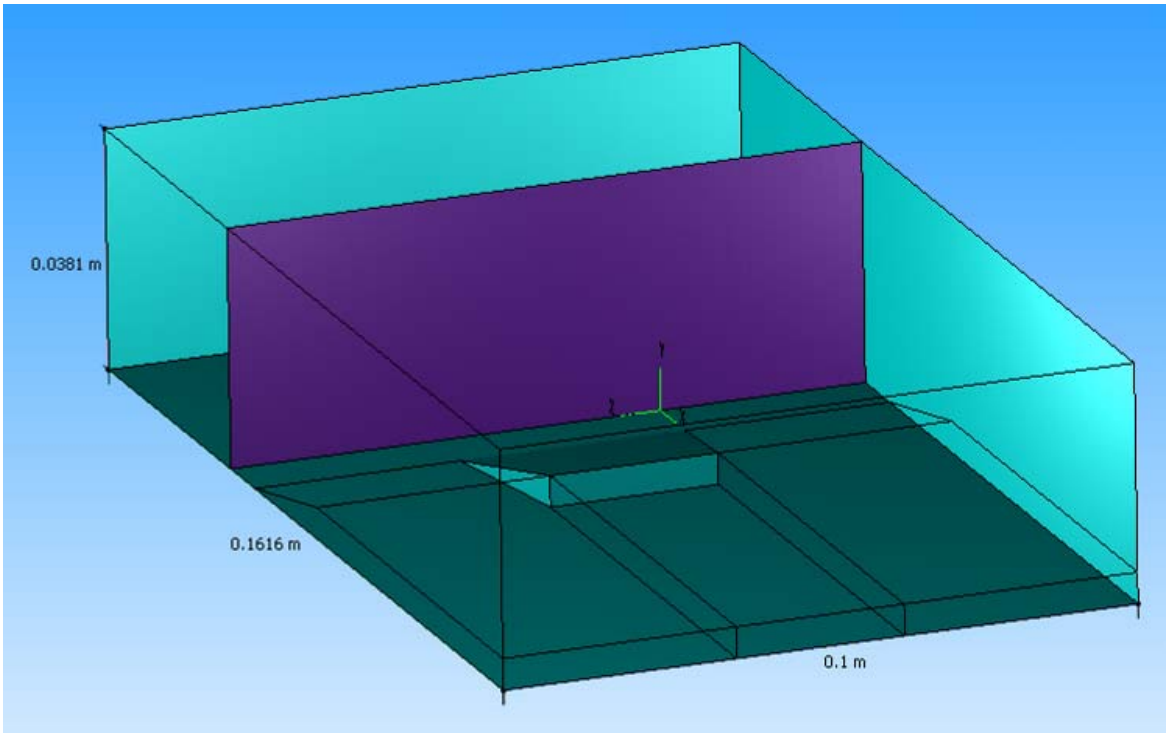

Figure 27. Time Accurate Swept Ramp CFD Geometry.

5. Time Accurate High-Sweep Swept Ramp Simulation

To further explore the swept ramp geometry, the final series of tests explored ramps with much more aggressive sweeps. Like the other ramps geometries, it had an initial width of 35.4 mm and an axial length of 25.4 mm. The high-sweep swept ramps had a much more aggressive sweep of 30.89 degrees, resulting in a square 5 x 5 mm cross-section at the base of the ramp (Figure 28).

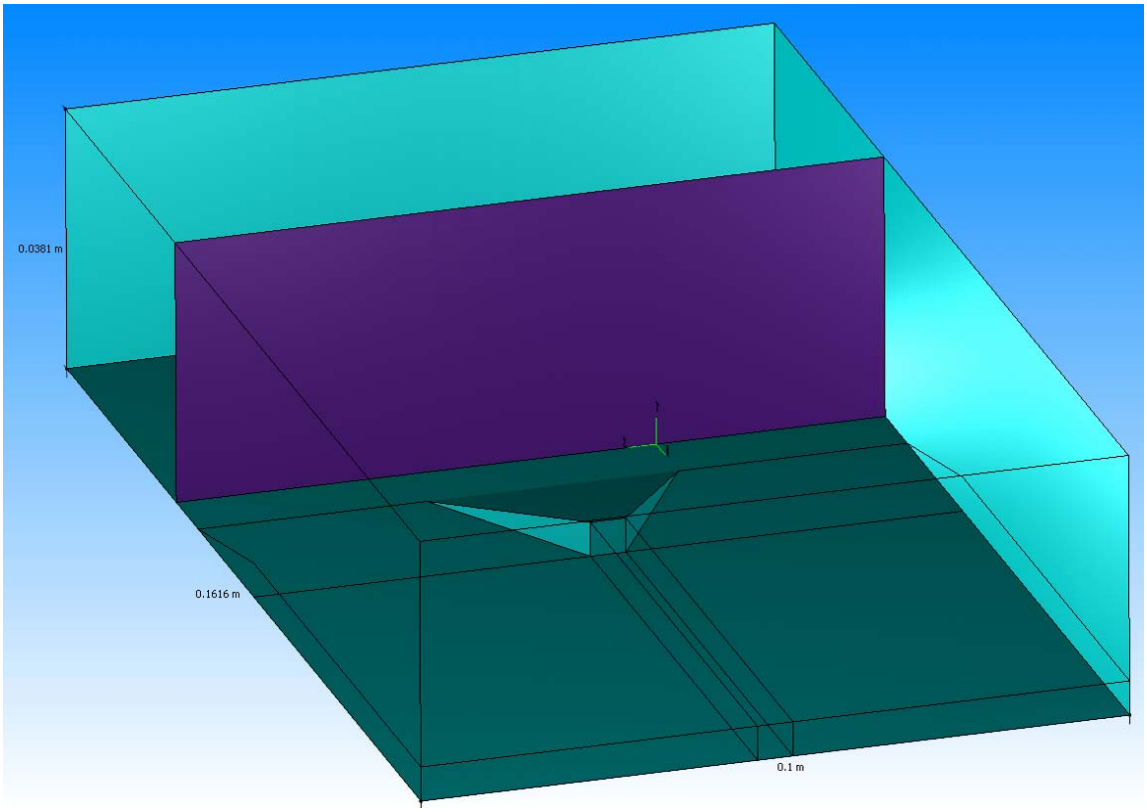

Figure 28. Time Accurate High-Sweep Swept Ramp CFD Geometry.

These final tests showed the most promising indications of all the simulations conducted. They were conducted both at static conditions and with an existing 90 m/s flow in the section. High levels of turbulence were created, with theoretically less pressure losses created than with the large surface areas behind the straight ramps. Indications of vorticity generation behind the ramps revealed the potential for flame advancement well ahead of an existing flame front as it passed the ramp due to the likelihood of small-scale generation. This might allow the flame front to accelerate locally, simultaneously increasing surface area and pulling the entire flame front forward. This vorticity can be compared in Figures 29 and 30, representing the flow velocity vectors present in a cross-sectional cut just downstream of the ramp before and after shock passage.

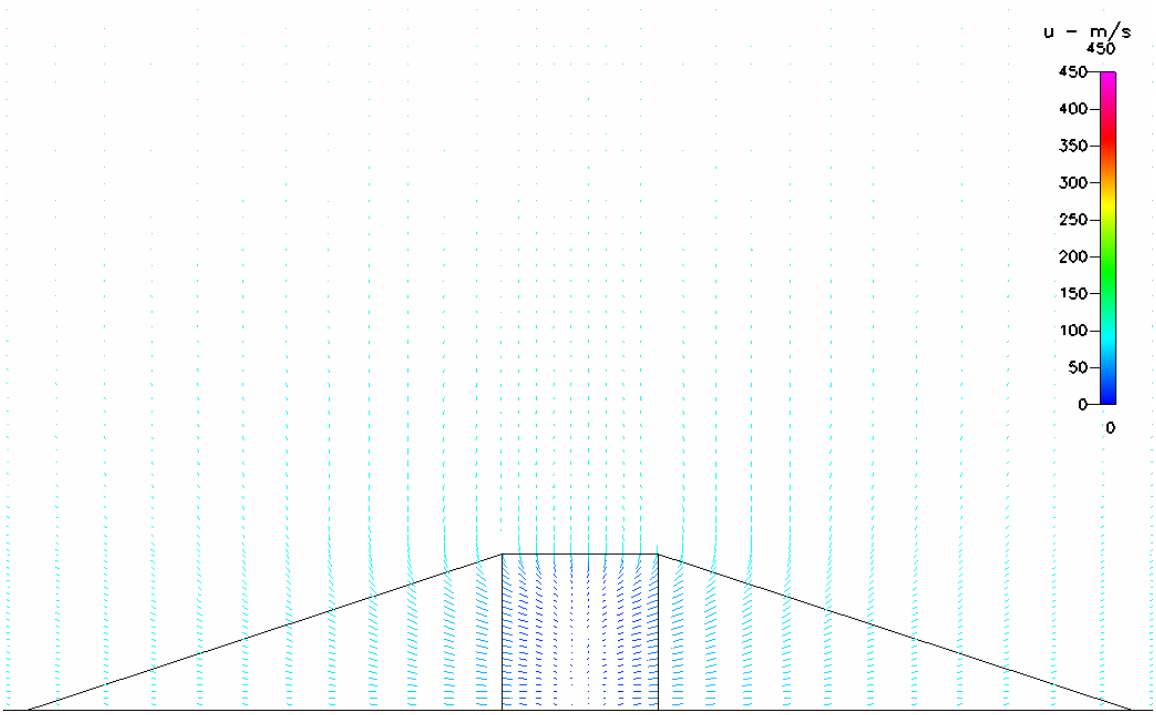

Figure 29. Flow behind High-Sweep Swept Ramp before Shock Passage.

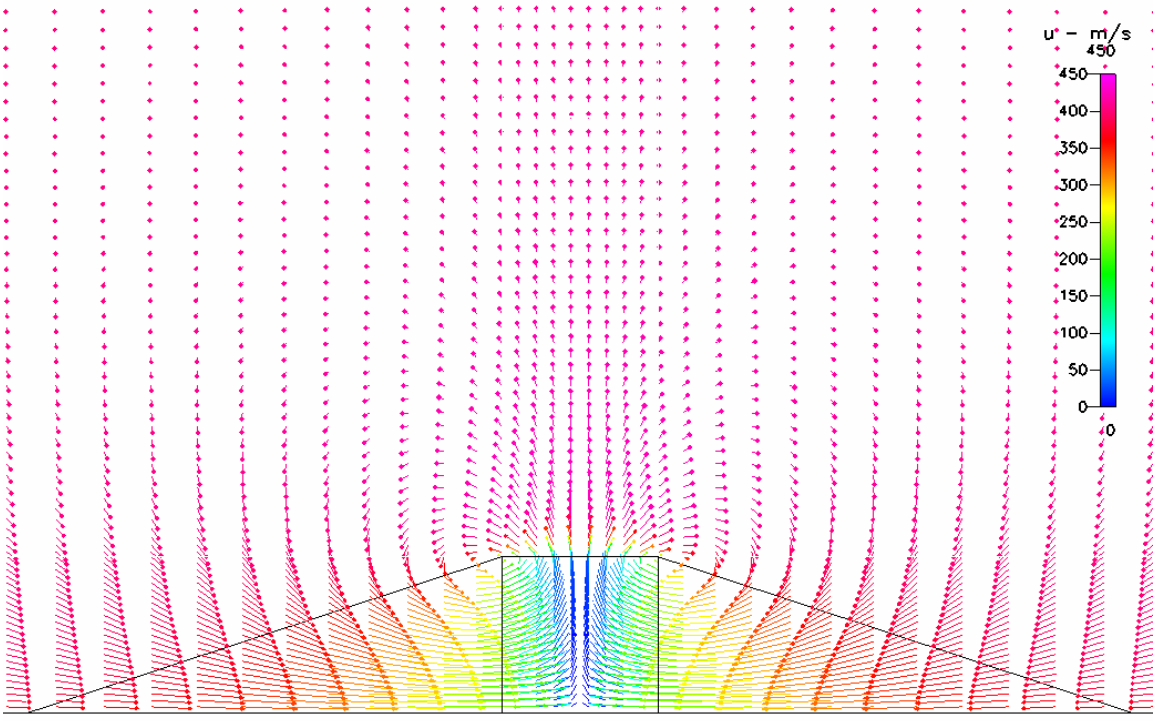

Figure 30. Vorticity behind High-Sweep Swept Ramp after Shock Passage.

IV. DESIGN/EXPERIMENTAL SETUP

The experimental research for this thesis was conducted at the Naval Postgraduate School Rocket Propulsion Laboratory Test Cell #1, shown in Figures 31 and 32. The test assembly consisted of a combustor section, shock formation tube, transition section, optical test section, and external tube. Gaseous ethylene (C_2H_4) and air were used as reactants and premixed prior to injection into the combustion section. Ignition was provided by a high capacitance igniter located at the head of the combustion section. Instrumentation included high speed acquisition of pressure and optical data, integrated with a high-speed imaging camera aimed at the optical test section. The assembly was mounted on a Newport Research Corporation optical table. All test cell actuation and instrumentation were controlled via computer from inside the control room. Camera control was through on a separate computer. The following sections describe this hardware and software in detail.

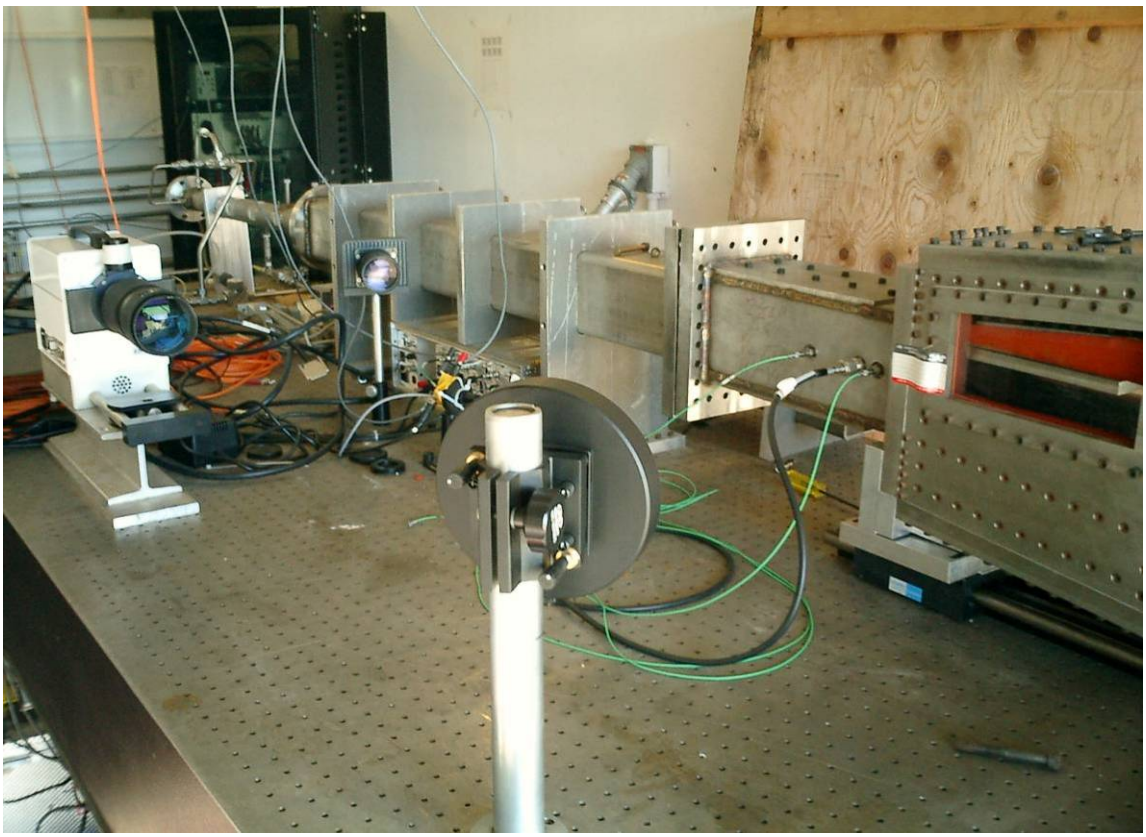

Figure 31. Test Cell #1 Experimental Setup-Aft View.

Figure 32. Test Cell #1 Experimental Setup-Forward View.

A. TEST SECTION

1. Combustor

The combustor section was comprised of a 2-inch (I.D) stainless steel tube 36 inches in length (Figure 33). The primary purpose of this section was to allow for the generation of a combustion wave and associated shock for passage into the shock formation tube. A 2-inch spiral measuring 24 inches in length with a 3/4-inch twist was inserted into the head of the combustor, as well as four threaded bolts asymmetrically placed along the test section to secure the spiral and provide additional turbulence for the initial flame acceleration. The purpose of the spiral section was to enhance mixing of reactants to ensure a uniform shock was generated before entry into the test section. Fuel and oxidizer enter the combustor approximately 3 inches from the head end via three ports arranged to maximize mixing. The combustor section was capped by the igniter plate on the head end and attached to the shock formation tube at the downstream junction.

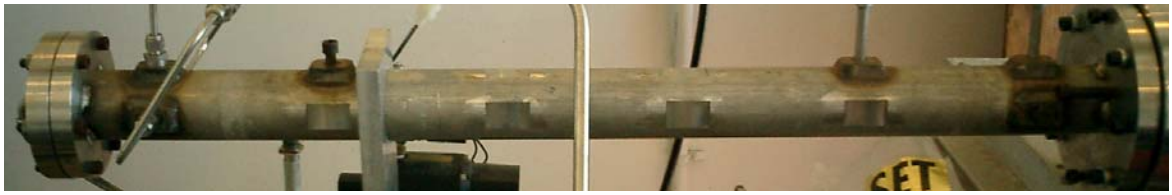

Figure 33. Combustor Section.

2. Shock Formation Tube

The shock formation tube (Figure 34) was a 48-inch long 5-inch outer diameter stainless steel square tube designed and built by Michael A. Fludovich Jr. for use in previous thesis work [13]. It was reinforced by four ribs made from one-inch aluminum plate spaced evenly along the length. The two outer ribs also provided support for mounting for the joined combustion section and shock formation tube. The purpose of this section was to provide sufficient length for the combustion shock to separate from the combustion wave and form a normal shock wave before entering the optical test section. This length also served to eliminate any transients remaining from the transition from the smaller circular combustion tube to the larger square shock formation tube. The downstream end of the shock formation tube had an o-ring seal and was attached with removable fasteners for upstream access to the optical test section.

Figure 34. Shock Formation Tube.

3. Transition Section

The transition section was also based on the Fludovich design and installed after the shock formation tube [13]. This section provided for a clean transition from the larger 4.5 x 4.5 inch inner diameter square shock formation tube with rounded corners to the shorter 4.5 x 2.9 inch square of the optical test section. Removable plates were mounted to the top and bottom interiors of this tube that extended upstream into the

shock formation tube to form the transition and test region (Figure 35). These plates extended through the optical test section into the external tube to provide a constant test region through the area of interest. Different upper plate configurations allowed for clean flow testing as well as subsequent mounting of various obstacle configurations. Obstacles were then bolted through the back of the upper plates before they were attached to the transition section.

Figure 35. Transition Section Showing Removable Plates.

The transition section also contained two transducer mounting ports spaced 10 cm apart axially along the centerline of one side of the tube, as seen in Figure 42. These ports housed Kistler pressure transducers used to accurately determine shock speed just prior to the test section. Two additional ports were located opposite each other on either side of the tube, in the center of the flow path. One of these was sealed, while the other held an optical sensor used to detect passage of the flame front to provide triggering date to the high speed camera.

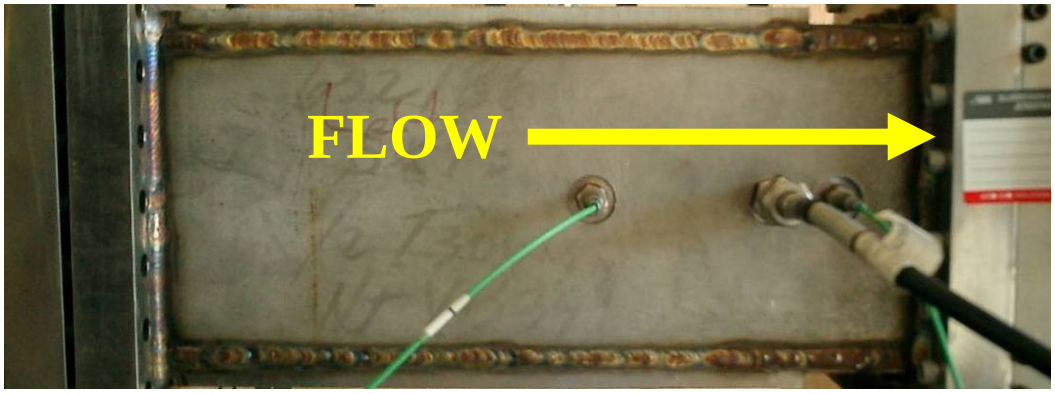

Figure 36. Transition Section Detail Showing Pressure Transducers and Optical Sensor.

The transition section was attached to the optical test section and both were hard mounted to a sliding roller bearing assembly attached to the test table, as seen in Figure 37. This arrangement allowed these two sections to be detached from the remainder of the assembly and translated aft between tests, allowing access to the transition section for mounting of different obstacle configurations.

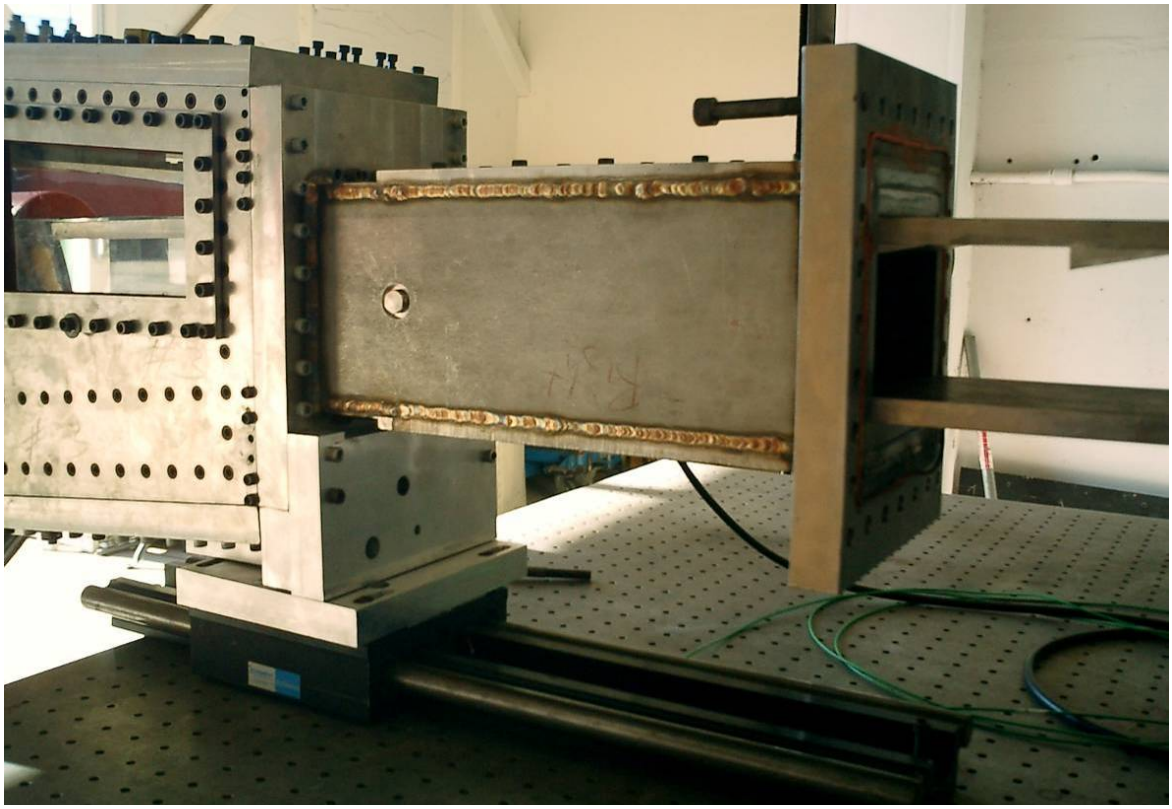

Figure 37. Transition Section and Optical Test Section on Sliding Assembly.

4. Optical Test Section

The optical test section was built on the Fludovich nozzle design [13], with nozzle components removed and replaced by plates extending from the transition section. The primary features of this section were the two 1.2-inch thick optical windows mounted flush with the section walls that formed either side of the imaging area. The aft end of the optical test section held a mounting bracket for the external tube. Figures 38 and 39 show the optical test section in more detail.

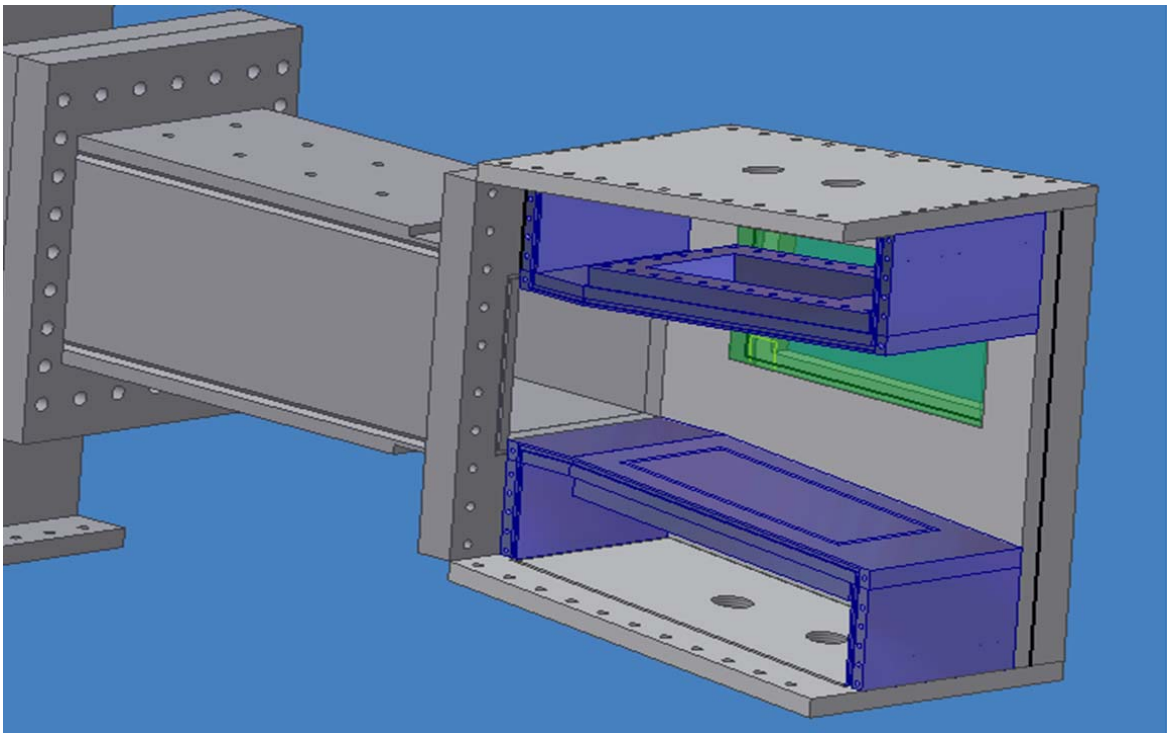

Figure 38. Optical Test Section CAD Model (From [14]).

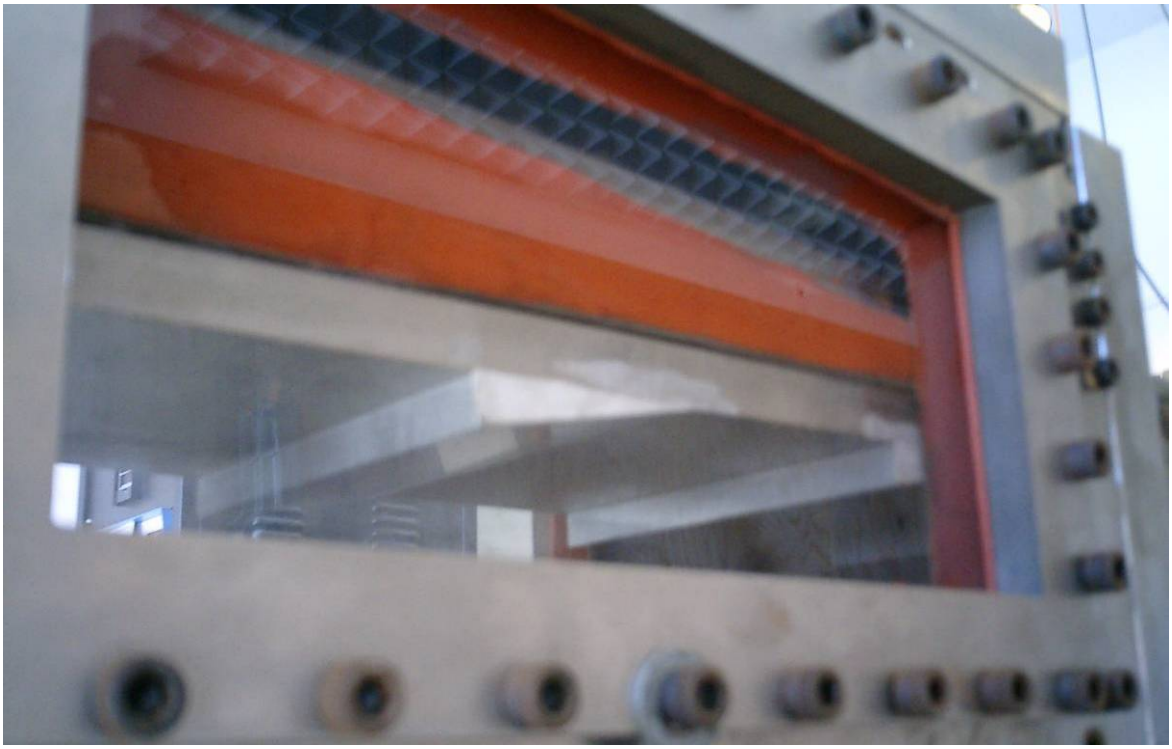

Figure 39. Optical Window Detail.

5. External Tube

The external tube was a removable square tube mounted aft of the optical test section (Figure 40). Its purpose was to isolate the test section from ambient flow disturbances present in the test cell area, and to direct the shock and combustion away from the test table and instrumentation. Two Kistler pressure transducers were mounted 15.24 cm apart along the top of the external tube. These sensors were used to accurately determine shock speed after the test section and compare it with the earlier velocity measurement. Two outer ribs were added to the external tube to increase mass and reduce vibration sensitivity during shock transition. The aft end of the external tube terminated inside the test cell exhaust tube. This tube provided a path away from the test cell for the shock and combustion products, and aided in damping acoustic noise present in the control room.

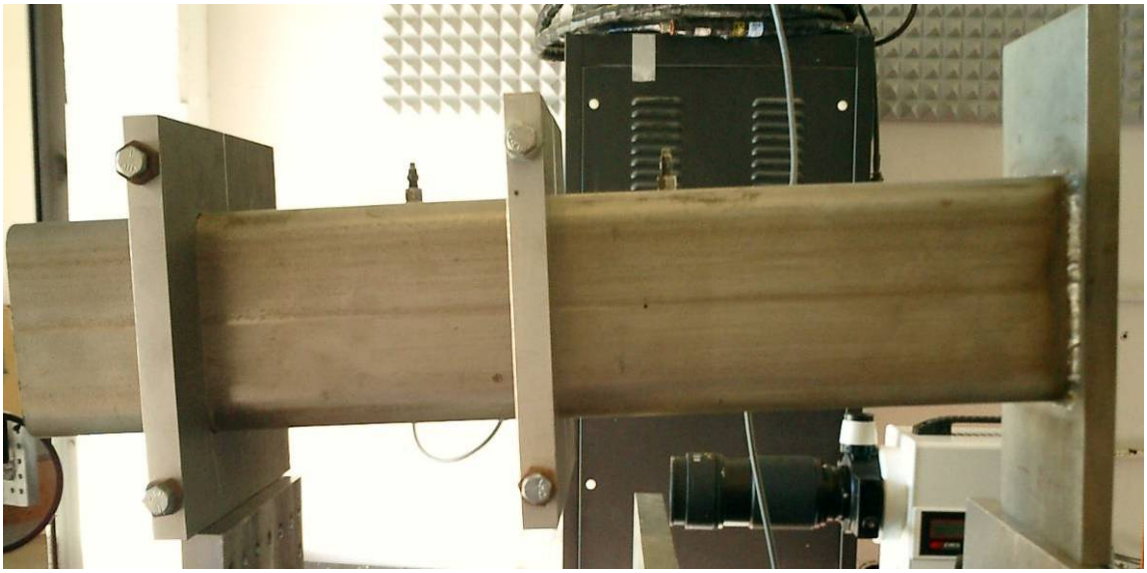

Figure 40. External Tube.

B. AIR AND FUEL DELIVERY

The test cell was provided high pressure air from the RPL common supply shared with all of the test cells and ethylene from a dedicated bottle supply. Both were regulated by Tescom ER3000 Version 2.0 software on the main RPL00 computer, controlling associated pressure regulators in the test cell and bottle room. These provided independently selectable pressures of each gas to the test table via 1/2-inch pipes. Two Omega PX-5500 pressure transducers were installed on the optical table to obtain high accuracy values. Each was placed immediately prior to Swagelok ball valves located on the test table. These ball valves were pneumatically actuated by an independent shop air supply line, but electrically controlled from LabVIEW through Crydom control solenoid switches in the test cell.

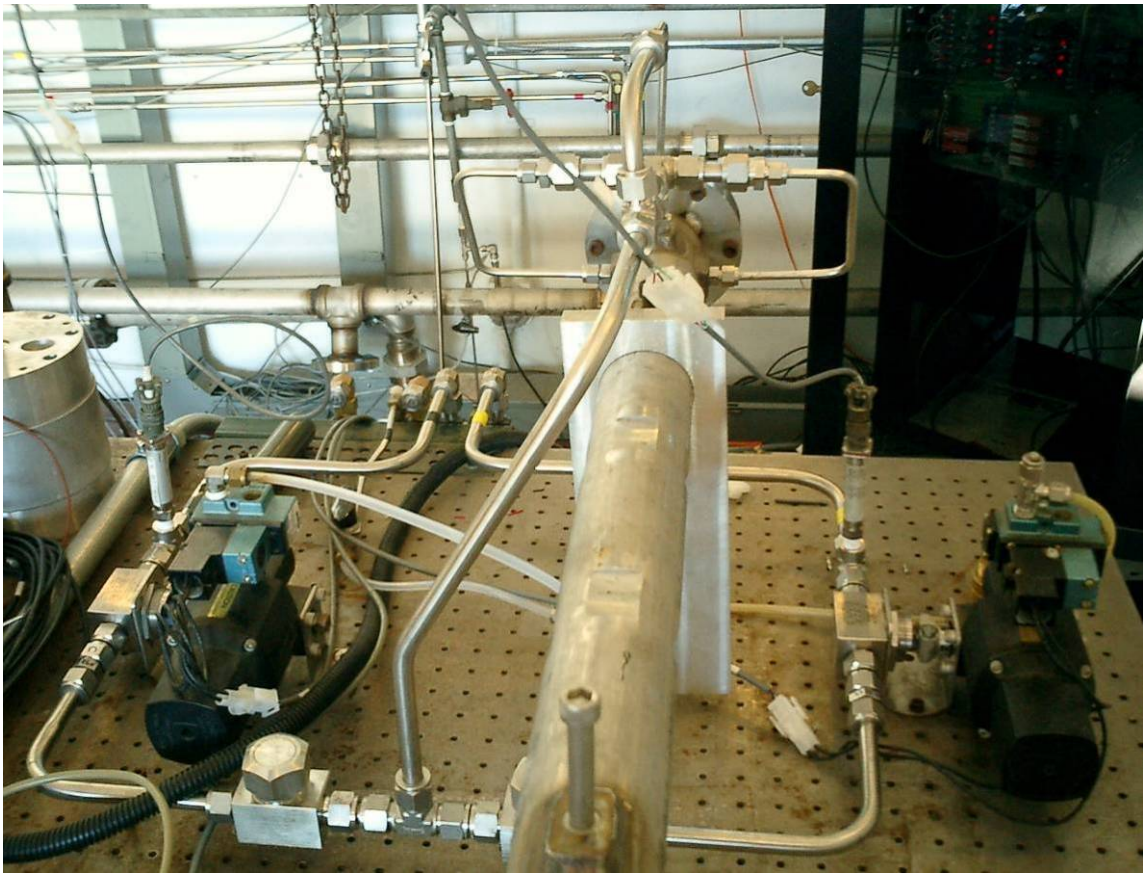

Figure 41. Air and Fuel Delivery System.

Choked orifices immediately followed each ball valve, providing metering of the mass flow rates for each gas and was controllable by varying upstream pressure. Choke diameters were selected as 0.0292 inches for ethylene and 0.0425 inches for air, based on the pressures required to achieve the desired mass flow rates. Each metered 1/2-inch supply line then passed though a one-way isolation valve before the gases were combined. This arrangement protected from backflow after combustion and allowed flow of high pressure air alone during initial and final air purge stages. The combined flow was routed to maximize mixing, and then split into three 1/4-inch lines before injection into the combustor section (Figures 41 and 42).

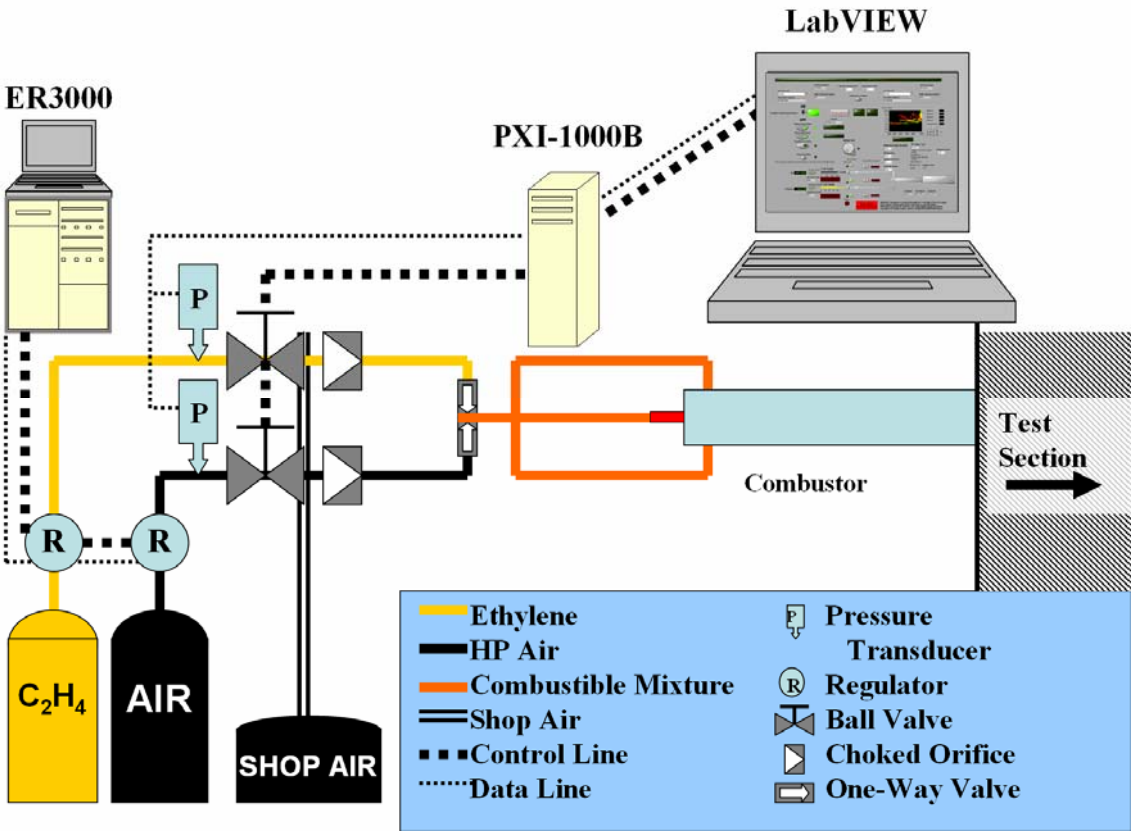

Figure 42. Schematic of Air and Fuel Delivery System.

C. IGNITION SYSTEM

The ignition system used was the Unison Vision-8 Variable Ignition System (VIS-8), a capacitive discharge system with an aviation-grade spark plug mounted in the head end of the combustor section (Figure 43). Preconfigured via manual entry, the system was capable of being remotely triggered by computer on command from the control room. The high voltage transient present upon ignition initiation also provided the trigger for high-speed data acquisition.

Figure 43. Unison Ignition System with Igniter.

D. INSTRUMENTATION

The test cell contained several different types of instrumentation for test initialization and data collection (Figure 49). Pressure and optical data were routed through one of four National Instruments 14-bit (NI) PXI-6115 cards mounted in the NI PXI-1000B chassis located in the test cell (Figure 44). This chassis interfaced via a NI PXI-MXI-4 PXI Bridge with the RPL05 desktop computer in the control room and was capable of real time data collection or high-speed buffered data acquisition. Optical data were collected from the cameras via fiber-optic lines or direct connection and routed to

either a dedicated desktop computer in the control room or a dedication laptop in the test cell. Additionally, a closed-circuit video camera system was positioned above the test cell to record each experimental run. Video collected by this system was used for presentation purposes, but was primarily a safety feature and will not be discussed further.

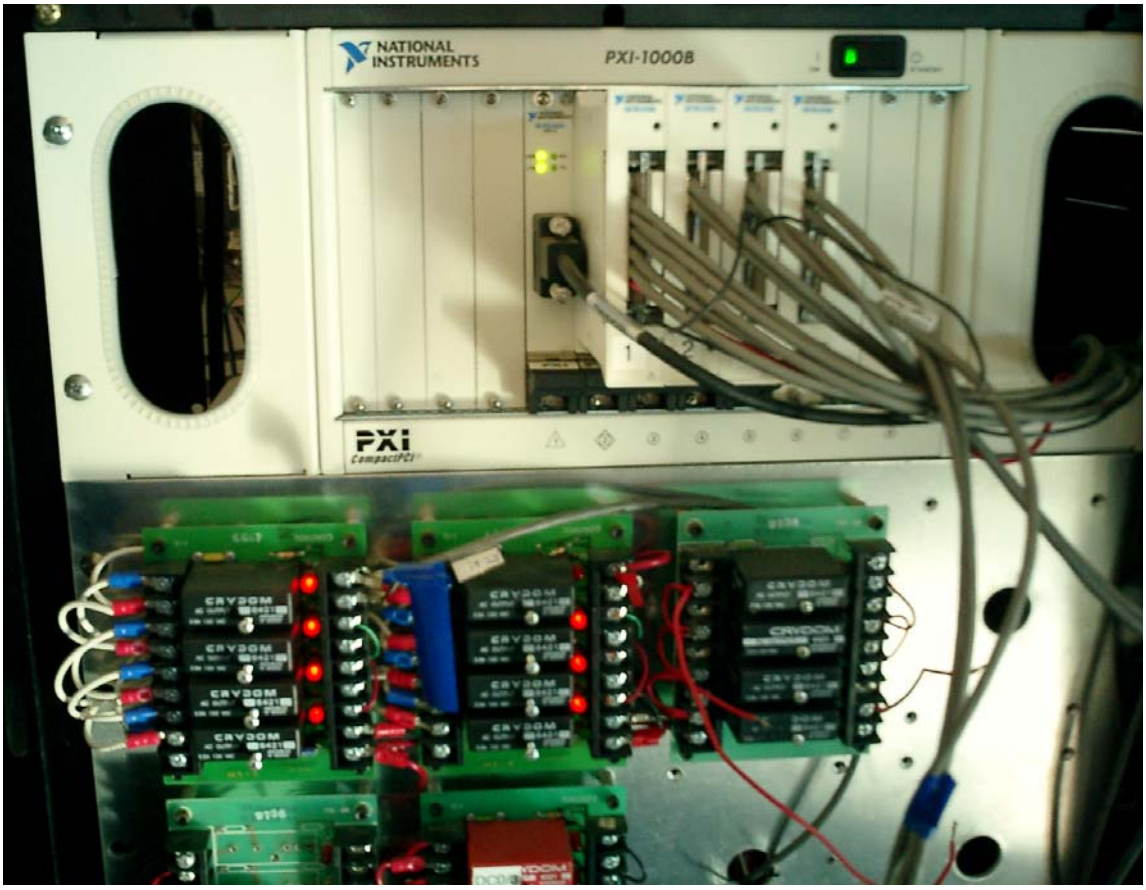

Figure 44. PXI-1000B Rack and Crydom Control Solenoid Switches.

1. Pressure Transducers

Two Omega PX-5500 pressure transducers were located upstream of the chokes in the air and fuel delivery lines, rated at 3000 and 1000 psi respectively. Measurements from these transducers were collected and sent directly by to the control room to ensure that the correct pressures were present for the desired mass flow rates through the chokes. Data from these sensors were also collected after test initiation for performance comparison.

2. Dynamic Pressure Transducers

Four high-frequency Kistler dynamic pressure transducers were mounted in pairs before and after the test section, and connected to Kistler Type 5010 Dual Mode Amplifiers. Amplified data were routed to two PXI-6115 cards in the cell for high-speed data acquisition. After proper initialization from the control computer, these cards were configured to trigger on the ignition event and begin collecting data at a 500 MHz sample rate to match the response rate of the Kistler transducers. The high-speed data resided in the card buffer until completion of the test and the buffer was then read and stored by the computer without loss of data or risk of hang-ups in the control program. Pressure data from the Kistler transducers provided extremely high temporal resolution of shock passage, allowing for very accurate calculation of the shock speed.

3. Optical Sensor

An optical sensor was placed 13.8 cm prior to the imaging section to detect passage of the frame front. Located between the two forward Kistler transducers, the optical sensor provided a reliable trigger to begin the high-speed imaging sequence. Prior to the camera input, the signal from this sensor passed through an intensity amplifier. The signal was the routed through a low-noise pre-amplifier/band-pass filter used to eliminate false triggers from the ignition event. Data from the optical sensor were also routed to the high-speed data acquisition card and integrated with pressure data.

4. Ultra 17 High-Speed Imaging System

Imaging of the optical test section was initially obtained using an Intensified Ultra 17 CCD camera from DRS Data & Imaging Systems, Inc (Figures 46 and 48). The Ultra 17 had capability of imaging and storing 17 high speed frames per test run. Image resolution was 512 x 512 pixels per frame with a 12-bit dynamic range, and a sample image is shown in Figure 45. The Ultra 17 was equipped with an image intensifier, allowing extremely low exposure times without the requirement for artificial external illumination. Intensifier gain could be increased up to 15,000x in 100 discrete steps. The system was capable of up to 150,000 frames per second and exposure times as low as 20 nanoseconds [15].

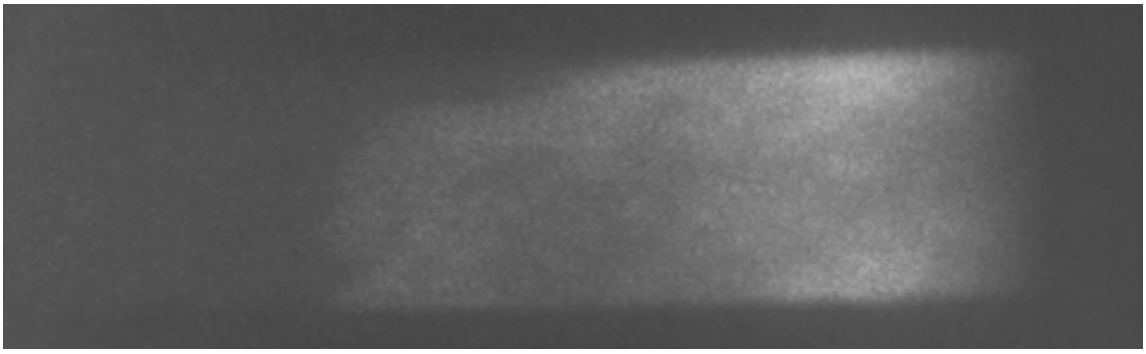

Figure 45. Sample Ultra Image (Flow R-L).

This Ultra camera was controlled from a dedicated desktop computer via a Hotlink/fiber optic connection and triggered directly by the optical sensor. A Nikon ED AF NIKKOR 80-200mm 1:2.8 telephoto lens attached to the camera was typically set with an f-stop of 8 and focused on the interior of the nearest optical window. The camera was mounted approximately 1.3 meters from the optical test section, using a table-mounted mirror for alignment of the optical path. This placement facilitated alignment and focusing of the imaging area and isolated the sensitive camera components from the direct vicinity of the optical window and the exit plane of the test section.

A two-way fiber optic link allowed the camera sequence to be initialized and the camera to be armed remotely. Imaging data fed directly back to the control computer in the control room for viewing and archiving [15]. Control and analysis of Ultra imaging was accomplished through the Ultra computer program, and will be discussed in more detail in the next section.

The Ultra camera failed approximately halfway through the testing phase. The malfunction was believed to be due to the control timing oscillator. The camera was left in place in the test cell with the expectation that it would be possible to repair and resume imaging. Unfortunately, the Ultra had not yet been returned to service by the time of this writing.

Figure 46. Ultra 17 and RDT+ Cameras (L-R)

5. Lightning RDT^{Plus} High-Speed Digital Camera

The Ultra was substituted by an RDT+ CMOS imager, also from DRS Data & Imaging Systems, Inc (Figures 46 and 48). The RDT+ had capability of imaging and storing 16,380 full high-speed frames per test run. Image resolution was 512 x 512 pixels per frame with a 10-bit dynamic range, up to 5,000 frames per second with full resolution. The RDT+ also had an operator-selectable capability of up to 100,000 frames per second by reducing the CCD read-area and effectively decreasing resolution (Figure 47). This system was capable of exposure times down to 4 microseconds [16].

Figure 47. Sample RDT+ Image (Flow R-L).

The RDT+ was controlled in a different manner than the Ultra, requiring a dedicated laptop that was constrained to the test cell because of cabling limitations. The camera had a much larger buffer size than the Ultra, eliminating the requirement for precise timing and delay from the optical sensor trigger. To reduce unnecessary data collection, however, the optical sensor was retained as an immediate trigger for the RDT+ camera.

A 75mm F1.4 C-mount lens provided by DRS was attached to the camera and set with an f-stop of 1.4 and focused on the interior of the nearest optical window. The camera was mounted approximately 1.6 meters from the optical test section. It used the same table-mounted mirror placement as the Ultra, realigned for the RDT+. Imaging data from the RDT+ fed directly to a dedicated laptop located in the test cell and could be viewed in the test cell, but had to be transferred via a USB flash memory drive for archiving.

Camera control and data analysis for the RDT+ system was accomplished by the MiDAS program on the laptop and will be discussed in more detail in the next section.

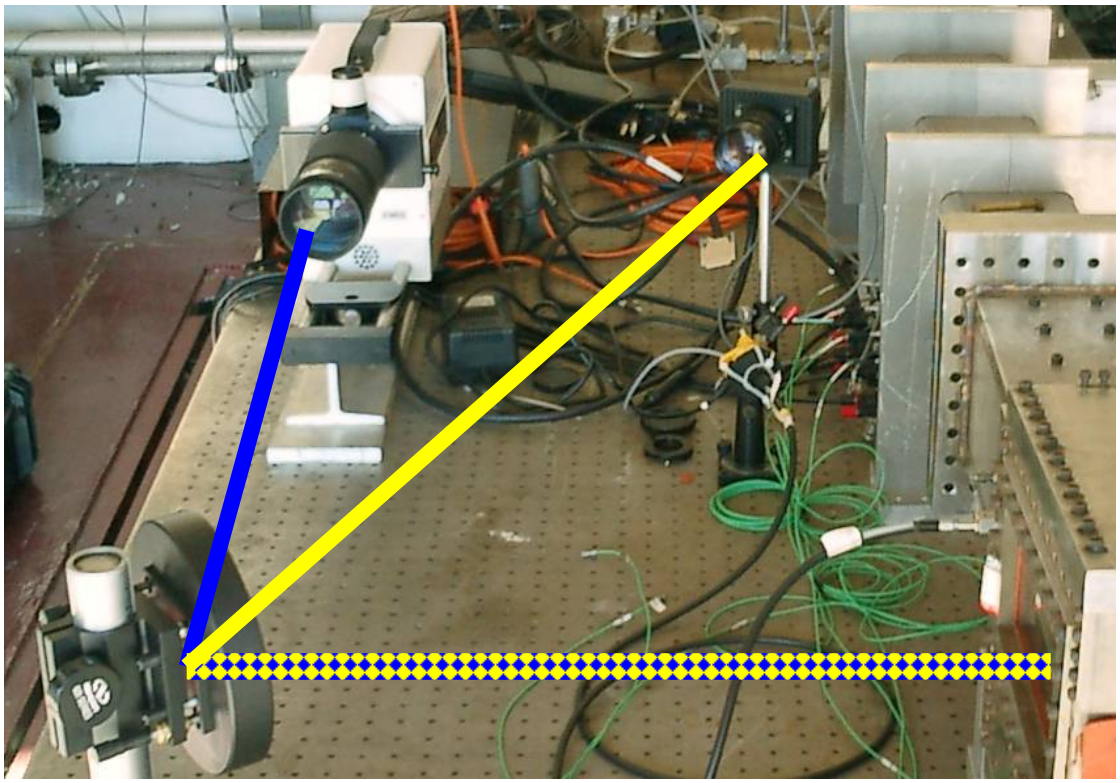

Figure 48. Diagram of Camera Optical Paths: Ultra 17 (Blue) and RDT+ (Yellow).

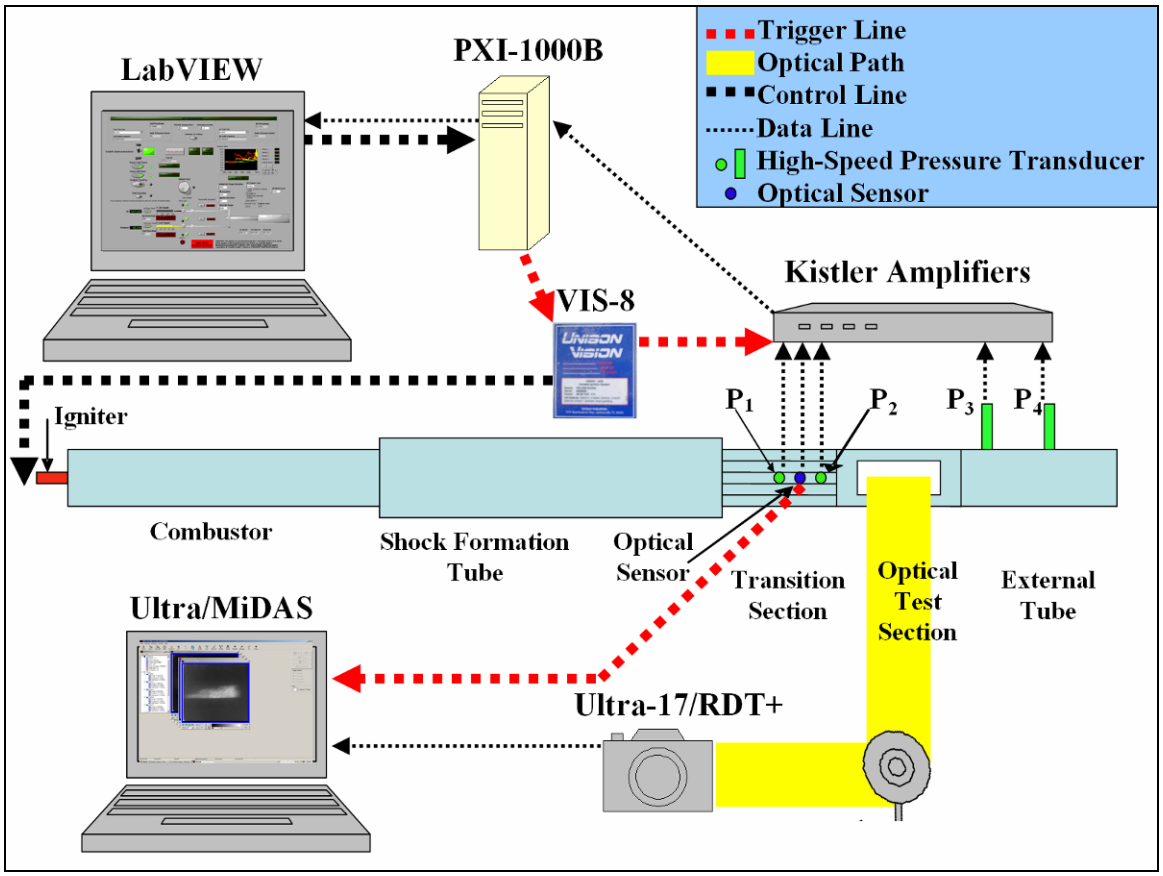

Figure 49. Schematic of Ignition and Instrumentation.

E. SOFTWARE DESCRIPTION AND FUNCTIONS

The graphical user interface software used in the setup and execution of the experimental procedure was designed to provide maximum safety and flexibility, automated execution and data recording, and useful visualization and situational awareness cues to the user during testing. Cequel was used during software development for the calculation of combustion properties. The primary means of control was a LabVIEW program executed on a Dell Dimension 8200 desktop equipped with an Intel Pentium 4 CPU processor with a clock speed of 2.20 GHz/512 MB RAM. The Ultra program was used for Ultra 17 camera control and data acquisition, and executed on a Dell Optiplex GX620 desktop equipped with an Intel Pentium D CPU 3.00GHz/1GB RAM. The Midas program was used for RDT+ camera control and data acquisition, and executed on a Sharp Pc-UM30W laptop equipped with an Intel Pentium 3 Mobile CPU 886MHz/256MB RAM. The operating system of all computers was Microsoft Windows

XP Professional Version 2002 Service Pack 2. The two desktops were located adjacent to each other in the control room and the laptop was normally located in the test cell.

1. Cequel

Preliminary analysis of reaction characteristics was conducted using the Cequel Toolbox: Chemical Equilibrium in Excel Version 1.75 from Software and Engineering Associates, Inc. /Spreadsheet World, Inc (Figure 50). This plug-in, used with Microsoft Excel 2002 Service Pack 2, allowed detailed examination of the theoretical combustion characteristics of many different compounds.

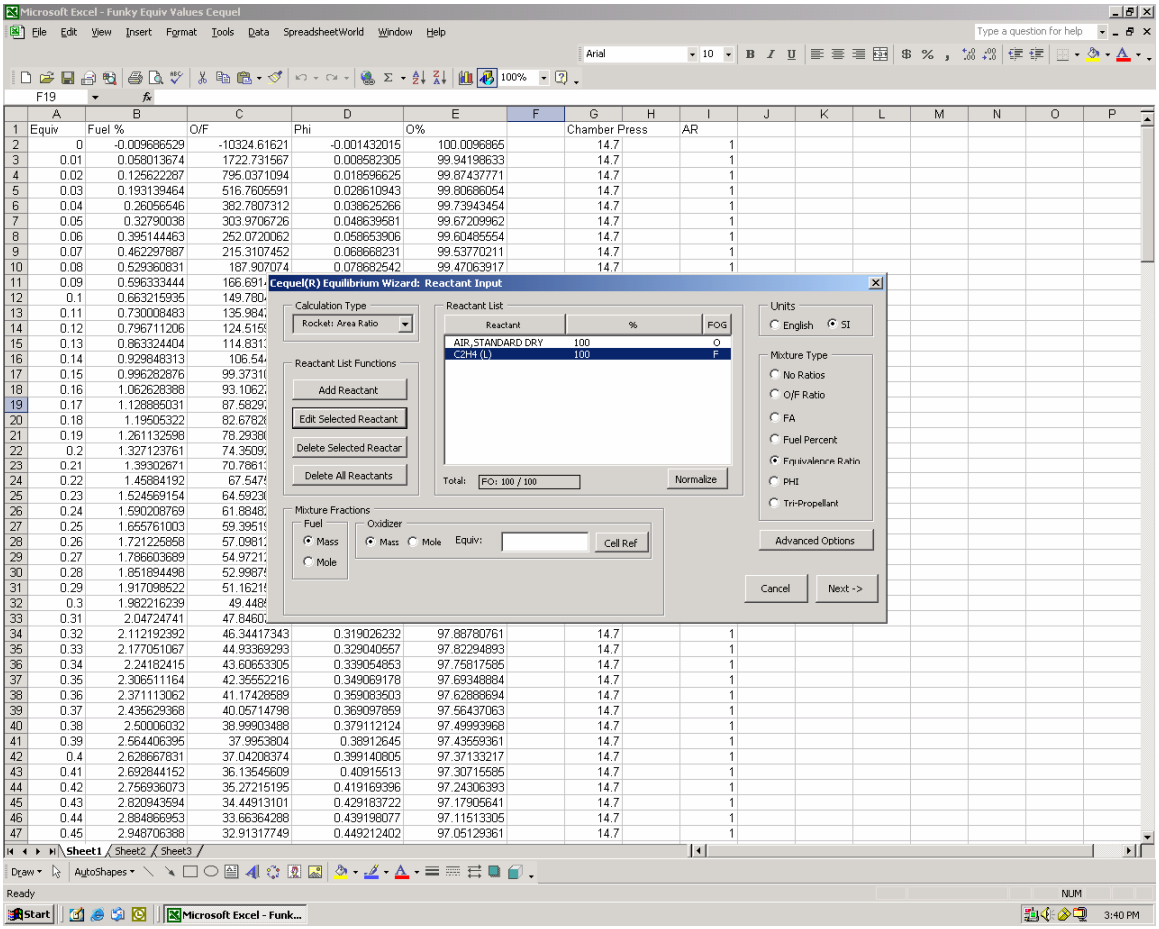

Figure 50. Cequel Screenshot.

The mass flow rates of air and fuel delivered to the test section were determined by the required equivalence ratio (φ). The equivalence ratio compares the fuel/oxidizer ratio of a given mixture to the ideal stoichiometric ratio of the mixture, and is defined by Equation (12):

Equivalence Ratio:
$$\phi = \frac{\dot{m}_f / \dot{m}_o}{\left[\dot{m}_f / \dot{m}_o\right]_{stoichiometric}} \quad (12)$$

The stoichiometric ratio refers to the idealized chemical reaction for complete combustion of all reactants into final products. The stoichiometric chemical equation for a mixture of ethylene (C_2H_4) and air (O_2+3.76N_2) is shown in Equation (13):

$$C_2H_4 + 3(O_2 + 3.76N_2) \rightarrow 2CO_2 + 2H_2O + 3(3.76N_2) \quad (13)$$

Equation 13 indicates φ equal to 1. When φ is less than 1, the reaction is fuel lean and unreacted oxygen is present in the combustion products. With φ greater than 1, the mixture is fuel rich and unreacted ethylene remains after combustion. Nitrogen is present on both sides of the equation as an unreactive component. The relationship represents an idealized case, indicating complete combustion that is unrealized in actual reactions where some degree of dissociation is always present. It also assumes ideal mixing resulting in a homogenous mixture, allowing all reactants to interact appropriately.

Cequel was used to determine the mass flow rates required to produce φ ranging from 0.1 to 2.42. These data were exported into a text file and used as a lookup table from LabVIEW. The required mass flow rates for each gas were then accessed for the desired equivalence ratio. The process allowed multiple test runs at different equivalence ratios without being forced to pause and recalculate mass flow rates.

A slightly fuel rich reaction was desired to assure a highly energetic, detonable mixture of gases. This also protected against the occurrence of locally fuel lean areas due to irregular mixing. After multiple tests to assure predictable ignition, an equivalence ratio of 1.2 was selected as the baseline for all further experimentation, resulting in a mass ratio of approximately 7.5% ethylene to 92.5% air.

2. LabVIEW

Experimental control was accomplished through a desktop PC executing LabVIEW Professional Development System 8.0, a Windows-based graphical user interface shown in Figure 51. A program file developed specifically for this project controlled actuators and received all data except high-speed imaging data from the

camera. It was designed to maximize flexibility and safety and integrated many options for step-by-step troubleshooting of the test cell. A detailed schematic of the LabVIEW back panel is included in Appendix C.

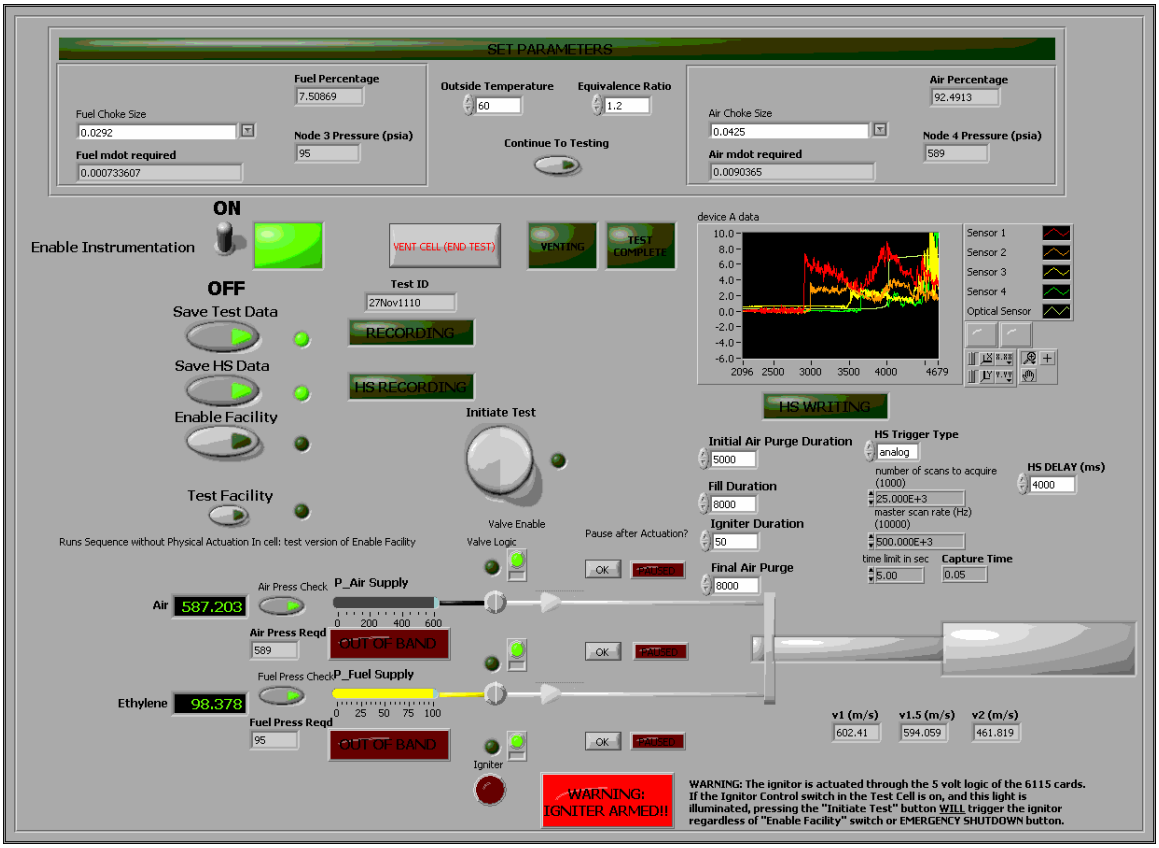

Figure 51. LabVIEW Front Panel Screenshot.

Upon program execution, LabVIEW reinitialized and established communication with the PXI cards and Crydom control solenoids in the test cell. The user was prompted to enter the respective choke sizes, desired equivalence ratio, and outside temperature. These data determined the percentage mass flow rates of each gas with respect to the total mass flow rate.

The total mass flow rate required was pre-determined to be 9.77 g/sec, based on the total amount of gas mixture estimated to completely fill the test section volume within three seconds. The individual mass flow rates required were then calculated in LabVIEW by taking the appropriate percentages of the total mass flow rate.

Mass flow metering was accomplished by regulating the pressure upstream of choked flow orifices in the test cell. The required pressure at each choke was determined based on the mass flow rate desired, area of the choke orifice, and temperature, using the compressible isentropic flow relationship below [17]:

$$\text{Choked Mass Flow Rate:} \qquad \dot{m} = \left(\frac{A_2 p_t}{\sqrt{T_t}} \right) \Gamma_2 \mathrm{K}_\Gamma \tag{14}$$

$$\text{where } \mathrm{K}_\Gamma = \sqrt{\left[\left(\frac{g_c}{R} \right) \left(\frac{2\gamma}{\gamma - 1} \right) \left(\frac{2}{\gamma + 1} \right)^{\frac{2}{\gamma - 1}} \left(\frac{\gamma - 1}{\gamma + 1} \right) \right]} \tag{15}$$

and $\mathrm{K}_\Gamma = 1$ (choked flow)

Calculated pressure values were displayed to the LabVIEW user for manual adjustment of the ER3000 regulator system. When pressure readings from the test cell matched calculated values, warning indicators in LabVIEW extinguished and a test could be initiated.

While in standby mode, pressure readings from the choke pressure transducers were able to be displayed in LabVIEW. Upon commencement of a test run, LabVIEW obtained a time stamp that was used as the common reference between all data systems to correlate test runs. Pressure readings and test parameters were exported to a unique Excel file for later analysis. Upon completion of the run, high-speed data from the four Kistler pressure transducers and the optical sensors were acquired from the PXI card buffers and saved to unique Excel files as well as displayed in LabVIEW for immediate examination. Simultaneously, a subroutine in LabVIEW calculated estimated shock wave velocity from this data. Finally, selected data values were appended to an existing file that summarized the parameters and results of all tests conducted [18].

3. Ultra 17 Camera and Ultra

The Ultra 17 high-speed camera was controlled from a dedicated desktop computer executing Ultra (Version 1.1.19.1 prerelease). Ultra is a Windows-based program from DRS Data & Imaging Systems, Inc. for use with their Ultra-series high-speed cameras. This program allows the user to construct an imaging sequence and

transmit it to the camera. Ultra also arms the camera, which in these tests was remotely triggered by the optical sensor in the test cell, before acquiring and presenting captured image data.

An Ultra imaging sequence was composed of 17 frames with a selectable trigger delay of 3.4 microseconds to 100 milliseconds. It was capable of a frame rate ranging from 1000-150000 frames per second with an exposure time of 10 nanoseconds to 1000 milliseconds. Gain was typically set the maximum value of 100. Many different sequence templates were created and used during testing to capture different time intervals, but a typical sequence using a 360 microsecond delay, 50000 frames per second, and 10 microsecond exposure time is illustrated in Figure 52 [19].

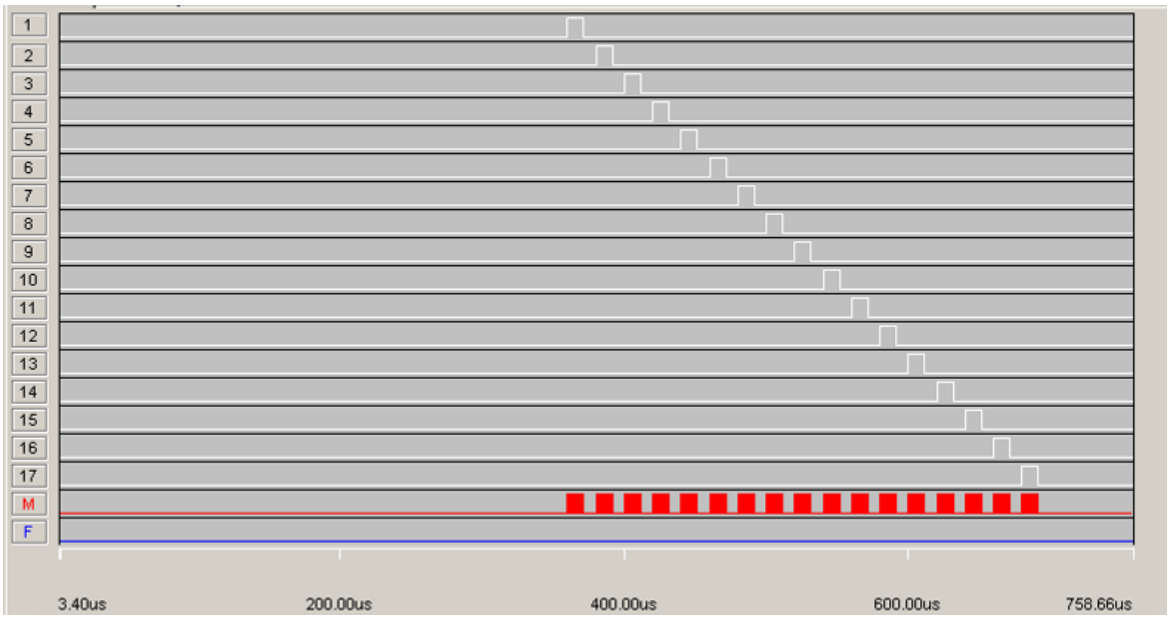

Figure 52. Typical Ultra Imaging Sequence.

4. RDT+ Camera and MiDAS

The RDT+ high-speed digital camera was controlled from a dedicated laptop computer executing MiDAS (Version 2.1.8.1). MiDAS is a Windows-based program from Xcitex, Inc. licensed for use with the RDT-series cameras. When connected to the RDT+, this program was capable of displaying continuous live images from the camera. Trigger conditions and sequence parameters were controlled by the program and exported to a secondary control interface. When triggered, the buffer retained a preset number of images for analysis. The resolution of the RDT+ camera was 512 x 512 at 5,000 frames

per second. Resolution had to be reduced if the frame rate was increased. Due to these limitations, the frame rate was optimized to 512 x 72 resolution. This arrangement imaged the first 96% of the optical window, while allowing 30,000 frames per second with 10 microsecond exposures. Once tested and calibrated, this setting was used for all the remaining imaging [20].

F. EXPERIMENTAL TEST PROCEDURE

The Test Cell #1 Standard Operating Procedure in Appendix D contains the detailed steps in testing procedure, but this section provides a more descriptive summary.

1. Obstacle Set-Up

The obstacle dimensions were based on the dimensions used in the simulations. Limitations in manufacturing required an approximate twofold increase in obstacle scale and conversion to English units, as shown in Figure 53.

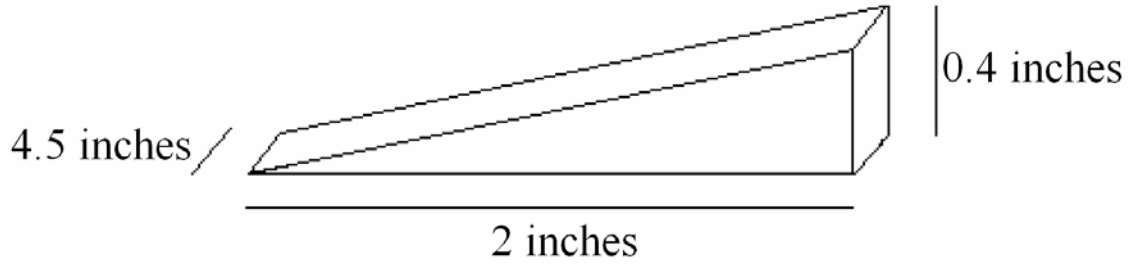

Figure 53. Straight Ramp Obstacle Dimensions.

A different obstacle arrangement was mounted in the test section for each series of testing. The setup ranged from a clean configuration (no obstacles) to up to four straight ramps mounted upstream of the optical test window (Figures 54 and 55). The obstacles spanned the test section and simulated two-dimensional flow,

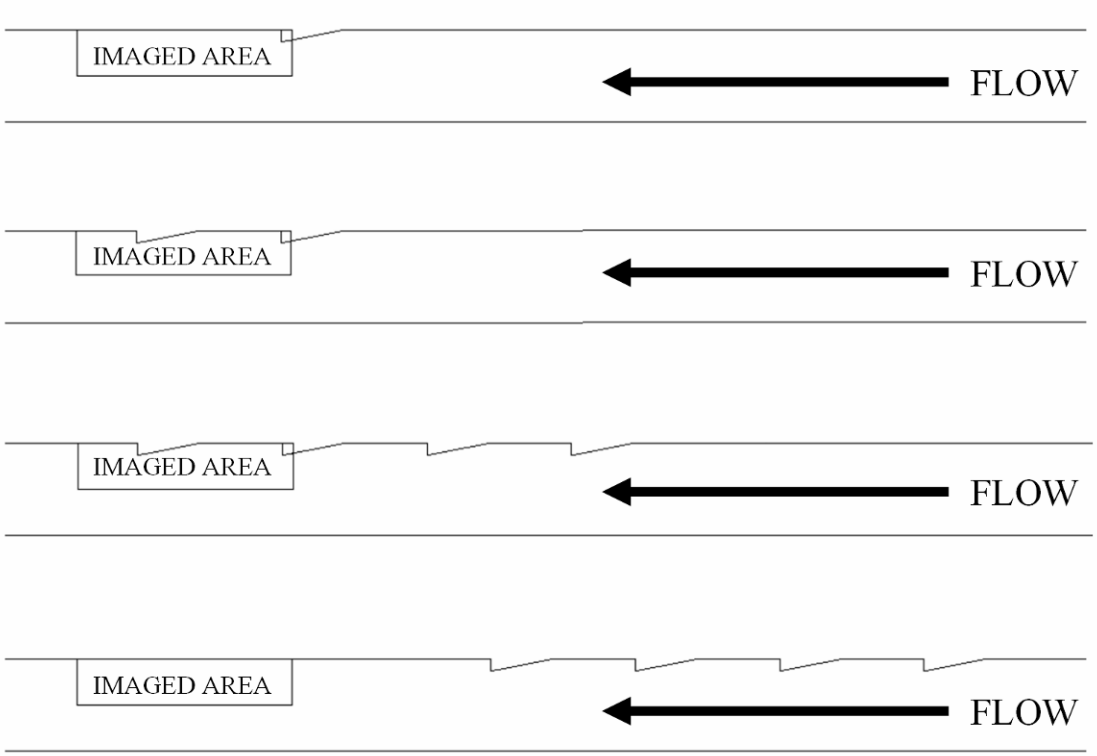

Figure 54. Obstacle Test Configurations.

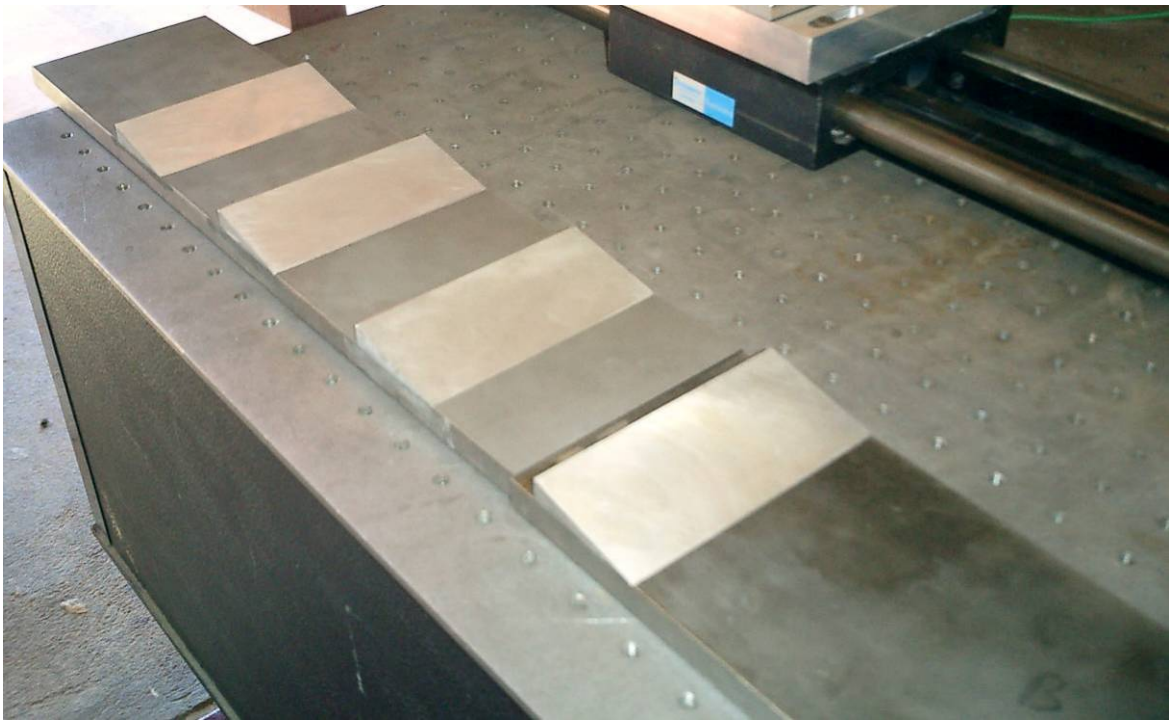

Figure 55. Sample Obstacle Configuration before Placement in Test Section.

2. Test Cell Initialization

The test cell configuration was kept the same for each run. Setup included closing and bolting the test section together, and attaching the external tube which was removed each day to allow the test cell door to close. Instrumentation lines were reattached, and all test cell electronics were powered up and gains on the amplifiers verified. The camera alignment was checked, and all gas supply valves were opened.

3. Mass Flow Calculation

LabVIEW, the ambient temperature, and desired equivalence ratio were used to calculate the required pressures upstream of the choked orifices. These pressures determined the mass flow rates required for each run. Calculated pressure values were entered into the ER3000, which regulated the supply pressures. Because of the higher accuracy of the test cell pressure transducers, the ER3000 input pressures often were in slight disagreement with the higher accuracy transducers installed near the chokes. The inputs to the ER3000 had to be changed in an iterative fashion until the pressures read by LabVIEW matched the desired pressures.

4. Test Setup

Just prior to execution, the camera system was armed to await the trigger signal to begin imaging. After several steps to ensure the safety of all personnel in and around the RPL, the cell was enabled. This step provided power to the cell and allowed test cell control by the LabVIEW virtual instrument (VI).

5. Test Execution

The program would begin a predefined sequence on command from the LabVIEW operator, to complete the test run. LabVIEW would first obtain a timestamp (e.g., “04DEC1410”) that would be used to identify the test run and all recorded data files for later correlation. The air ball valve would then open and begin a five-second initial purge to clear the test section. The ethylene ball valve would then open and the air/fuel mixture would begin to fill the test section. The system was designed for a three-second fill time, but the combustor was overfilled for a total of eight seconds. This longer time allowed the supply regulator to recover from the initial pressure drop and damp out transients in delivered flow. It also ensured that the entire test section was filled with

mixture of the desired equivalence ratio before ignition. Following the eight–second fill, the air valve would remain open while the fuel ball valve closed.

6. Combustion Event

Immediately after the fuel valve closed, the ignition system triggered and the event begun. The ignition signal also triggered the high speed acquisition of the Kistler pressure transducers. The initial combustion shock wave would quickly form and pass through the test section. The shock wave was characterized by a near-instantaneous and sustained pressure increase. Kistler transducers spaced at a defined distance from each other would register this event at slightly different times, and this data could be used to determine shock speed. The combustion event would follow approximately 2 milliseconds later, and excite the optical sensor just prior to entering the optical test section. The optical sensor triggered the camera which would image the flame as it passed the optical windows. After the flame had passed and as the shock wave was leaving the end of the tube, a rarefaction wave would form and propagate through the test cell, but in the opposite direction.

7. Data Collection

While the event was taking place the air valve remained open for a total of eight seconds, ensuring that the combusted products were evacuated from the test section. During this time, the high speed data acquisition cards would transmit all buffered data to LabVIEW for storage and examination. All camera images were also stored on their respective computers. Saved data included high-speed pressure and optical readings, low speed readings of the choke pressures, image data, and a test summary of all parameters of the test.

8. Test Completion

The air ball valve then closed and the test was complete. The cell was disabled, safety warnings removed, and the ER3000 pressures were set to zero. The test cell could then be configured for a subsequent run. The entire test sequence took place in less than 22 seconds, with the combustion event complete in approximately 10 milliseconds from start to finish.

V. EXPERIMENTAL RESULTS

A compendium of all tests with valid data collection is included in Appendix E. A total of 117 data collection tests were conducted, for five different configurations. A summary of results for representative obstacle configurations are included in this section. These include comparisons of pressure data obtained, flame speed measurements, and numerical results.

A. HIGH-SPEED PRESSURE DATA

This section will illustrate pressure trace data from the different obstacle configurations tested. It is primarily a qualitative comparison analysis, and quantitative data follows in a later section.

The P1 and P2 traces represent the responses of the high speed pressure transducers located in the transition section before the optical test section. The optical transducer was used as a trigger and is physically located between the first two transducers, and the magnitude of the measurements were not quantitative but were temporally accurate. P3 and P4 are the pressure transducers after the test section in the external tube. Data collection began at time zero and ended 20 milliseconds later, but all traces have been expanded to the area of interest.

Pressure readings were primarily used to measure shock speeds, and initially used only qualitatively to compare pressure increases experienced. As pressures increased dramatically near the end of testing, this data exceeded the threshold of the amplifiers and was clipped due to the dynamic range settings. Gains of the amplifiers were reduced for later runs, and all traces are normalized accordingly. Unfortunately, some data was lost before quantitative analysis of pressure data was considered.

A detailed description follows for the results of the clean configuration, followed by highlighted differences for subsequent configurations.

1. Clean Configuration

Several tests were conducted to validate data collection and characterize the baseline response of the test section with no obstacles present. High speed pressure data with the optical sensor response superimposed for the clean tube configuration are shown in Figure 56.

The initial pressure spikes registered in P1 and P2 as the initial shock wave reached the first set of transducers near 0.006 seconds. The shock can be seen passing the P3 and P4 transducers near 0.0074 seconds. This shock was created by the initial combustion event and was very far ahead of the actual combustion wave, on the order of 2 milliseconds. This corresponds to a distance of approximately 1.2 meters.

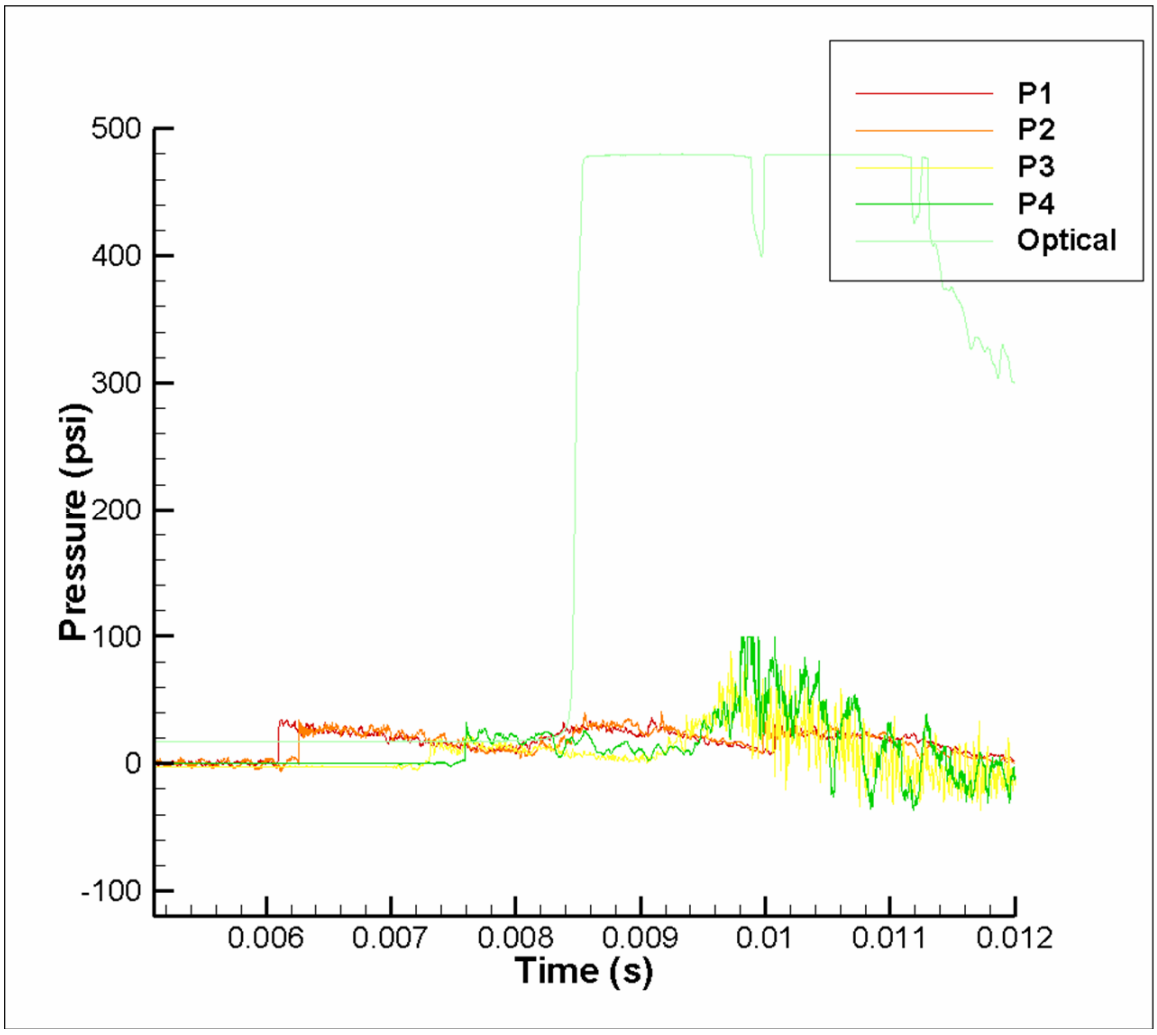

Figure 56. Pressure Traces for Clean Configuration.

The combustion event reached the optical sensor located between the P1 and P2 near 0.008 seconds. This signal was not precise as the sensor may begin to sense illumination reflected off the combustor walls from the combustion event before it passes. The response of this trigger was also filtered by the pre-amplifier above 100,000 Hz and has a proportionally delayed response. Despite these issues, the signal shown on this graph is a qualitatively valid comparison between the test runs.

The optical signal is accompanied shortly after by a slight increase in pressure in P1 and P2 caused by passage of the flame front, around 0.0088 seconds. For the clean configuration, these pressures never exceed the initial pressure rise experienced from the combustion shock. The response is magnified by the time it reaches the P3 and P4 transducers near time 0.01 seconds as shock waves in the test section begin to coalesce.

2. One Ramp

The addition of one ramp obstacle (Figures 57 and 58) did not drastically affect the results for the clean tube configuration. The characteristics of the initial shock are similar, and are comparable for all configurations tested. This will show that the addition of obstacles did not greatly affect the speed of propagation of the initial shock wave, nor were they expected too.

Figure 57. One-Ramp Configuration.

There was a slight increase in pressure experienced by the P1 and P2 transducers near flame front passage, actually exceeding the initial pressure rise. The P3 and P4 traces are correspondingly larger, actually exceeding the gain threshold as discussed above. While not definitive, this second pressure rise occurs earlier after the optical detection than in the clean tube, indicating a possible increase in flame speed.

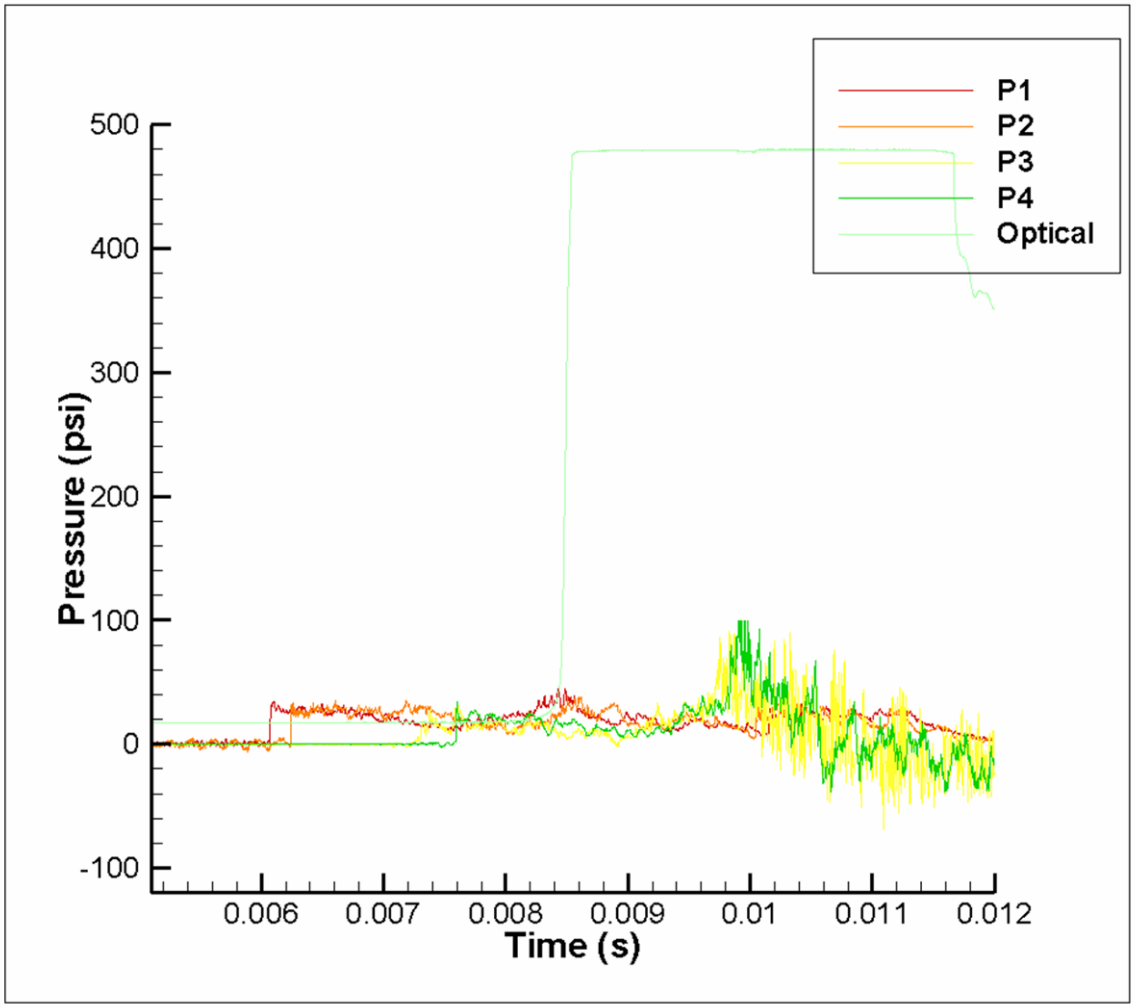

Figure 58. Pressure Traces for One-Ramp Configuration.

3. Two Ramps

The time difference between initial shock passage and flame front passage is noticeably shorter with two ramps (Figures 59 and 60). The second shock also occurs earlier after flame passage and the observed pressure increases are greater. Amplifier saturation becomes more noticeable here, and the gain was reduced for later runs.

While the pressure traces for two ramps showed increased pressure and flame speed, the results from the images were inconclusive. The time remaining for experimental testing was becoming short, and testing was accelerated to the four-ramp configuration.

Figure 59. Two-Ramp Configuration.

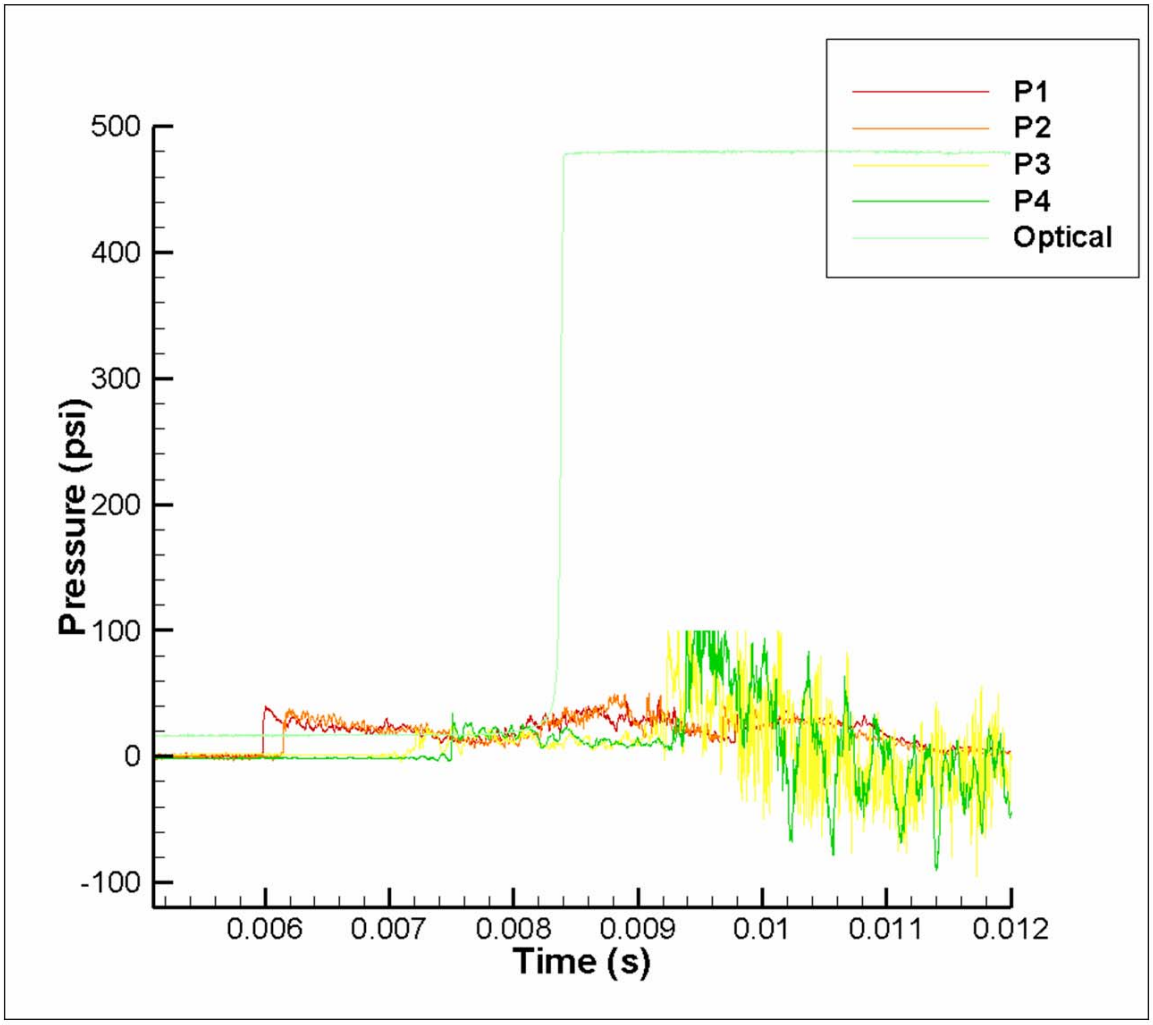

Figure 60. Pressure Traces for Two-Ramp Configuration.

4. Four Ramps Mounted Aft

Pressure traces from the four ramps mounted aft in the test section showed pressure rises with flame passage and large increases in the last transducers (Figures 61 and 62. Because of gain discrepancies, these latter pressure data were inconclusive when compared with the two-ramp configuration. Imagery was difficult to analyze, and for the

final set of experimental tests the four-ramp configuration was moved upstream 6 inches to allow the flame front to redevelop after obstacle passage.

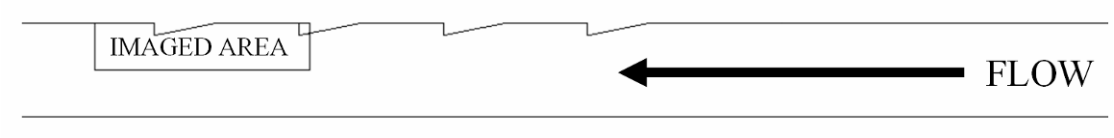

Figure 61. Four-Ramp Configuration Mounted Aft.

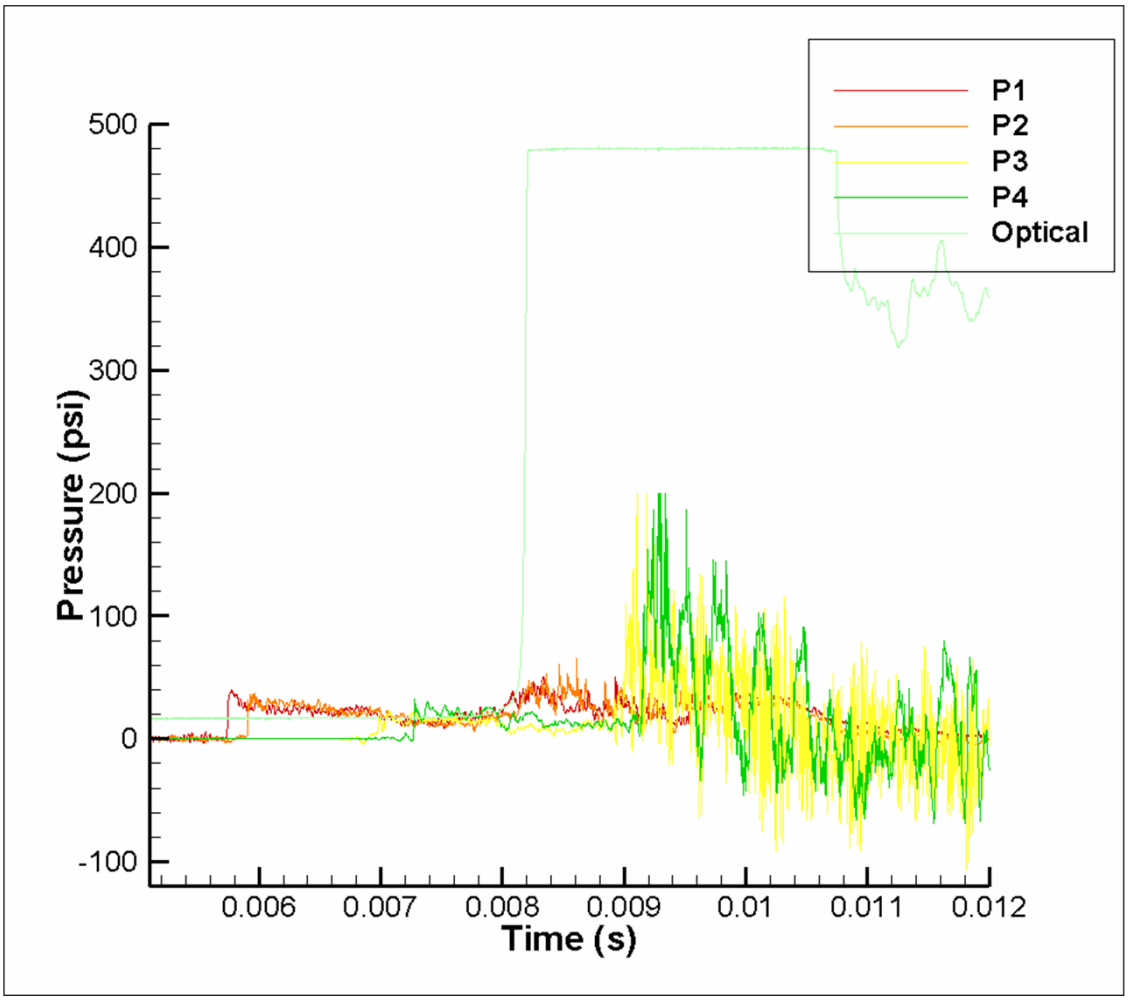

Figure 62. Pressure Traces for Four-Ramp Configuration Mounted Aft.

5. Four Ramps Mounted Forward

The most significant data were collected when the four ramps were mounted in the forward portion of the test section (Figures 63 and 64). When the ramps were moved forward, the initial shock remained consistent with previous tests Flame front passage occurred very shortly after the shock passed P4, indicating that the flame is moving much faster than in these other tests. A significant increase in pressure rise at flame passage is also present, reaching P3 and P4 very quickly and reaching pressure levels not seen in any other test.

Figure 63. Four-Ramp Configuration Mounted Forward.

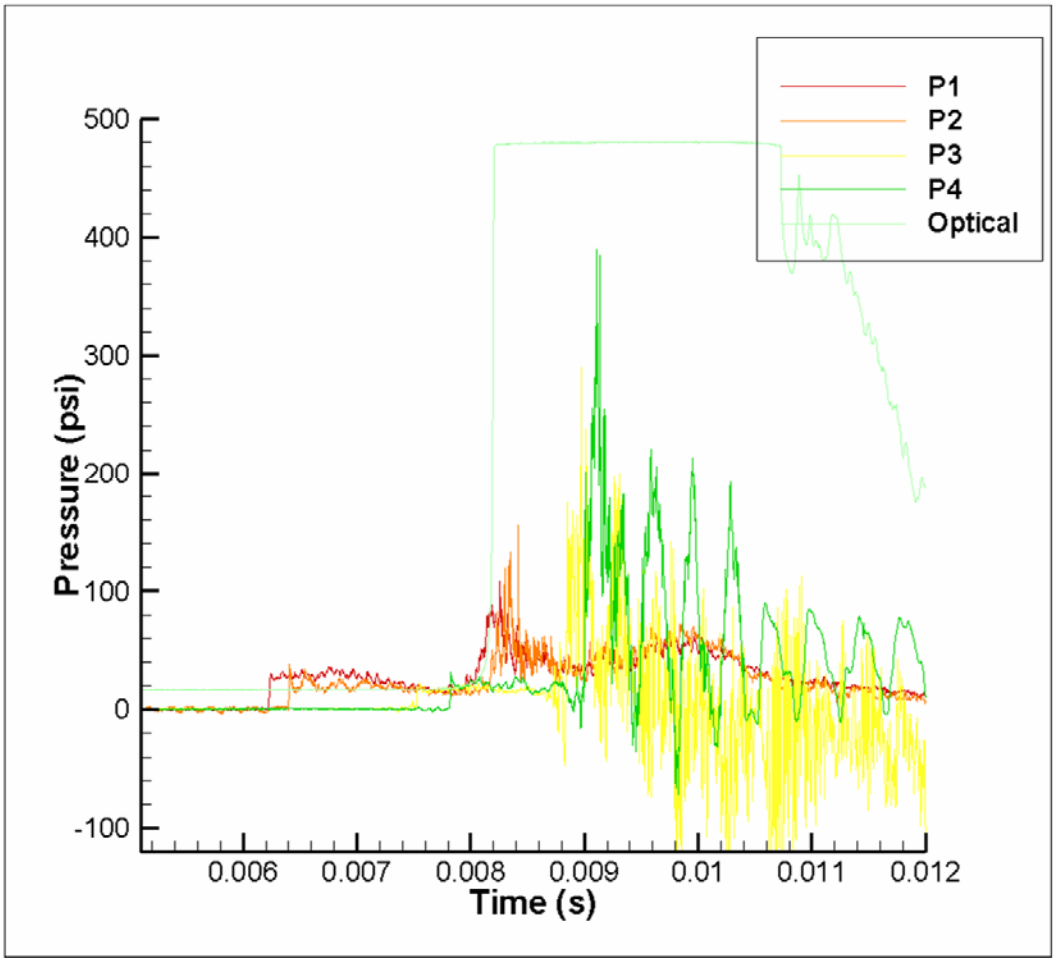

Figure 64. Pressure Traces for Four-Ramp Configuration Mounted Forward.

While compelling, this test could not be duplicated with full instrumentation. Following this run, the P4 pressure transducer stopped sending useful information. Subsequent runs did show that the other results were reproducible, as seen in Figure 65. Large pressure rises following flame front passage are visible, and pressure rises in P3 are even larger than those seen in the previous run.

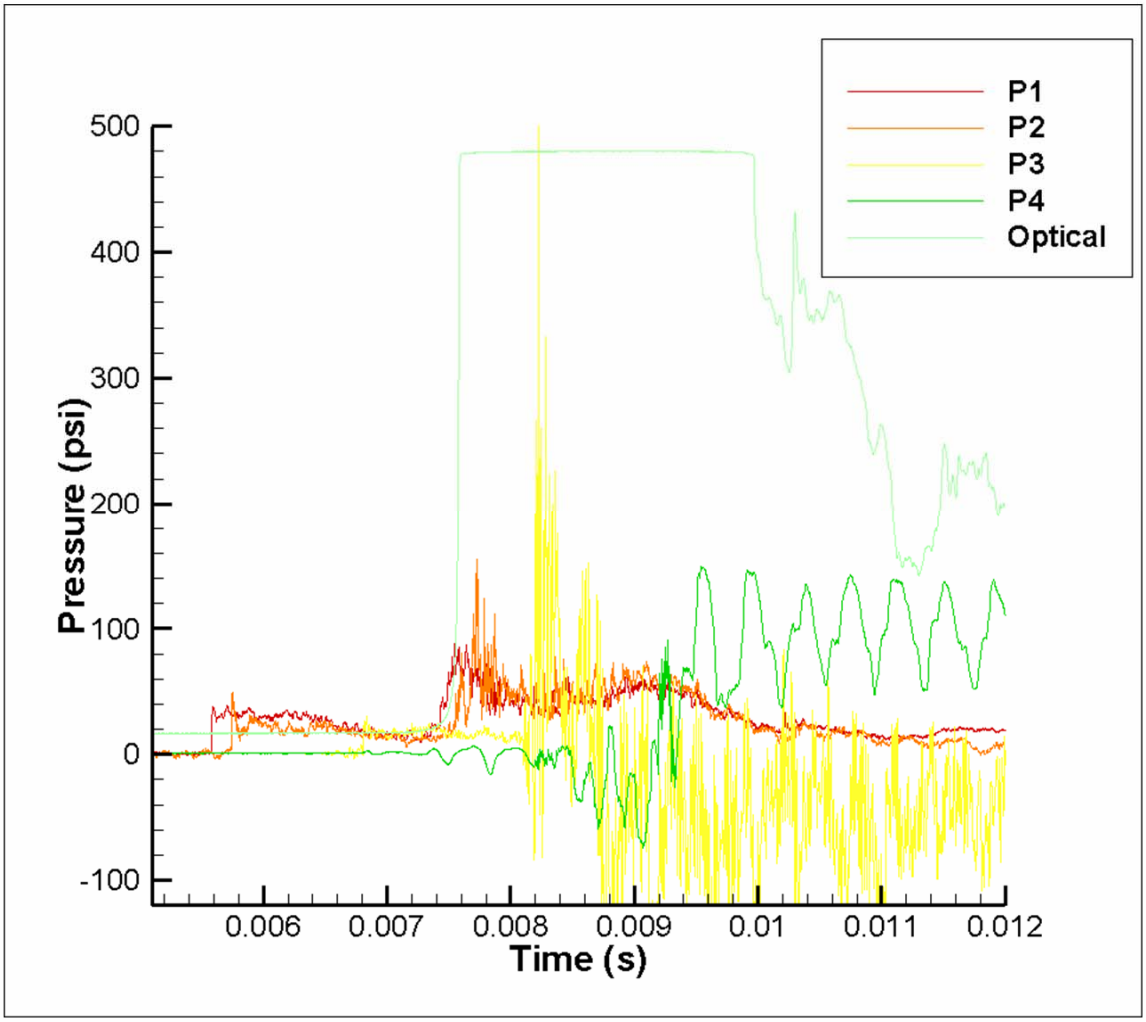

Figure 65. Pressure Traces for Four-Ramp Configuration Mounted Forward: P4 Sensor Inoperable.

6. Summary

The pressure traces clearly show a large increase in pressure corresponding to flame front passage with the addition of obstacles. This indicated the presence of multiple strong compression waves beginning to coalesce ahead of the flame. The traces also indicated possible acceleration of the combustion event. While not conclusive, these data demonstrated reproducible effects corresponding to flame acceleration with the addition of obstacles. The clean tube trace and final fully–instrumented trace are presented together for a final comparison in Figures 66 and 67.

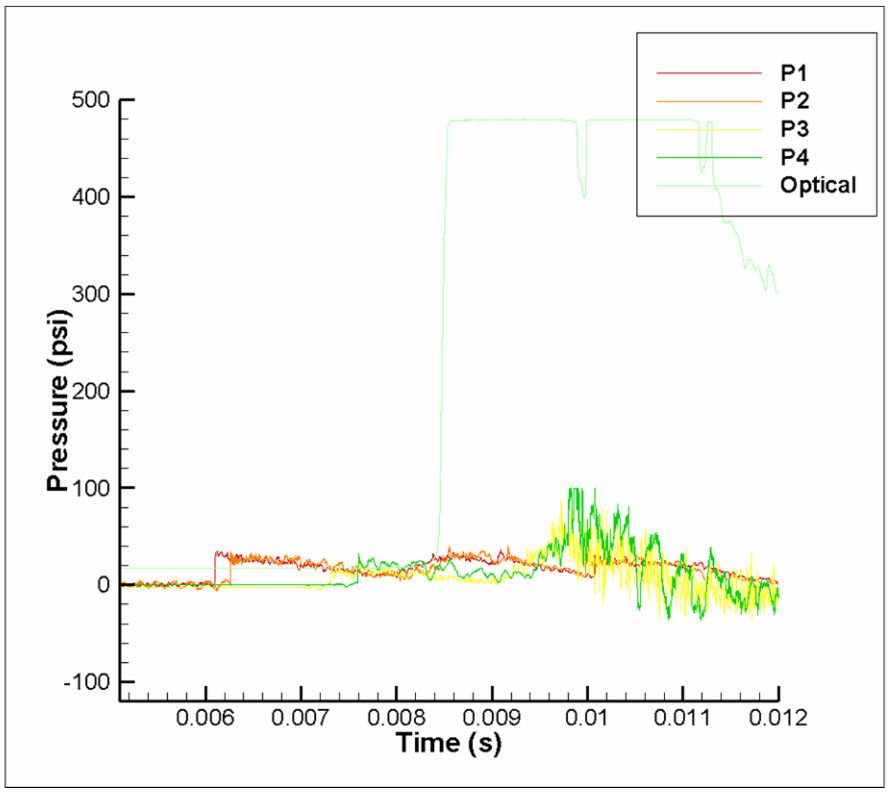

Figure 66. Clean Configuration Comparison.

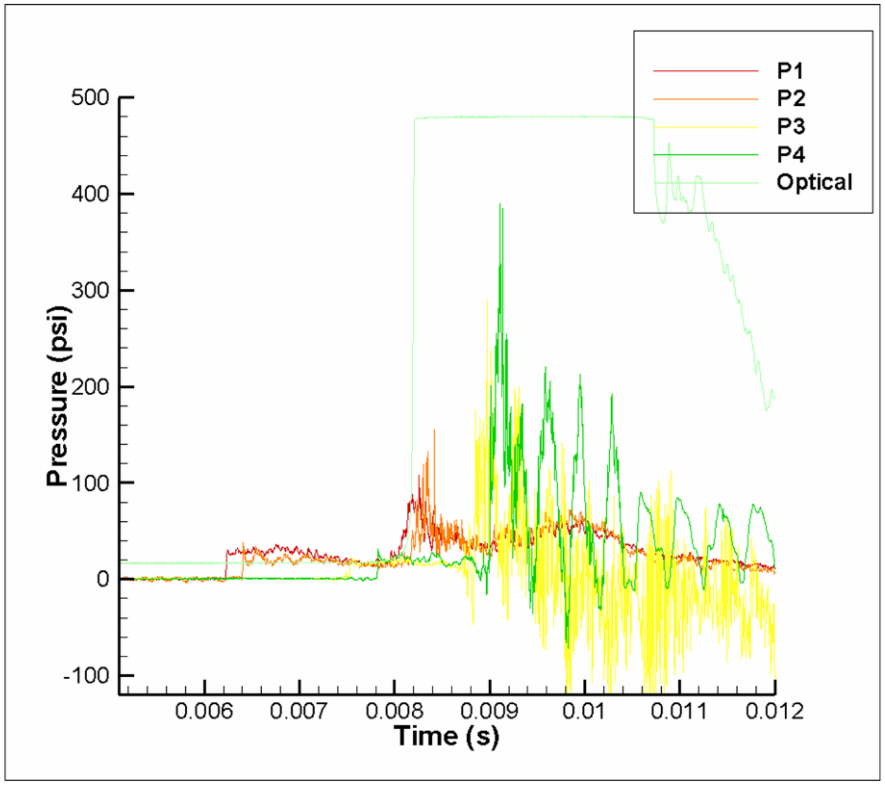

Figure 67. Four-Ramp Configuration Mounted Forward Comparison.

B. HIGH-SPEED CAMERA IMAGES

Two different camera configurations were used in the experimental test runs. The Ultra with image intensification was used only during clean tube testing and the RDT+ was used for the remainder. The most important impact of this change was the inability of the RDT+ to see dim events. The RDT+ performance improved as more obstacles were added, an indication of increasing energy release creating higher levels of luminosity.

The high-speed imagery obtained supplied two types of data. Raw images showed qualitative understanding of the effects of the obstacles on the flame front. Frame-by-frame analysis allowed measurements of flame speed through the optical test section.

1. Flame Imagery

The image sequence in Figure 68 was taken using the Ultra camera, and shows flame passage through the unobstructed tube. Because of the geometry of the optical test

section, the lower half of the test section is obstructed. This image shows a parabolic flame front maintaining shape as it passes through optical test section. While these images were magnified by the Ultra camera, subsequent testing with the RDT+ did not provide enough illumination for analysis of images until more obstacles were included.

The image sequence in Figure 69 was one of the first useful images from the RDT+ camera, which did not depict good imagery until flame luminosity had been increased through the addition of more than one obstacle. This sequence shows flame passage in a two-ramp configuration. The black line is a wire from the pressure transducer that was displaced during a previous test. The flame front no longer represents a smooth or predictable shape, and seems to appear spontaneously on the far side of the final ramp. This is due to flame front advancement in the hidden portion of the test section. There is evident turbulence and possible vorticity on the backside of the ramp, but whether a streamwise component exists is difficult to determine. The flame appears to move very quickly but with no predictable shape of flame these images were not useful in measuring flame speed.

Figure 68. Clean Tube Ultra Sequence 01Nov1459, 50 microsecond Steps (Flow R-L).

Figure 69. Two-Ramp RDT+ Sequence 27Nov1708, 33 microsecond Steps (Flow R-L).

The image sequence in Figure 70 is of the four-ramp aft configuration using the RDT+ camera. While it is difficult to visualize from still images, MiDAS image processing shows a much more dynamic evolution of the event. In frames 3, 6, and 8, large increases in luminosity are clearly seen. The flame front in this configuration appears to deflect around the obstacles, only to rapidly collapse up against the top of the test section. This creates momentarily large flame surface area and corresponding increase in energy release. The burst drives the flame over the next obstacle and the sequence repeats itself. However, this obstacle field does not allow an accurate determination of flame speed.

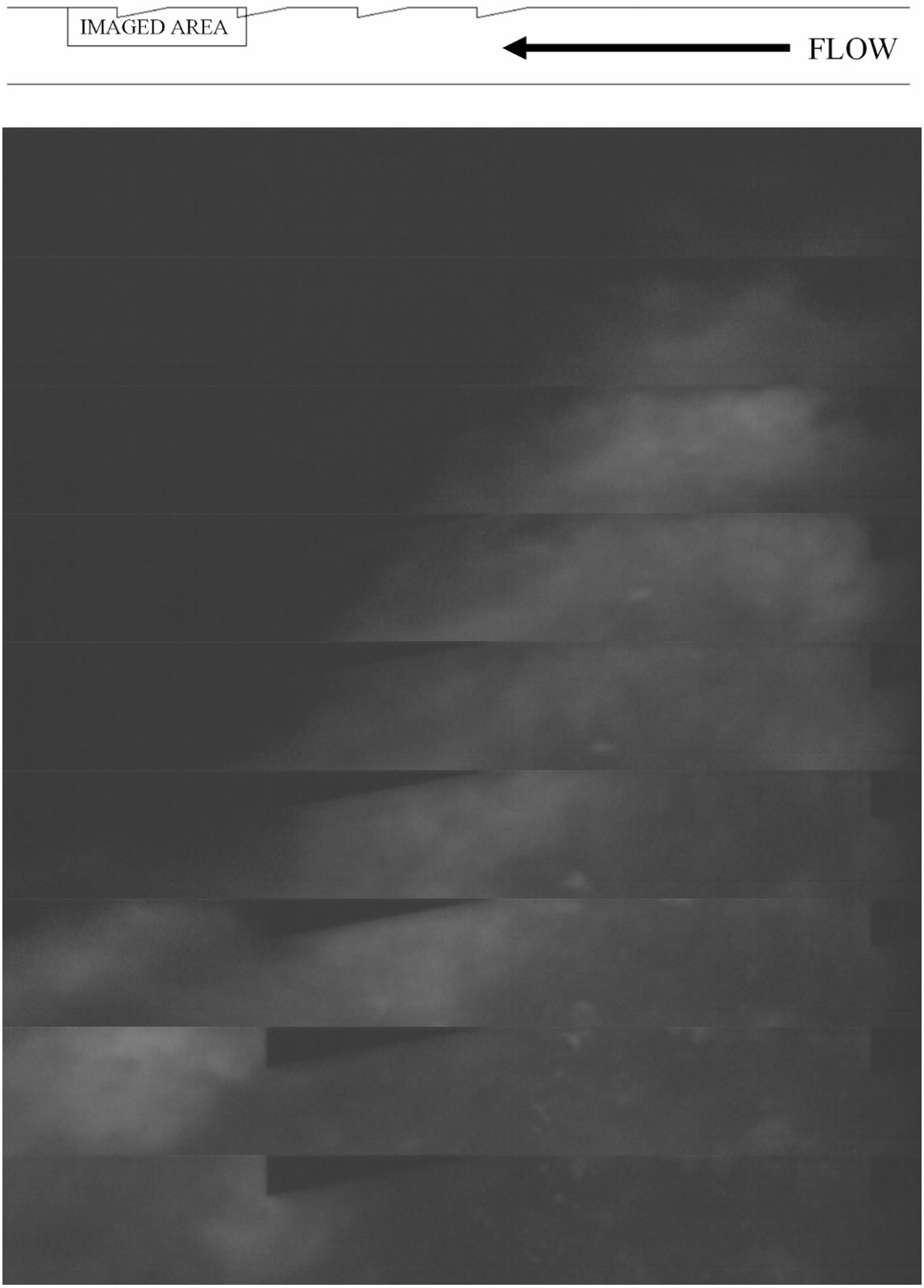

Figure 70. Four-Ramp Aft RDT+ Sequence 30Nov1234, 33 microsecond Steps (Flow R-L).

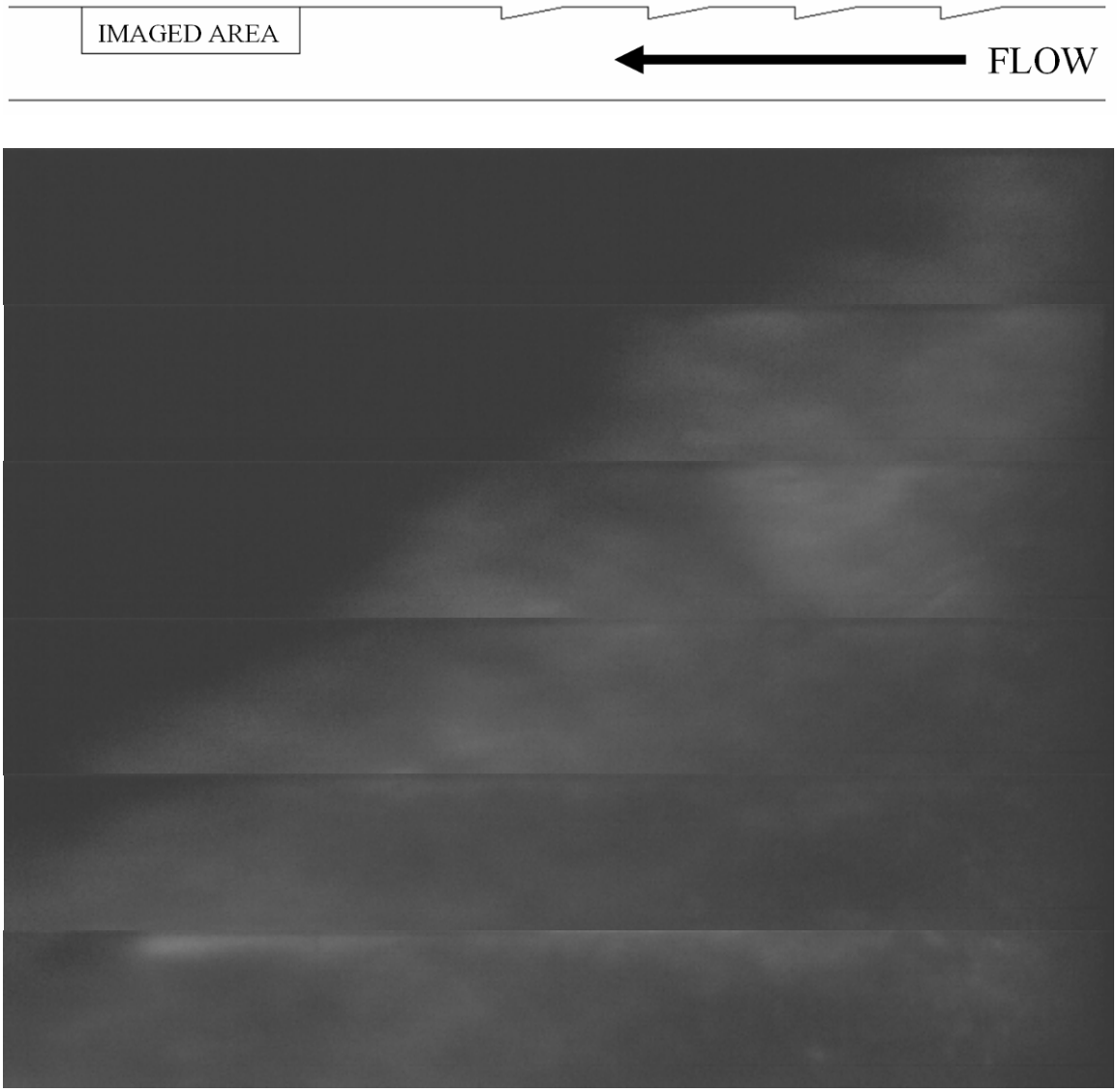

Figure 71. Four-Ramp Forward RDT+ Sequence 01Dec1621, 33 microsecond Steps (Flow R-L).

The final sequence in Figure 71 shows one of the most energetic of the four-ramp forward test runs. The flame has stabilized significantly compared to the configurations in which the obstacles reside in the imaging area, although some tumbling of the flame is present. These runs provided a much improved measurement of flame velocity, consistent across tests, and were much higher than any of the other configurations.

2. Flame Front Velocity Determination

Only the clean tube and four-ramp forward test configurations allowed accurate measurement of flame velocity. Flame speeds for the other obstacle fields were calculated, but required very subjective analysis.

Images were calibrated by imaging a micrometer in the optical window and determining the equivalent number of pixels spanned. Time information was taken directly from the image recorder, and together flame velocity was determined. Some subjective interpretation was required to determine the exact location of the flame front in any given image. To compensate, identical criteria were used between different runs to identify the flame front. Inter-frame velocities and total velocity across the optical window were calculated and compared to provide the most accurate assessment of actual flame velocity.

C. DATA ANALYSIS

The following section summarizes the quantitative results of the experiment, based on the averages of all measurements and observations for each ramp configuration. All test runs with good high-speed data collection were considered, although the sample size for flame velocity was somewhat smaller because not every run yielded usable imagery.

It should also be noted that the initial test run of each day was often audibly and visually weaker than subsequent runs with the same configuration. This was attributed to air present in the fuel lines from venting after the previous session, resulting in a lower than expected equivalence ratio and accompanied by much lower shock velocities than previously observed. These runs were not considered in this analysis.

1. Tabulated Data

All tabular information includes data from multiple runs, with two exceptions. The two-ramp configuration did not appear to produce pressure data significantly different from the one-ramp configuration, and imagery was inconclusive due to obscuration of the flame front. The testing schedule was accelerated to the four-ramp setup, and only later during analysis was it found that only one set of valid two-ramp data

had been obtained. Similarly, the four-ramp forward configuration only yielded one useable test run of data before failure of the P4 pressure transducer.

All tests were considered were conducted with a 1.2 equivalence ratio, except the final set of four-ramp forward runs, which were completed using a 1.3-1.35 equivalence ratio range. With the failure of P4 on the preceding runs, the goal of these final runs was to attempt to achieve detonation before the conclusion of experimental testing. While detonation appeared imminent, none was detected. Despite this, all collected data from these final runs correlated the trend of the previous equivalence ratio.

	V1 (m/s)	V1.5 (m/s)	V2 (m/s)	Post-Trig V (m/s)	Flame Velocity (m/s)
Clean	601	571	537	614	614
1 Ramp	605	573	525	571	565
2 Ramps	602	567	515	552	482
4 Ramps Aft	591	553	509	553	504
4 Ramps Fwd	575	535	515	1103	1136
4 Ramps Fwd*	615	559	--	1107	961

Table 4. Experimental Velocity Comparison.

V1 refers to the velocity of the initial combustion shock wave across the P1 and P2 high-speed pressure transducers, while V2 corresponds to the same shock across P3 and P4. V1.5 is the average velocity between P2 and P3 and was not as accurate as either V1 or V2, but sufficient to validate the other values.

Flame velocity was taken directly from camera observations. As discussed previously, only the clean and four-ramp forward configurations were considered sufficiently accurate although the other measurements are included in the table.

The post-trigger velocity was an extrapolated value obtained by measuring the time delay between the trigger event and the first image of flame in the window, across a known distance. The timing response of the optical sensor was not precisely characterized, containing inaccuracies due to possible early excitation from luminosity and reflections sensed before flame passage. A correction factor was employed to account for trigger delay. This correction assumed that the flame velocity observations in the clean configuration were relatively unchanging across the 13.8 cm distance between

the sensor and the optical window. The factor was scaled so that the post-trigger velocity was equal to the observed flame velocity in the clean configuration. While this was not a strictly qualitative analysis, it provided additional comparison data supporting the observed flame velocity.

2. Analysis

Three main observations emerged from these data. The first was that regardless of ramp configuration, the speed of the initial combustion shock wave was relatively consistent across both pairs of pressure transducers. While the clean and one-ramp configurations were both located after P1 and P2, the other configurations involved obstacles upstream of these sensors. V2 was proportionally decreased compared to V1 across all obstacle configurations, and may in part be attributable to obstacle interference. However, the comparable presence of this phenomenon in the clean configuration suggested that the deceleration was a characteristic of the test section. It may have been a result of the slight expansion from the optical test section into the larger external tube, where the P3 and P4 transducers are located.

The second notable detail was that the observed flame velocity data did not seem to indicate acceleration with the addition of obstacles, until a very large increase with the four-ramp forward configuration. This was attributed to the difficulty in measuring the position of the actual flame front when obstacles were present in the optical test section. This forced estimation of flame edges that may in fact have significantly lagged the actual flame front. Qualitative trend analysis of imagery data suggested that significant flame activity was present outside of the field of view and further supported this explanation for the apparent discrepancy. This also explained corresponding estimates of the post-trigger flame velocity, which was determined by the timing of the first flame visible in the imagery. Any delay in initial flame detection would indicate slower velocities than actually present.

Comparison of flame velocity in the clean and four-ramps forward configurations showed conclusive proof that the latter case produced significant acceleration of the flame front. Both of these cases provided clear imagery that depicted a continuous and consistent flame front. This was supported by the indications of post-trigger flame velocity.

THIS PAGE INTENTIONALLY LEFT BLANK

VI. CONCLUSIONS AND FUTURE WORK

A. CONCLUSIONS

This thesis explored the use of straight and swept ramp obstacles to enhance deflagration-to-detonation transition. While detonation was not achieved, experimental data have shown that straight ramp obstacles were effective in producing the conditions that lead to detonation. Large pressure increases in the secondary shock wave indicated the formation of strong shocks due to coalescence of strong compression waves, and observations clearly show flame front acceleration. Increased flame luminosity and flame front surface area indicated the potential for rapid energy release leading to flame acceleration.

Simulations indicate the effects of swept ramps on inducing vorticity to the post-shock flow field. While not tested experimentally, this geometry shows promise to provide an additional avenue for flame acceleration.

B. FUTURE WORK

The experimental results of this thesis demonstrate that further research in this area is merited.

Time and material constraints, combined with technical issues, did not allow for the full scope of research originally envisioned by the author. With the existing setup, further testing of multiple configurations would help to better characterize the observed events. Placement of obstacles beginning further forward in the test section would allow more accurate measurement of flame front speed. This could be accomplished though addition of a longer mounting plate, which would also enable use of more than four obstacles. Individual straight and swept ramp obstacles with unconstrained sides could be manufactured to examine the three-dimensional effects during and after flame passage. When combined, these two subjects could progress towards development of three-dimensional obstacle fields to examine the cumulative and reinforcing effects of straight and swept ramps on DDT.

With minor modification, the existing test setup could incorporate an optical imaging area that included the entire test cross-section in its field of view. This would allow more accurate flame speed measurement and improved characterization of the flame front interactions with obstacles. The end of the test section could also be extended with a constant cross-sectional area, to include placement of additional pressure transducers further downstream of the obstacle field. Other future areas of research include the addition of base flow to straight and swept ramp configurations, and multi-cycle implementation to gather empirical data on total pressure losses compared to other methods of detonation initiation.

APPENDIX A: STEADY STATE CFD PARAMETERS

CFD Steady State Problem Settings				
**** Values are case dependent**				
Problem Type				
Modules				
	Modules:	Compressible Flow (Flow)		
Model Options				
Global				
	Flow			
		Gas Model:	Ideal Gas	
		Viscous Model:	Inviscid (Euler)	
		Ideal Gas Properties:		
			Molecular Weight:	28.97 g/mol
			Gamma (C_p/C_v):	1.4
Volume Conditions				
VC Setting Mode				
	Properties:	Fluid		
Boundary Conditions				
Wall		BC Setting Mode:	General	
		Flow Heat Transfer:	Adiabatic	
		Flow Condition:	No-Penetration	
Interface		BC Setting Mode:	General	
Inlet		BC Setting Mode:	General	
		Flow BC Subtype:	Fixed Mass Flow Rate	
		Boundary Values		
		U:	**1	m/s
		V:	0	m/s
		W:	0	m/s
		Static Pressure (p):	0	N/m^2
		Static Temp (T):	**2	K
Outlet		BC Setting Mode:	General	
		Flow BC Subtype:	Fixed Pressure	
		Static Pressure (p):	0	N/m^2
Initial Conditions				
Flow		Initial Condition From:	Constant	
		Flow		
		U:	0	m/s
		V:	0	m/s
		W:	0	m/s
		Static Pressure (p):	0	N/m^2
		Static Temp (T):	0	K

Solver Control					
Control					
	Simulation:	Steady State			
		Max Number of Cycles:	100		
		Zonal Subcycles:	1		
		Convergence Crit.:	0.0001		
	Time Step:	Based on CFL Number			
		Initial CFL:			0.1
		Final CFL:			1
		Ramping Cycles:			100
Spatial		Flux Splitting:		Roe's FDS	
		Spatial Accuracy:		First Order	
		Entropy Fix			
		Linear Waves:			0.2
		Nonlinear Waves:			0.2
Solvers					
	Flow				
		Time Integration:		Implicit	
		Implicit Scheme:		Point Jacobi (Fully Implicit)	
		Subiterations:			20
		Tolerance:			0.0001
		Discretization:		Backward Euler	
Output					
Output					
	Solution Data (DTF):	Specified Interval			
		Cycles/Steps:	25		
			Same File		
	RSL, Force, etc:		Overwrite/Create		
				50 cycles/steps	
		Unique files	Overwrite		

Table 5. CFD-FASTRAN Problem Settings for Steady State Simulations.

CFD Steady State Case Summary

Straight Ramp: U=100 Injected=0		
	Inlet	
**1	100	
**2	300	

Straight Ramp: U=200 Injected=0		
	Inlet	
**1	100	
**2	300	

Swept Ramp: U=100 Injected=0		
	Inlet	
**1	100	
**2	300	

Swept Ramp: U=200 Injected=0		
	Inlet	
**1	200	
**2	300	

Swept Ramp: U=200 Injected=50				
	Inlet		Base of Ramp	
**1	200		**1	50
**2	300		**2	300

Swept Ramp: U=200 Injected=100				
	Inlet		Base of Ramp	
**1	200		**1	100
**2	300		**2	300

Swept Ramp: U=200 Injected=150				
	Inlet		Base of Ramp	
**1	200		**1	150
**2	300		**2	300

Table 6. CFD-FASTRAN Case Summary for Steady State Simulations.

THIS PAGE INTENTIONALLY LEFT BLANK

APPENDIX B: TIME ACCURATE CFD PARAMETERS

CFD Time Sensitive Problem Settings				
**** Values are case dependent**				
Problem Type				
Modules				
Modules:	Compressible Flow (Flow)			
Model Options				
Global				
Flow				
Flow				
Gas Model:	Ideal Gas			
Viscous Model:	Turbulent (Navier-Stokes)			
Ideal Gas Properties:				
Molecular Weight:	28.97	g/mol		
Gamma (C_p/C_v):	1.4			
Viscosity:	Constant (Dynamic)			
Mu:	1.7e-5	kg/m-s		
Conductivity:	Prandtl Number			
Pr:	0.7			
Turbulent Conductivity				
Pr_t:	0.9			
Turbulence Model:	K Epsilon (Wall Function)			
Volume Conditions				
VC Setting Mode				
Properties:	Fluid			
Boundary Conditions				
Wall	BC Setting Mode:	General		
	Flow Heat Transfer:	Adiabatic		
	Flow Condition:	No-Slip		
Interface	BC Setting Mode:	General		
Inlet	BC Setting Mode:	General		
	Flow BC Subtype:	Fixed Mass Flow Rate		
	Boundary Values			
	U:	*1	m/s	
	V:	0	m/s	
	W:	0	m/s	
	Static Pressure (p):	*2	N/m^2	
	Static Temp (T):	*3	K	
	Turb. Kin. Energy (k):	0	m^2/s^2	
	Dissipation Rate (e)	0	j/kg-s	
Outlet	BC Setting Mode:	General		
	Flow BC Subtype:	Extrapolated		

Initial Conditions						
Flow	Initial Condition From:		Constant			
	Flow					
		U:	*4	m/s		
		V:		0 m/s		
		W:		0 m/s		
		Static Pressure (p):	*5	N/m^2		
		Static Temp (T):	*6	K		
		Turb. Kin. Energy (k):		0 m^2/s^2		
		Dissipation Rate (e)		0 j/kg-s		
Solver Control						
Control						
	Simulation:	Time Accurate				
		Max Number of Cycles:	10000			
		Start Time:	0 s			
		Max Time:	0.0002 s			
	Time Step:	Based on CFL Number				
		Initial CFL:				0.1
		Final CFL:				1
		Ramping Cycles:				100
Spatial		Flux Splitting:			Roe's FDS	
		Spatial Accuracy:			First Order	
		Entropy Fix				
			Linear Waves:			0.2
			Nonlinear Waves:			0.2
Solvers						
	Flow					
		Time Integration:			Implicit	
		Implicit Scheme:			Point Jacobi (Fully Implicit)	
		Subiterations:				40
		Tolerance:				0.0001
		Discretization:			Backward Euler	
Output						
Output						
	Solution Data (DTF):	Specified Interval				
		Cycles/Steps:	200			
			Unique File(s)			
	RSL, Force, etc:	Overwrite/Create				
					50 cycles/steps	
		Unique files				
		Overwrite				

Table 7. CFD-FASTRAN Problem Settings for Time Accurate Simulations.

CFD Time Sensitive Case Summary

Straight Ramp: Mach 2, T=300K				
*1, *2, *3	N/A (No Inlet)		Driver	Volume
		*4	0	0
		*5	480530	101320
		*6	522.97	300

Straight Ramp: Mach 3, T=300K				
*1, *2, *3	N/A (No Inlet)		Driver	Volume
		*4	0	0
		*5	1060000	101320
		*6	804.21	300

Straight Ramp: Mach 2, T=500K				
*1, *2, *3	N/A (No Inlet)		Driver	Volume
		*4	0	0
		*5	532940	101320
		*6	876.13	500

Straight Ramp: Mach 3, T=500K				
*1, *2, *3	N/A (No Inlet)		Driver	Volume
		*4	0	0
		*5	1252600	101320
		*6	1314.8	500

Straight Ramp with Base Flow: Mach 2, T=500K, u=225 m/s				
Base of Ramp			Driver	Volume
*1	225	*4	0	0
*2	101320	*5	532940	101320
*3	500	*6	876.13	500

Straight Ramp with Troughs: Mach 2, T=500K				
*1, *2, *3	N/A (No Inlet)		Driver	Volume
		*4	0	0
		*5	532940	101320
		*6	876.13	500

Sweep Swept Ramp: Mach 2, T=500K				
*1, *2, *3	N/A (No Inlet)		Driver	Volume
		*4	0	0
		*5	532940	101320
		*6	876.13	500

High-Sweep Swept Ramp: Mach 2, T=500K				
*1, *2, *3	N/A (No Inlet)		Driver	Volume
		*4	0	90
		*5	532940	101320
		*6	876.13	500

High-Sweep Swept Ramp with Flow in Volume: Mach 2, T=500K, u=90 m/s				
	Inlet		Driver	Volume
*1	90	*4	90	90
*2	532940	*5	532940	101320
*3	876.13	*6	876.13	500

Table 8. CFD-FASTRAN Case Summary for Time Accurate Simulations.

APPENDIX C: LABVIEW BACK PANEL SCHEMATIC

Figure 72. LabVIEW Back Panel Schematic.

THIS PAGE INTENTIONALLY LEFT BLANK

APPENDIX D: TEST CELL #1 STANDARD OPERATING PROCEDURES

Standard Operating Procedures 9.6 01DEC06

Test Cell #1

Facility Open Procedure (Start of Day)

1. CELL #1 EMERGENCY SHUTDOWN Button (Control Room) – VERIFY IN
2. Test Cell Door – OPEN
3. Igniter Control (Test Cell) – VERIFY OFF (Red Button OUT)
4. PXI-1000B Rack (Test Cell) – VERIFY ON
5. Shop Air Valve (Test Cell Table) – VERIFY OPEN
6. Test Apparatus/Chokes/Electrical leads – VERIFY INTEGRITY

Testing Set-Up

7. Viewing Section – SEPARATE FROM FILL TUBE (4 Bolts)
   Note: Viewing section must be removed and translated aft in order to complete following two steps
8. Obstacle Testing – SETUP
9. External Tube (Square section after Viewing Section) – ATTACH
10. Viewing Section – SECURE TO FILL TUBE (4 Bolts)
11. Kistler Amplifier Power – ENSURE OFF
12. Kistler Leads (4) – ATTACH
13. Exhaust Tube (Large red tube) – ENSURE PROPER POSITION
14. 115VAC CONTROL/CELL#1 Switch (Control Room) – ON
15. 28VDC POWER SUPPLY/CELL#1 Switch (Control Room) – ON
16. LabVIEW file "Z:\Medina\Labview\Funky 9_6.vi" – OPEN AND RUN ON RPL05 DESKTOP
17. LabVIEW: Continue to Testing Switch - DEPRESS
18. LabVIEW ENABLE INSTRUMENTATION Button – ON
19. Pressure Transducer Readings – VERIFY
    WARNING: HP AIR LINE MAY HOLD SOME RESIDUAL PRESSURE.
20. Notify all personnel that gases and TESCOM will be enabled
21. Test Cell #2 Node 4 Air Isolation Valve (Test Cell #2) – ENSURE CLOSED
    WARNING: THIS VALVE MAY BE LEFT OPEN ONLY IF TEST CELL #2 IS CONFIGURED FOR AND IS ACTIVELY ENGAGED IN TESTING.
22. Test Cell #3 Node 4 Air Isolation Valve (Test Cell #2) – ENSURE CLOSED
23. TRANSDUCER AND TESCOM POWER Switch (Test Cell #2) - ON
24. Set ZERO pressures on ER3000
    a. Node 3 (Ethylene)
    b. Node 4 (HP Air 1/2")
25. MAIN HP Air Isolation Valve (Test Cell) – OPEN

26. Test Cell #1 Node 4 Air Isolation Valve (Test Cell) – OPEN
    WARNING: OPEN VALVE SLOWLY TO PREVENT RAPID PRESSURIZATION OF LINES.
27. Igniter Control light (Red LED next to upper left Black CRYDOM in PXI-1000B Rack) – VERIFY OUT
    CAUTION: IF LIGHT IS ON, MUST RERUN LABVIEW CODE TO CLEAR DIO.
28. Power Strip (above PXI-1000B Rack) – ON
29. Igniter Control (Test Cell) – ON (Red Button IN)
30. Igniter Control Startup Diagnostic – OBSERVE COMPLETION
31. Optical Transducer Gain Switch – ON
32. Kistler Amplifier Power Switches (4) (On back of devices) – ON
33. Select "Operate" on Kistler Amps, verify proper gains set, ensure no error lights.
34. Low Noise Preamp – ON

35. **********ULTRA CAMERA ONLY**********
    a. Ultra-17 Camera – ON
    b. Ultra – RUN ON OPTIPLEX DESKTOP
    c. Ultra: Load "CALTEST.ult" file and verify image
    d. Ultra: Load *.ult file for desired test
    ****

35. ##########RDT+ CAMERA ONLY############
    a. RDT+ – ENSURE CABLE DISCONNECTED
    b. MAGMA Control Box – ON
    c. MiDAS USB Dongle – INSERT
    d. Sharp Laptop – ON
    e. At Laptop Welcome Screen – ENTER
    f. RDT+ – CONNECT CABLE
    g. MiDAS – RUN ON SHARP LAPTOP
    h. RDT+ Image – VERIFY
    i. Frame Rate, Exposure Time, Image Area – SET
    ##########

36. Main HP Air Jamesbury Valve (Outside of Test Cell) – OPEN
37. Node 3 (Ethylene) Shop Air Valve (Above Bottle in Bottle Room) – VERIFY OPEN
38. Ethylene Bottle (Bottle Room) – OPEN
    a. Check Ethylene Bottle Pressure Gauge for sufficient pressure for testing

Pre-Testing

39. LabVIEW: Stop and run again if parameters are not correct
40. LabVIEW: Verify proper ambient temperature and choke size is set
41. LabVIEW: Enter desired equivalence ratio
42. LabVIEW: Continue to Testing Switch - DEPRESS
43. LabVIEW ENABLE INSTRUMENTATION Button – ON
44. LabVIEW: If recording data:
    a. SAVE TEST DATA Button – ON
45. LabVIEW: If recording HS data:
    a. SAVE HS DATA Button - ON
46. LabVIEW: Select "Valve Enable" switches for desired test (all three required for ignition)
47. Verify desired trigger type and valve durations
48. Set required pressures on ER3000
    a. Node 3 (Ethylene)
    b. Node 4 (HP Air 1/2")
49. LabVIEW: Verify pressures, Enable "Air Press Check" and "Fuel Press Check" switches
    Note: The test cell transducers are more accurate than the ER3000, so a bias may have to be added to the ER3000 inputs to produce the desired pressures.
50. Set ER3000 Node 3 (Ethylene) to zero, verify zero pressure in LabVIEW
51. FUNKY TC1 VHS Tape – INSERT INTO VCR
52. Switch Monitor to B (Test Cell #1)
53. Camera - ARM

Testing

54. Set ER3000 Node 3 (Ethylene) back to desired setpoint, verify pressure in LabVIEW
55. Clear Test Cells/Head Count
56. Flashing Yellow Lights - ON
57. Verify Golf Course is clear
58. VCR – RECORD
59. SIREN – ON
60. LabVIEW: ENABLE FACILITY Button - ON
61. CELL #1 EMERGENCY SHUTDOWN Button – TURN CLOCKWISE
62. LabVIEW: INITIATE TEST Button - DEPRESS

Test Complete (When ENABLE FACILITY Button dims)

63. LabVIEW: ENABLE FACILITY Button – VERIFY OFF
64. CELL #1 EMERGENCY SHUTDOWN Button – PUSH IN
65. SIREN – OFF
66. VCR – OFF

If further testing will be accomplished immediately, return to "Testing"

WARNING: DO NOT CLOSE LABVIEW EARLIER THAN SOP OR IGNITER MAY TRIGGER.

Post Testing

67. Set ER3000 Node 3 (Ethylene) to zero, verify zero pressure in LabVIEW
68. FUNKY TC1 VHS Tape – REMOVE FROM VCR
69. Flashing Yellow Lights - OFF
70. Notify Personnel that cell is secure
71. Save image sequence with Test ID Data from LabVIEW
72. If further testing will be accomplished with identical obstacle set-up, return to "Pre-Testing"
73. If further testing will be accomplished with different obstacle set-up, return to "Testing Set-Up"

Facility Close Procedure (End of Day)

THE FOLLOWING ITALICIZED STEPS MAY IMPACT OTHER TESTING PERSONNEL. DECONFLICT WITH TEST CELLS #2 AND #3 BEFORE TAKING THESE STEPS:

74. Set pressures on ER3000 to zero
    a. Node 3 (Ethylene)
    b. Node 4 (HP Air 1/2")
75. Notify Personnel that cell will be venting
76. Flashing Yellow Lights - ON
77. CELL #1 EMERGENCY SHUTDOWN Button – TURN CLOCKWISE
78. LabVIEW: END TEST Button – DEPRESS
79. Vent Test Cell Following LabVIEW Prompts
80. CELL #1 EMERGENCY SHUTDOWN Button – PUSH IN
81. Flashing Yellow Lights - OFF
82. Ethylene Bottle (Bottle Room) – CLOSE

83. **********ULTRA CAMERA ONLY**********
    a. Ultra-17 Camera – OFF
    b. Ultra – EXIT ON OPTIPLEX DESKTOP
    ****

84. ##########RDT+ CAMERA ONLY###########
    a. RDT+ – DISCONNECT CABLE
    b. MAGMA Control Box – OFF
    c. MiDAS – EXIT ON SHARP LAPTOP
    d. Sharp Laptop – SHUTDOWN
    e. MiDAS USB Dongle – REMOVE AND SECURE
    ##########

84. Low Noise Preamp – OFF
85. Igniter Control (Test Cell) – OFF (Red Button OUT)
86. Kistler Amplifier Power Switches (4) (On back of devices) – OFF
87. Optical Transducer Gain Switch – OFF
88. Power Strip (above PXI-1000B Rack) – OFF
89. Test Cell #1 Node 4 Air Isolation Valve (Test Cell) – CLOSE
90. Kistler Leads (4) – REMOVE, COVER, AND STOW
91. Viewing Section – SEPARATE FROM FILL TUBE (4 Bolts)
    Note: Viewing section must be removed and translated aft in order to complete following two steps
92. External Tube (Square section after window) – REMOVE AND STOW
93. Viewing Section – TRANSLATE FORWARD CLEAR OF DOOR
94. ***TRANSDUCER AND TESCOM POWER Switch (Test Cell #2) – OFF***
95. ***MAIN HP Air Isolation Valve (Test Cell) – CLOSE***
96. Test Cell Door Clearance – ENSURE
97. ***Test Cell Door – CLOSE***
    Note: Other personnel may need access to this cell to close out their SOPs
98. ***Compressor SOP Complete - VERIFY***
99. ***Main HP Air Jamesbury Valve (Outside of Test Cell) – CLOSE***
100. ***Bottle Room – SECURE***
101. LabVIEW – EXIT ON RPL05 DESKTOP
102. ***28VDC POWER SUPPLY/CELL#1 Switch (Control Room) – OFF***
103. ***115VAC CONTROL/CELL#1 Switch (Control Room) – OFF***

THIS PAGE INTENTIONALLY LEFT BLANK

APPENDIX E: TEST SUMMARY

Test ID	Ramp	Phi	Fuel %	Air %	P1 (ms)	P2 (ms)	P3 (ms)	P4 (ms)	V1 (m/s)	V1.5 (m/s)	V2 (m/s)	Image Qual	Post Trig V (m/s)	Flame V (m/s)
25 OCT 1451		1.1	6.9	93.1	9.576	9.734	16.596	11.014	633					
25 OCT 1517		1.1	6.9	93.1	9.576	9.734	16.596	11.014	633					
25 OCT 1522		1.1	6.9	93.1	10.330	10.494	0.000	11.796	633					
25 OCT 1523		1.1	6.9	93.1	10.140	10.302	11.316	11.574	610					
25 OCT 1533		1.1	6.9	93.1	9.968	10.122	11.114	11.390	617	592	591			
26 OCT 1200		1.1	6.9	93.1	8.842	8.998	10.002	10.250	649	605	552			649
26 OCT 1215		1.2	7.5	92.5	8.504	8.656	9.630	9.890	641	598	615			641
26 OCT 1224		1.3	8.1	91.9	8.550	8.700	9.660	9.912	658	616	586			658
26 OCT 1230		1.4	8.7	91.3	8.550	8.700	9.660	9.912	667	625	605			667
26 OCT 1232		1.4	8.7	91.3	8.476	8.626	9.672	9.838	667	625	605			
26 OCT 1302		1.4	8.7	91.3	5.620	5.786	7.134	7.130	667					
26 OCT 1440		1.4	8.7	91.3	5.952	7.126	6.112	7.410	602					
26 OCT 1606		1.4	8.7	91.3	6.604	6.762	7.790	8.070	625	592	537			
31 OCT 1456		1.4	8.7	91.3	5.142	6.208	7.234	7.508	633	584	544			
31 OCT 1510		1.4	8.7	91.3	5.116	6.200	7.268	7.554		585	556			
31 OCT 1519		1.4	8.7	91.3	6.038	6.200	7.506	7.510		562	533			
31 OCT 1538		1.4	8.7	91.3	6.420	6.590	7.918	7.930	617					
31 OCT 1544		1.2	7.5	92.5	6.420	6.590	7.918	7.930	588					
31 OCT 1607		1.2	7.5	92.5	6.878	7.042	8.174	8.362	588					
01 NOV 1348		1.2	7.5	92.5	6.556	6.724	8.076	8.068	610					
01 NOV 1352		1.2	7.5	92.5	6.894	7.066	9.976	8.432	595					
Ultra-17 Added to Test Cell														
01 NOV 1354		1.2	7.5	92.5	6.824	6.996	9.962	8.368	581			X		
01 NOV 1404		1.2	7.5	92.5	6.520	6.690	7.776	8.058	581			XX		536
01 NOV 1459		1.2	7.5	92.5	7.158	7.326	8.366	8.654	588	552	540	XX		526
02 NOV 1358		1.2	7.5	92.5	6.960	7.120	8.138	8.416	595	577	529	XX		470
02 NOV 1428		1.2	7.5	92.5	7.034	7.210	8.324	8.614	625	589	548	X		
02 NOV 1436		1.2	7.5	92.5	6.848	7.020	8.098	8.390	568	539	526			
02 NOV 1443		1.2	7.5	92.5	7.040	7.218	8.342	8.640	581	557	522			
02 NOV 1524		1.2	7.5	92.5	6.822	6.996	8.120	8.414	562	534	511			
02 NOV 1533		1.2	7.5	92.5	7.198	7.376	8.498	8.792	575	534	518			
02 NOV 1534		1.2	7.5	92.5	6.516	6.686	7.772	8.056	562	535	518			
02 NOV 1538		1.2	7.5	92.5	6.482	6.648	7.716	7.864	588	552	537	XXX		555
02 NOV 1548		1.2	7.5	92.5	6.440	6.606	7.658	7.944	602			X		
02 NOV 1554		1.2	7.5	92.5	6.482	6.618	7.676	7.836	602	570	533	XX		596
02 NOV 1555		1.2	7.5	92.5	6.744	9.220	11.102	10.616				X		
03 NOV 1437		1.2	7.5	92.5	6.616	9.264	7.846	10.312						
06 NOV 1244		1.2	7.5	92.5	6.490	6.658	7.714	8.002						
13 NOV 1549		1.2	7.5	92.5	6.922	7.096	8.170	8.466	595	568	529			
13 NOV 1553		1.2	7.5	92.5	6.722	6.892	7.942	8.232	575	559	515			

Test ID	Ramp	Phi	Fuel %	Air %	P1 (ms)	P2 (ms)	P3 (ms)	P4 (ms)	V1 (m/s)	V1.5 (m/s)	V2 (m/s)	Image Qual	Post Trig V (m/s)	Flame V (m/s)
13NOV1556		1.2	7.5	92.5	6.566	6.734	7.780	8.068	588	571	526	XXX		599
13NOV1601		1.2	7.5	92.5	6.656	6.822	7.856	8.140	595	574	529	XXX		621
13NOV1611		1.2	7.5	92.5	6.390	6.558	7.616	7.906	602	580	537	XXX		634
13NOV1617		1.2	7.5	92.5	6.394	6.562	7.620	7.908	595	567	526	XXX		641
13NOV1618		1.2	7.5	92.5	6.668	6.838	7.910	8.200	595	567	529	XXX		580
13NOV1619		1.2	7.5	92.5	6.588	6.764	7.878	8.176	588	560	526	XX		603
13NOV1621		1.2	7.5	92.5	6.750	6.930	8.036	8.334	568	539	511	XXX		704
13NOV1622		1.2	7.5	92.5	6.236	6.400	7.426	7.708	556	542	511	XXX		
13NOV1626		1.2	7.5	92.5	6.844	7.030	8.264	8.522	610	585	540			
14NOV0936		1.2	7.5	92.5	6.210	6.644	7.682	7.962						
14NOV0937		1.2	7.5	92.5	6.884	7.062	8.184	8.482		578	544			
14NOV0938		1.2	7.5	92.5	5.964	6.492	7.500	7.778	562	535	511	X		674
14NOV0940		1.2	7.5	92.5	6.704	6.884	8.004	8.304		595	548	XX		579
14NOV0943		1.2	7.5	92.5	6.138	6.300	7.336	7.618	556	536	508	XX		696
14NOV0953		1.2	7.5	92.5	6.232	6.400	7.448	7.734	617	579	540	XX		638
14NOV0956		1.2	7.5	92.5	6.456	6.622	7.674	7.960	595	573	533	XX		601
14NOV0957		1.2	7.5	92.5	6.322	6.484	7.518	7.800	602	570	533	XX	616	570
14NOV1000		1.2	7.5	92.5	6.508	6.676	7.726	8.012	617	580	540			
14NOV1005		1.2	7.5	92.5	6.102	6.270	7.332	7.618	595	571	533	XXX		619
14NOV1006		1.2	7.5	92.5	6.172	6.338	7.386	7.670	595	565	533	XXX		697
14NOV1009		1.2	7.5	92.5	6.126	6.296	7.364	7.654	602	573	537	XXX		588
14NOV1010		1.2	7.5	92.5	6.262	6.428	7.480	7.768	588	562	526	XX		644
14NOV1016		1.2	7.5	92.5	6.202	6.364	7.382	7.664	602	570	529	XXX		657
14NOV1017		1.2	7.5	92.5	6.044	6.210	7.264	7.552	617	589	540			
14NOV1022		1.2	7.5	92.5	6.182	6.350	7.402	7.686	602	569	529			
14NOV1023		1.2	7.5	92.5	6.258	6.424	7.474	7.760	595	570	537	XXX		629
14NOV1024		1.2	7.5	92.5	5.946	6.106	7.134	7.416	602	571	533	XXX		568
14NOV1025		1.2	7.5	92.5	6.032	6.194	7.222	7.502	625	584	540			
14NOV1033		1.2	7.5	92.5	6.370	6.530	7.560	7.842	617	584	544			
14NOV1034		1.2	7.5	92.5	6.098	6.264	7.314	7.598	625	583	540	XXX		621
14NOV1036		1.2	7.5	92.5	5.906	6.072	7.128	7.414	602	571	537	XXX		639
14NOV1037		1.2	7.5	92.5	6.030	6.198	7.248	7.532	602	568	533	XXX	596	587
14NOV1044		1.2	7.5	92.5	6.184	6.352	7.402	7.688	595	571	537	XXX	613	578
14NOV1045		1.2	7.5	92.5	5.896	6.064	7.122	7.408	595	571	533	XXX	631	637
14NOV1048		1.2	7.5	92.5	5.826	5.994	7.048	7.334	595	567	533	XXX		558
14NOV1049		1.2	7.5	92.5	6.022	6.182	7.208	7.490	595	569	533	XXX		641
14NOV1128	1	1.2	7.5	92.5	6.072	6.242	7.312	7.596	625	585	540			
14NOV1129	1	1.2	7.5	92.5	5.622	6.134	7.210	7.502	588	561	537	XXX		609
14NOV1134	1	1.2	7.5	92.5	6.396	6.556	7.578	7.858		558	522	XXX		623
14NOV1135	1	1.2	7.5	92.5	6.042	6.208	7.266	7.554	625	587	544	XXX		612
14NOV1213	1	1.2	7.5	92.5	6.118	6.288	7.348	7.634	602	567	529			
14NOV1214	1	1.2	7.5	92.5	5.922	6.092	7.152	7.438	588	566	533			
16NOV1209	1	1.2	7.5	92.5	5.810	5.976	6.986	7.316	588	566	533			

Test ID	Ramp	Phi	Fuel %	Air %	P1 (ms)	P2 (ms)	P3 (ms)	P4 (ms)	V1 (m/s)	V1.5 (m/s)	V2 (m/s)	Image Qual	Post Trig V (m/s)	Flame V (m/s)
RDTPlus Replaced Ultra-17														
27 NOV 1110	1	1.2	7.5	92.5	5.834	6.000	7.024	7.332	602	594	462			
27 NOV 1119	1	1.2	7.5	92.5	5.878	6.044	7.070	7.380	602	586	495			
27 NOV 1126	1	1.2	7.5	92.5	5.874	6.038	7.066	7.380	602	585	492			
27 NOV 1130	1	1.2	7.5	92.5	5.854	6.014	7.048	7.332	610	584	486	X		
27 NOV 1145	1	1.2	7.5	92.5	5.742	5.908	6.966	7.252	625	580	537	X		
27 NOV 1159	1	1.2	7.5	92.5	5.792	5.952	6.986	7.270	602	567	533	X		
27 NOV 1209	1	1.2	7.5	92.5	5.692	5.850	6.884	7.168	625	580	537	X		
27 NOV 1219	1	1.2	7.5	92.5	5.876	6.038	7.070	7.352	633	580	537	X		
27 NOV 1239	1	1.2	7.5	92.5	5.680	5.846	6.900	7.186	617	581	541	X		
27 NOV 1243	1	1.2	7.5	92.5	5.852	6.024	7.104	7.396	602	569	533	X		
27 NOV 1330	1	1.2	7.5	92.5	5.724	5.892	6.950	7.236	581	556	522	X		
27 NOV 1344	1	1.2	7.5	92.5	5.834	6.000	7.056	7.342	595	567	533	X		
27 NOV 1353	1	1.2	7.5	92.5	5.858	6.030	7.112	7.404	602	568	533			
27 NOV 1357	1	1.2	7.5	92.5	5.860	6.028	7.086	7.374	581	555	522	X	510	501
27 NOV 1414	1	1.2	7.5	92.5	5.832	6.000	7.050	7.336	595	567	530	X	601	653
27 NOV 1421	1	1.2	7.5	92.5	5.934	6.096	26.846	26.846	595	571	533			
27 NOV 1427	1	1.2	7.5	92.5	5.904	6.068	7.134	7.422	617			X	473	455
27 NOV 1434	1	1.2	7.5	92.5	5.984	6.150	7.208	7.504	610	563	530	X	601	541
27 NOV 1708	2	1.2	7.5	92.5	5.912	6.084	7.256	7.492	602	567	515	X	552	482
30 NOV 1140	4A	1.2	7.5	92.5	5.540	5.994	7.150	7.366	581	512				
30 NOV 1141	4A	1.2	7.5	92.5	5.762	5.928	6.992	7.298		519				
30 NOV 1145	4A	1.2	7.5	92.5	5.733	5.911	6.951	7.276	602	564	498			
30 NOV 1152	4A	1.2	7.5	92.5	5.800	5.966	7.030	7.324	562	577	469	XXX		
30 NOV 1202	4A	1.2	7.5	92.5	5.580	5.752	6.844	7.146	602	564	519	XXX		
30 NOV 1228	4A	1.3	8.1	91.9	5.562	5.730	6.791	7.084	581	549	505	X		
30 NOV 1234	4A	1.4	8.7	91.3	5.624	5.786	6.838	7.132	595	565	521	X		
30 NOV 1302	4A	1.3	8.1	91.9	5.644	5.814	6.902	7.202	617	570	519	X		
30 NOV 1328	4A	1.3	7.8	92.2	5.540	5.708	6.782	7.072	588	551	508	X		
30 NOV 1337	4A	1.4	8.4	91.6	5.606	5.776	6.856	7.152	595	559	526	X	553	504
30 NOV 1355	4A	1.5	8.9	91.1	5.740	5.902	6.940	7.248	588	556	515			
01 DEC 1210	4F	1.2	7.5	92.5	6.228	6.402	7.524	7.820				X	830	680
01 DEC 1218	4F	1.2	7.5	92.5	5.578	5.744	6.830	0.000	575	535	515	XXX	1103	1136
No Further Data from P4 Pressure Transducer														
01 DEC 1236	4F	1.4	8.4	91.6	5.582	5.744	6.812	0.000	602	552		X	1109	950
01 DEC 1610	4F	1.3	8.1	91.9	5.692	5.852	6.920	0.000	617	562		X	1109	881
01 DEC 1621	4F	1.3	8.1	91.9	0.000	0.000	0.000	0.000	625	562		X	1103	1053

Table 9. Test Summary.

THIS PAGE INTENTIONALLY LEFT BLANK

LIST OF REFERENCES

1. Friedman, R., "American Rocket Society," Vol. 24, p.349, November 1953.

2. Bauer, P. A, Damora, E. K., Manson, N., "Chronology of Early Research on Detonation Wave," *Dynamics of Detonations and Explosions: Detonations,* Vol. 133, AIAA Inc., pp 3-18, 1991.

3. Kuo, K. K., *Principles of Combustion,* 2nd ed., John Wiley & Sons, Inc., 2005.

4. Vasil'ev, A. A., "Optimization of Accelerators of Deflagration-to-Detonation Transition," in G. Roy, S. Frolov, R. Santoro, S. Tsyganov (Eds.), *Confined Detonations and Pulse Detonation Engines*, pp 41-48, Torus Press Ltd., 2003.

5. Higgins, A. J., Pinard, P., Yoshinaka, A. C., and Lee, J. H. S., "Sensitization of Fuel-Air Mixtures for Deflagration-to-Detonation Transition," in G. Roy, S. Frolov, D. Netzer, and A. Borisov (Eds.), *High-Speed Deflagration and Detonation: Fundamentals and Control*, pp. 45-49, ELEX-KM Publishers, 2001.

6. Channell, B. T., *Evaluation and Selection of an Efficient Fuel/Air Initiation Strategy for Pulse Detonation Engines*, Master's Thesis, U.S. Naval Postgraduate School, Monterey CA, September 2005.

7. Hutcheson, Patrick D., *Design, Modelling and Performance of a Split Path JP-10/Air Pulse Detonation Engine (PDE)*, Master's Thesis, U. S. Naval Postgraduate School, Monterey CA, December 2006.

8. Falempin, F., Bouchaud, D., Forrat, B., Desbordes, D. Daniau, E., P., *Pulsed Detonation Engine: Possible Application to Low Cost Tactical Missile and to Space Launcher*, AIAA-2001-3815, AIAA Inc., 2001.

9. Baurle, R. A., Alexopoulos, G. A., and Hassan, H.A., "Analysis of Supersonic Combustors with Swept Ramp Injectors," *Journal of Propulsion and Power*, Vol. 3, March-April 1997, pp. 327-328.

10. *CFD-FASTRAN Theory Manual*, ESI CFD, Inc., 2004.

11. *Shockwave Calculator Applet: A Java Applet for Computing Normal and Oblique Shockwave Properties for Calorically Perfect and Real Gasses*, Matthew MacLean (Developer), www.engapplets.vt.edu/fluids/shockcal/shockcal.html, last referenced 8 December, 2006.

12. Donohue, J. M., McDaniel, J. C. and Haj-Hariri, H., "Experimental and Numerical Study of Swept Ramp Injection into a Supersonic Flowfield," *AIAA Journal*, Vol. 32, No. 9, pp. 1860-1867, 1994.

13. Fludovich, Michael A. Jr., *Investigation of Detonation Wave Diffraction Interaction with Reactive Transpiration*, Master's Thesis, U.S. Naval Postgraduate School, Monterey CA, September 2002.

14. Fludovich, Michael A. Jr., "Pulsed Detonation Engines: Investigation of Detonation Wave Diffraction with Reactive Transpiration," Master's Thesis Presentation, Monterey CA, September 2002.

15. Ultra 17 High-Speed Imaging System Data Sheet, DRS Data & Imaging Systems, Inc.

16. Lightning RDTPlus High-Speed Digital Camera Data Sheet, DRS Data & Imaging Systems, Inc.

17. Benedict, R.P., *Fundamentals of Temperature, Pressure and Flow Measurements*, John Wiley & Sons, Inc., 1984.

18. *LabVIEW Basics I: Introduction Course Manual*, Software Version 6.1, National Instruments, Corp., May 2002.

19. *Ultra Operators Manual: Ultra Software Version 1.1*, DRS Hadland Ltd., 2 July 2002.

20. *MiDAS 2.0 User Manual: Version 2.1.8*, Xcitex Inc., 2004.

INITIAL DISTRIBUTION LIST

1. Defense Technical Information Center
   Ft. Belvoir, Virginia

2. Dudley Knox Library
   Naval Postgraduate School
   Monterey, California

3. Professor Christopher Brophy
   Department of Mechanical and Astronautical Engineering
   Monterey, California

4. Professor Jose Sinibaldi
   Department of Mechanical and Astronautical Engineering
   Monterey, California

5. LCDR Carlos Medina
   Naval Postgraduate School
   Monterey, California